Εθνικό Μετσόβιο Πολυτεχνείο
Σχολή Πολιτικών Μηχανικών
Δ.Π.Μ.Σ 'Δομοστατικός Σχεδιασμός & Ανάλυση των Κατασκευών'
Εργαστήριο Εδαφομηχανικής

National Technical University of Athens
School of Civil Engineering
MSc in Analysis & Design of Earthquake Resistant Structures
Soil Mechanics Laboratory

Μεταπτυχιακή Εργασία

Γεώργιος Κ. Ντούσκας

Επιβλέπων:

Καθηγητής Γ. Γκαζέτας

Σεισμική Απόκριση Εγκιβωτισμένων Θεμελιώσεων σε Ανομοιογενές Έδαφος

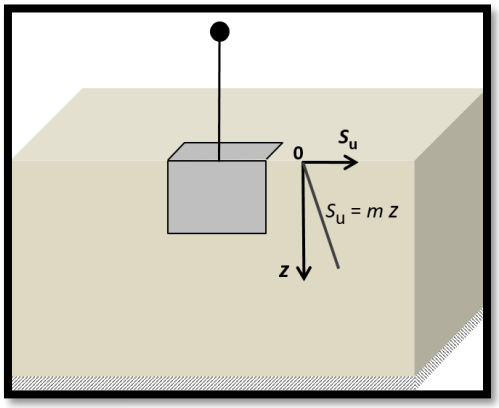

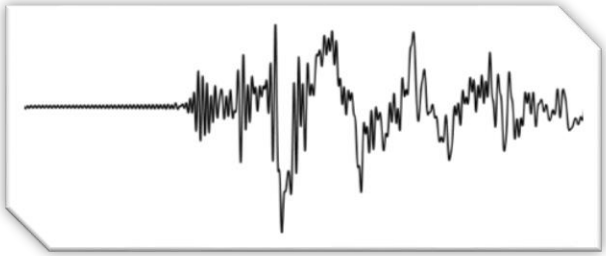

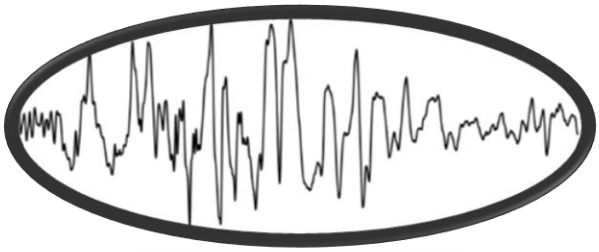

Seismic Response of Embedded Foundations in Inhomogeneous Soil

Master of Science Thesis by

George Ntouskas

Supervised by:

Professor G. Gazetas

Αθήνα, Φεβρουάριος 2018 **Athens, February 2018**

Thanks…

At the end of this postgraduate thesis, I would like to thank all those who have contributed to this effort.

First, I would like to warmly thank our professor George Gazetas who honored me with his trust and gave me the opportunity to work under his supervision and guidance in a very creative and pleasant work environment. His advice and guidance have been valuable to my academic years and will follow me on my professional career.

Thanks deserve to all the professors of the university that impart me knowledge during my studies.

I would like to thank my family, my fellow students and friends for their continuous and uncompromising support, not only during this thesis but also in the overall academic years. I wish them all the best.

Finally, I dedicate this thesis to John (‘Giannis’) Tzomakas, my former physics professor, who unfortunately passed away the final days of this work. His precious advice and help gave me the opportunity to become a member of the School of Civil Engineering, and they will guide me for the rest of my life.

TABLE OF CONTENTS

ABSTRACT

In the present MSc thesis results of a three-dimensional finite-element study for the effect of embedment on the undrained bearing capacity, the elastic stiffness, and the seismic behavior of square-in-plan foundations are presented for two linearly inhomogeneous soil profiles. For static analysis, equations for uniaxial horizontal (Q) and pure-moment (M) limit loads with the relative elastic stiffnesses (K_{HH} and K_{MM}) as functions of soil heterogeneity and embedment ratio are exported. Additionally, capacity envelopes for (QM), (NQ) and (NM) loading combinations are presented; special references for the significance of the vertical load (N) and the position of the reference point are noted. The response is affected by the type of contact between the foundation interfaces (vertical and horizontal) with the surrounding and underlying soil. For this reason, a comparison for two different soil–foundation interaction types is made; the ideal case of fully bonded contact [FBC] in contrast to tensionless and of limited shear (sliding) resistance interfaces [TSI]. Extensive comparisons are made with the results for homogeneous soil. One-dimensional seismic response of embedded foundations with a simple slender structure is investigated parametrically, as function of the foundation embedment ratio, the soil heterogeneity, the vertical safety factor and the superstructure slenderness. Diagrams of acceleration in various model positions, foundation settlement via rotation angle, loops $M–\theta$ for two seismic records are presented. Only [TSI] type of soil–foundation interaction interface is investigated. For credible results and conclusions, the system is subjected to two different seismic stimulations with various characteristics.

KEYWORDS: bearing capacity; failure; finite-element modelling; foundations; inhomogeneous soil; soil/structure interaction; seismic response

INTRODUCTION

Analysis of the foundation design is an engineering issue of major importance for many decades. For the static problem, foundation bearing capacity limits were obtained with the classic bearing capacity theory (Terzaghi, 1943; Meyerhof, 1953; Brinch Hansen, 1970). This theory has given satisfactory solutions, but researchers have attempted to come up with a more accurate idea. Most recently, a lot of studies (Butterfield & Ticoff, 1979; Georgiadis & Butterfield, 1988; Nova & Montrassio, 1991; Butterfield & Gottardi, 1994; Martin, 1994; Salencon & Pecker, 1995; Bransby & Randolph, 1999; Gottardi *et al.*, 1999; Houlsby & Puzrin, 1999; Taiebat & Carter, 2000; Houlsby, 2003; Randolph & Puzrin, 2003; Gourvenec, 2007, 2008; Yun & Bransby, 2007; Chatzigogos *et al.*, 2009; Randolph & Gourvenec, 2011; Ntritsos *et al.*, 2015) introduced and utilised the 'failure envelope' method. According to this, all *NQM* load combinations (where *N* is the vertical force, *Q* is the horizontal force, and *M* the overturning moment) can be represented with a surface designed in a Cartesian coordinate system with *NQM* axes. If an *NQM* combination point is inside the envelope, the foundation is safe. If it is an envelope point, a 'failure' mechanism is formed.

Even if these theories are a satisfactory base for the foundation capacity problem, also other parameters need to be included in order to simulate the reality. Most previous studies refer to strip and circular foundations, where soil–foundation interaction is fully bonded (Bransby & Randolph, 1999; Poulos et al., 2001; Yun & Bransby, 2007; Gourvenec, 2008). Ntritsos *et al.* (2015) presented an imperfect soil–foundation contact, that is, a tensionless interface of limited shear capacity allowing the foundation sliding and uplift (interface non-linearity).

Another important issue is that most of the above-mentioned researches consider the soil as a continuous elastoplastic homogeneous continuum. Recent studies present as main issue of consideration, the heterogeneity of the soil undrained shear resistance and the way this affects the bearing capacity and the failure mechanisms of the soil in various load combinations (Yun & Bransby, 2007; Gourvenec, 2008) for strip and circular foundations. Specifically, is considered linear increase of the soil undrained shear resistance with the depth (with non-zero soil shear resistance at surface), as a reasonable assumption.

The current research investigates the static and seismic response of square foundations embedded in linearly inhomogeneous soil profiles (with zero soil shear resistance at surface) under undrained loading conditions. The foundation embedment ratio varies ($0 \leq D/B \leq 1$). The static soil–foundation interaction is examined first as a fully bonded problem, and secondly as one with tensionless sliding interface. The second interaction type is also investigated in seismic foundation response. The results arise from a three-dimensional (3D) finite-element (FE) model considering the soil as an elastoplastic continuum with linearly increasing undrained shear resistance.

Fig. 1 presents the two phases of the research. At first (Fig. 1(a)), the bearing capacity of the soil–foundation system is obtained for monotonic *NQM* load combinations applied directly at the foundation base level. Each and every load combination eventually leads to bearing capacity point of the presented 'failure' envelope.

Secondly (Fig. 1(b)), the entire soil–foundation–superstructure system is modelled, where the superstructure is a rigid beam with a lumped mass at its top. Seismic loading is apllied at the base of the whole model. The seismic excitations are chosen for their different characteristics, in order to examine how the soil heterogeneity affects the system response. Note that P–Δ effects are examined.

Finite-element modelling

All 3D FE analyses are performed with Abaqus (2013). Fig. 2 depicts the 3D FE mesh, taking advantage of problem symmetry. Soil and foundation are simulated with eight-noded hexahedral brick-type elements, non-linear for the former and elastic for the latter. The superstructure is analysed with beam elements.

The soil is an inhomogeneous clay stratum simulated as an elastoplastic material with linearly increasing (with depth) undrained shear strength. The soil strength profile is given by the following equation

$$S_u = S_{uo} + mz \tag{1}$$

where S_{uo} (≈ 0) is the shear strength at the soil surface, and m is the gradient of undrained shear strength with depth (z) in terms of kPa/m. Fig. 1 presents the two different inhomogeneous soil profiles; for m=2 and 10 kPa/m. The shear modulus G increases linearly with depth, according to gradient λ [$\approx$ m(600)]. The soil Young's modulus is a linear function of depth, maintaining a constant ratio E_u/S_u=1800. It also applies γ=20 kN/m^3 and Poisson's ratio (ν) for the soil equals to 0·49. The undrained material response of the soil is expressed by a linear elastic perfectly plastic constitutive law with the undrained Young's modulus (E_u) and Poisson's ratio (ν). Failure is defined by the Tresca criterion, which determines the maximum shear stress in any plane according to the undrained shear strength (S_u). The foundation and the superstructure are modelled as a rigid body. The base of the model is fixed in all coordinate directions. Special interface elements are used for the soil–foundation interface, simulating the two referred contact conditions.

(a) Fully bonded contact (FBC): the foundation is in perfect contact with the soil. This type of contact has infinite tensional and shear capacities, not permitting the foundation separation and slippage on the contact surface with the soil.

(b) Tensionless sliding interface (TSI): on the contrary to (FBC), foundation separation from the soil and slippage at the soil–foundation contact surface, are allowed. The latter obeys in total stress analysis Coulomb's friction law with φ_a=0 and $c_a=\alpha S_u$. Separation results from the tensionless contact surface behaviour. In current research, adhesion coefficient, α, is equal to 0·50 for the lateral soil–foundation interaction and 1·00 for the base soil–foundation interaction. It is considered as a logical assumption as in reality, soil is more dense at the base of the foundation than the corresponding soil in the sides of the foundation, which drives to more efficient soil–foundation interaction. It is also assumed that for the lateral soil–foundation interaction, S_u is equal to the soil undrained shear strength in the middle of the foundation embedment. For the base soil–foundation interaction, S_u is equal to the soil undrained shear strength at the base of the foundation.

Loading conditions

In static analysis (Fig. 1(a)), monotonic loading is set at the centre of the foundation base. First, a quota of the ultimate vertical bearing capacity N_u is applied as a vertical force N. Secondly, a displacement probe of constant ratio u/θ until the foundation load remains stable with increased displacement is performed. In the words of Yun & Bransby (2007): 'once the failure envelope is reached, each loading path travels around the failure envelope until it reaches a termination point where the

direction of the tangent to the failure envelope matches the prescribed displacement ratio'. As the direction of the incremental plastic displacement vector at failure is vertical to the failure envelope, latter can be considered as the plastic potential surface.

Model validation

In order to validate the FEA model, a comparison is made with the research of Yun & Bransby (2007), where plain-strain analyses for foundations embedded in inhomogeneous soil were developed. The analysed soil is clay with undrained shear strength linearly increased with depth (gradient equal to 1·1 kPa/m) and shear strength at soil surface equal to zero. Additively, soil is modelled as linearly plastic-perfectly plastic with Poisson's ratio, v=0·49 and E_u/S_u=400. Soil–foundation interface permits no sliding or foundation uplift, as foundation remains always in full contact with soil. Validation analysis, has the same soil characteristics and it was developed for the foundation with D/B=1. Fig. 3 depicts MQ envelope for N/N_{ult}=0, which was developed with probe and swipe analyses, compared to the results of Yun & Bransby (2007). As seen divergence of two solutions is satisfactory, even if the results present higher bearing capacity.

NUMERICAL AND (SOME) ANALYTICAL RESULTS

FULLY BONDED CONTACT (FBC)

Numerical results from the 3D FE analysis (FEA) of square-in-plan embedded foundations in Gibson soil are presented, some of which are compared with those of Ntritsos *et al.* (2015).

Horizontal bearing capacity & stiffness. The lateral bearing capacities Q_{max} and Q_{ult} of a square embedded footing are investigated under pure horizontal translation (rotation θ=0) and horizontal force (rotation M=0) respectively. Following equations are fitted to the 3D FEA numerical results, presenting the ratio of shear soil resistances of inhomogeneous soil via $A_{base}S_u^{(z=B)}$ and for each degree of inhomogeneity:

$$Q_{max}/A_{base}S_u^{(z=B)} \approx Q_{max}/AmB \approx [0{\cdot}14 + 1{\cdot}36(D/B)] + [4{\cdot}65(D/B)^2] \quad (2)$$

$$Q_{ult}/A_{base}S_u^{(z=B)} \approx Q_{ult}/AmB \approx [0{\cdot}11 + 2{\cdot}27(D/B)] + [2{\cdot}08(D/B)^2] \quad (3)$$

It must be noted that mB is equal to undrained shear strength in depth B. Ntritsos *et al.* (2015) results for homogeneous soil are normalised with the common soil undrained shear strength 150 kPa. Therefore, all soil profiles are normalized with soil shear strength in a depth B.

Fig. 4 depicts the two horizontal capacities Q_{max} (zero rotation) and Q_{ult} (zero moment) from the FE analysis for various degrees of heterogeneity (10 values of m, from 1 to 10 kPa/m) and for the homogeneous soil profile of Ntritsos *et al.* (2015), against D/B. It is obvious that all soil profiles have similar behaviour. Nevertheless, in the homogeneous material from D/B=0·2 begins to distinguish the difference in the strength of the system for the two different capacities, whereas in the non-homogeneous materials this divergence is obvious for D/B>0·4~0·5. This behaviour can be principally explained because of the greater undrained shear strength of foundation's lateral soil in homogeneous soil profile, which leads to increased exploitation of embedment in horizontal bearing capacity with zero rotation.

Additively, in Gibson soil profiles, normalised horizontal bearing capacity is independent of m for each embedment ratio. This ability is really impressive in Q_{max} capacity and for low to medium embedment ratios in both capacities.

Now, in terms of horizontal elastic stiffness, it was fitted the following equation to the numerical results of 3D FEA depicting the ratio of elastic horizontal stiffness of a square embedded foundation via the horizontal stiffness of a surface foundation with the same base founded in a inhomogeneous soil for various degrees of heterogeneity:

$$K_H/K_{HO} \approx [1 + 8{\cdot}46(D/B)] + [3{\cdot}76(D/B)^2] \quad (4)$$

Fig. 5(a) illustrates horizontal stiffness K_H of embedded foundation over horizontal stiffness K_{HO} of surface foundation for various degrees of inhomogeneity (10 values of m, from 1 to 10 kPa/m) against D/B. It is obvious that for a specific value of m, the ratio K_H/K_{HO} increases linearly as a function of D/B. Additionally, for a specific value of embedment, as m increases, the ratio K_H/K_{HO} increases with a slightly rising rate.

An interesting normalization is made by dividing the horizontal stiffness with the λB^2. The results are expressed by the equation:

$$K_H/\lambda B^2 \approx [0{\cdot}76 + 6{\cdot}32(D/B)] + [2{\cdot}81(D/B)^2] \quad (5)$$

Fig. 5(b) presents horizontal stiffness K_H of embedded foundation over λB^2 for various degrees of λ (10 values of λ, from 600 to 6000 kPa/m) against D/B. For each value of λ, the ratio $K_H/\lambda B^2$ increases practically linearly with increasing embedment ratio. Additionally, when λ increases the ratio decreases. This means that the increase of shear modulus gradient leads to leads to a slight increase of the elastic stiffness.

In the above words, however, there is no mention to the effect of the vertical load N in the horizontal bearing capacity. As also Ntritsos *et al.* (2015) noted, the FEA gives results that are slightly affected by the vertical load N. Veritably, although not thoroughly reported in this paper, relevant numerical simulations show that the effect of vertical load becomes significant only progressively (with increasing N) when approximately

$$N > 3B^2S_u \approx N_{uo}/2 \quad (6)$$

in which N_{uo} is the ultimate vertical capacity of the surface foundation, as it will be shown subsequently.

Figs 6(a), 7(a) and 7(c) illustrate the (purely horizontal) failure mechanisms for two embedment ratios (0·2 and 1), for two inhomogeneous soil profiles (m=2 and 10 kPa/m) and the homogeneous soil profile of Ntritsos *et al.* (2015) in the form of the vectors of displacement, with superimposed as dark shadows the regions of large plastic strains. It is interesting to observe that the plastic strains tend to localise in well-defined shear bands. In such cases, the problem can be mesh dependent and a sensitivity analysis is required. Such a sensitivity study was performed as part of the present study, leading to the selection of the adopted FE mesh.

The inhomogeneous soil profile with m=10 kPa/m and the homogeneous soil profile present identical failure mechanisms: sliding of the foundation–soil system develops, with active and passive failure on the front and back side of the foundation, and shear at the base and at the two parallel sidewalls. However, inhomogeneous soil profile with m=2 kPa/m present a slightly different failure mechanism for D/B=1. The difference lies in the form of soil plastification beneath the right side of the foundation

base, marked with a black circle in Fig. 6(a). A logical reason for this behaviour is the rapid plastification of some soil elements in foundation base (relatively low undrained shear strength in contrast to other soil profiles), which drives to diagonal sedimentation (in the direction of motion) by drifting a small mass of not plasticised-soil.

Rotational bearing capacity & stiffness. The moment bearing capacities M_{max} and M_{ult} of a square embedded footing are examined under pure rotation (horizontal displacement u=0) and overturning moment (horizontal force Q=0). Following equations are fitted to the 3D FEA numerical results, presenting the ratio of rotational soil resistance of inhomogeneous soil via $A_{base}S_u^{(z=B)}B$ and for each degree of inhomogeneity:

$$M_{max}/A_{base}S_u^{(z=B)}B \approx M_{max}/AmB^2 \approx [0{\cdot}24 + 0{\cdot}31(D/B)] + [2{\cdot}76(D/B)^2] \quad (7)$$

$$M_{ult}/A_{base}S_u^{(z=B)}B \approx M_{ult}/AmB^2 \approx [0{\cdot}21 + 0{\cdot}75(D/B)] + [1{\cdot}38(D/B)^2] \quad (8)$$

As previously, mB is equal to undrained shear strength in depth B. Ntritsos *et al.* (2015) results for homogeneous soil are normalised with the common undrained shear strength 150 kPa. Therefore, all soil profiles are normalized with soil shear strength in a depth B.

Fig. 8 presents the two rotational capacities M_{max} (zero horizontal displacement) and M_{ult} (zero vertical force) from the FE analysis for various degrees of heterogeneity (10 values of m, from 1 to 10 kPa/m) and for the homogeneous soil profile of Ntritsos *et al.* (2015), against D/B. Soil profiles have similar behaviour again. Nevertheless, in the homogeneous material from D/B=0·2 begins to distinguish the difference in the strength of the system for the two different capacities, whereas in the non-homogeneous materials this divergence is obvious for D/B>0·4. This behaviour can be principally explained because of the greater undrained shear strength of foundation's lateral soil in homogeneous soil profile, which leads to increased exploitation of embedment in rotational bearing capacity with zero horizontal displacement. An important point to refer is that, in Gibson soil profiles, normalised rotational bearing capacity is practically independent of m, especially dor low embedment ratios.

As for the rotational stiffness, it was fitted the following equation to the numerical results of 3D FEA depicting the ratio of elastic rotational stiffness of a square embedded foundation via the rotational stiffness of a surface foundation founded in a inhomogeneous soil for various degrees of inhomogeneity:

$$K_R/K_{RO} \approx [1+ 0{\cdot}23(D/B)] + [14{\cdot}84(D/B)^2] \quad (9)$$

Fig. 9(a) depicts rotational stiffness K_R of embedded foundation over rotational stiffness K_{RO} of surface foundation for various degrees of inhomogeneity (10 values of m, from 1 to 10 kPa/m) against D/B. It is obvious that for a specific value of m, the ratio K_R/K_{RO} increases with increasing D/B, presenting rising rate, especially at higher embedment ratios. Additionally, for a specific value of embedment, as m increases, the ratio K_R/K_{RO} increases with a slightly rising rate.

Similarly to the horizontal stiffness, normalization is made again by dividing the rotational stiffness with the λB^3. The results are expressed by the equation:

$$K_R/\lambda B^3 \approx [2{\cdot}52 + 0{\cdot}55(D/B)] + [36{\cdot}1(D/B)^2] \quad (10)$$

Fig. 9(b) presents rotational stiffness K_R of embedded foundation over λB^3 for various degrees of λ (10 values of λ, from 600 to 6000 kPa/m) against D/B. For each value of λ, the ratio $K_H/\lambda B^2$ increases with increasing embedment ratio. It must be noted that, the is no certain pattern of the lines as function of λ. Specifically, for low values of λ (from 1 to 5 kPa/m), as λ increases the ratio decreases. For higher values of λ, the ratio increases with changing rate. This indicates that as the soil heterogeneity takes high values, the rotational capacity increases with higher rate.

It could be useful to notice in Figs 5(a) and 9(a) that elastic rotational stiffness is less affected from the gradient m than the elastic horizontal stiffness. Indeed, for D/B=1, K_R/K_{RO}=16 for m=1 kPa/m and 20·2 for m=10 kPa/m, while K_H/K_{HO} is equal to 12·5 and 20·8 respectively. However, the effect of embedment on stiffnesses differentiates depending on the embedment. Specifically, for m=10 kPa/m and D/B=0·5, K_H/K_{HO} is equal to 9·4, while K_R/K_{RO}=6·8. For D/B=1, K_H/K_{HO} is equal to 20·8, while K_R/K_{RO}=20·2. It is obvious that especially for great embedment ratios (D/B>0·5), elastic rotational stiffness is affected more by increasing embedment. In contrast to this, elastic horizontal stiffness is affected semi-linearly by increasing embedment. A possible reason for this, is that low strength of soil (especially near the surface), do not permit the rotational stiffness to increase to a large extent, while the rotational stiffness reacts in a similar way to each value of embedment ratio. As a result, only for D/B=1 the two stiffnesses are equal. It should be referred that for values of m higher than 10 kPa/m the rotational overcomes the horizontal stiffness and this come to agreement with Ntritsos *et al.* (2015) proving that embedment ratio has increased effect on the rotational stiffness.

Figs 6(b), 7(b) and 7(d) illustrate the (purely rotational) failure mechanisms for two embedment ratios (0·2 and 1), for two inhomogeneous soil profiles (m=2 and 10) and the homogeneous soil profile of Ntritsos *et al.* (2015) in the form of the vectors of displacement, with superimposed as dark shadows the regions of large plastic strains.

For D/B=0·2 and in case of m=2 kPa/m (Fig. 6(b)), soil fails presenting a *scoop-wedge* failure mechanism. A reason for this behaviour is the low soil undrained strength resulting in a high settlement on the right side of the foundation (great soil plastification) and low elevation on the left side (low soil plastification) with simultaneous ground swelling on the right face and displacement of the semicircular shear zone to the left. This semicircular shear zone has a centre (indicated with the solid dot in the figure) with distance L≈0 from the foundation base and L≈0.25B from foundation base centre. In the inhomogeneous soil profile with m=10 kPa/m (Fig. 7(b)) the failure mechanism changes and tends to the *scoop* failure mechanism with a larger radius of the semicircular failure and with a sufficient degree of plastification at the right lower edge of the foundation. However, this plastification is lower than the homogeneous soil with m=2 kPa/m, as well as the soil swelling on the right side. This is due to the greater soil stiffness and strength, which drives to approximately equal vertical movements of the foundation sides and to symmetrical appearance of the shear semicircular zone with respect to the vertical axis, which goes through the foundation centre. This semicircular shear zone has a centre (indicated with the solid dot in the figure) with distance L≈0 from the foundation base and L≈0·1B from the foundation base centre. In the homogeneous soil profile (Fig. 7(d)) the failure mechanism is identical.

For D/B=1 and m=2 kPa/m (Fig. 6(b)), a composite failure mechanism, including spheroidal failure surface near the base, active and passive wedges on the upper part of the normal sidewalls, and torsional shear on the parallel sidewalls. The spheroidal shear zone of failure is unsymmetrical with respect to the vertical axis, which goes

through the foundation centre and has a rotation pole (indicated with the solid dot in the figure) with distance $L \approx 0$ from the foundation base and $L \approx 0 \cdot 3B$ from the foundation base centre. Additionally, high soil plastification is presented at the right edge of the foundation base. This also appeared in the foundation with $D/B=0.2$ and is due to causes referred. In the other two soil profiles (Figs 7(b) and 7(d)), the spheroidal shear zone is symmetrical with respect to the vertical axis of the foundation and has a rotation pole (indicated with the solid dot in the figure) with distance $L \approx 0$ from the foundation base and $L \approx 0$ from the foundation base centre.

FAILURE ENVELOPES

MQ *interaction (with* N*=0)*

In previous sections, perspectives of the maximum horizontal load Q_{max} and of the maximum overturning moment M_{max} have been analysed separately. Nonetheless, it was a combination of Q and M that led to these two limit values: a moment was necessary to nullify the rotation as required for Q_{max} and a horizontal force to nullify the horizontal displacement as required for M_{max}. But these were only two MQ combinations out of infinite possibilities. The full interaction between the limiting values of Q and M, comprising all combinations, is portrayed in Figs 10(a), 11(a), 12, 13 and 14, in the normalised form: $M=BAS_u^{(z=B)}$ plotted against $Q=AS_u^{(z=B)}$ and for two values of D/B, 1 and 0·2. The vertical load, N, which also affects the QM interaction, is taken as 0 in both figures. Figs 10(b) and 11(b) are meant to illustrate the fact that the shape of the failure envelopes depends strongly on the point which M, Q, u and θ refer to. Regardless of them, the information conveyed by each of the three different sets of envelopes (interaction diagrams) for the three reference points (base, middle, top) is exactly the same.

In Figs 10(a), 11(a), 12, 13 and 14 the location of Q_{max} and M_{max} (for the three soil profiles) is shown at the two extremes of the envelope, where the normal lines to the envelope (the 'failure surface') are parallel to the horizontal and vertical axes, respectively. This is a consequence of the associated flow rule adopted in the present soil constitutive model (preservation of normality). Also indicated in the figures are the two limit values of the purely horizontal-force ($M=0$) and purely overturning-moment ($Q=0$) loading, denoted as Q_{ult} and M_{ult}, respectively (adopting the terminology of Gourvenec). The normal vectors to the envelope at these latter locations point to the negative M and Q axes, respectively–indicative of negative (counter-clockwise) rotation and negative (on the x-axis) displacement, respectively. This behaviour can be visualized in the inserted four snapshots of the vectors of displacement (with the concentration of plastic shear strains superimposed as shadows), for each of the four limit loads referred here. They correspond to pure horizontal load, pure horizontal translation, pure moment and pure rotation, respectively. It is noticeable, that all profiles have similar behaviour and present similar characteristics. Nevertheless, they differ in the envelope values and in the face of some failure mechanisms.

Figs 10(a), 11(a), 12, 13 and 14 reveal a significant effect of embedment, not only on the values of the various limit loads but also on the shape of the envelope; the latter becomes increasingly skewed with increasing (relative) depth, D/B. As a result, the maximum moment capacity M_{max} (which occurs in the presence of positive horizontal load, applied always at the base) increases disproportionately more than the increase of M_{ult}. Indeed, the ratio M_{max}/M_{ult} attains (approximately) the values of

(a) 1·39 for D/B=1 (inhomogeneous soil: m=2 kPa/m)
(b) 1·06 for D/B=0·2 (inhomogeneous soil: m=2 kPa/m)
(c) 1·43 for D/B=1 (inhomogeneous soil: m=10 kPa/m)
(d) 1·11 for D/B=0·2 (inhomogeneous soil: m=10 kPa/m)
(e) 1·75 for D/B=1 (homogeneous soil)
(f) 1·10 for D/B=0·2 (homogeneous soil)

Similar are the trends of the Q_{max}/Q_{ult} ratio, which is equal to

(a) 1·39 for D/B=1 (inhomogeneous soil: m=2 kPa/m)
(b) 1·00 for D/B=0·2 (inhomogeneous soil: m=2 kPa/m)
(c) 1·28 for D/B=1 (inhomogeneous soil: m=10 kPa/m)
(d) 1·03 for D/B=0·2 (inhomogeneous soil: m=10 kPa/m)
(e) 1·60 for D/B=1 (homogeneous soil)
(f) 1·02 for D/B=0·2 (homogeneous soil)

For the surface foundation (D/B=0), both ratios approach 1, as there is negligible coupling of M and Q under fully bonded contact and N=0, as considered here.

To further elucidate the role of embedment on the *shape* of the QM failure envelopes, Fig. 15 compares the four envelopes (for D/B=0, 0·2, 0·5 and 1) as plotted in the normalized coordinate system: $M=M_{ult}$ plotted against $Q=Q_{ult}$. It is noticeable that all soil profiles present similar graphs.

It is also worth observing the failure mechanisms at Q_{ult} and M_{ult} in the inserts in Figs 10, 11, 12, 13 and 14. Fig. 10, depicts failure mechanisms for inhomogeneous soil with m=10 kPa/m and Fig. 11 for homogeneous soil (Ntritsos *et al.*, 2015). It is noticeable that failure mechanisms are similar, with slight differences. For homogeneous soil, under pure moment loading, at M_{ult}, applied at the foundation base level, a scoop mechanism is observed with its rotation pole (indicated with the solid dot in the figure) located approximately $L\approx D/2$ above the base, that is, at the foundation centre of gravity. The foundation response is therefore mainly rotational, but it is also accompanied by a negative horizontal translation. The latter, as indirectly evidenced by the oblique intersection of the failure envelope with the moment ordinate axis, is substantial only for the deeper foundation (D/B=1); it is of marginal importance for the shallow foundation (D/B=0·2), and would hardly exist for a surface foundation. The corresponding mechanism for inhomogeneous soil with m=10 kPa/m has its rotation pole at $L\approx D/3$ from the foundation base.

For homogeneous soil, under purely horizontal loading, at Q_{ult}, a reverse *scoop* mechanism is formed with its centre of rotation moving up near the soil surface – nearly a pendulum. Thus, failure consists of (nearly equally important) horizontal translation and counter-clockwise rotation. In this case, the obliquity of the intersection of the envelope with the Q axis is appreciable even for the shallow foundation (D/B=0·2). The same applies for the inhomogeneous soil with m=10 kPa/m with the difference that, the rotation pole is a bit closer to the soil surface.

In Figs 12, 13 and 14 failure mechanisms for all soil profiles and for D/B=0·2 are presented. Under pure moment loading, at M_{ult}, in inhomogeneous soil with m=10 kPa/m and in homogeneous soil, a *scoop* mechanism is formed, with the difference that rotation pole is closer to the surface in inhomogeneous soil. In inhomogeneous soil with m=2 kPa/m is formed a *scoop-wedge* mechanism with the rotation pole at the surface and in a distance $L\approx 0.25B$ left from the upper foundation base. The reason why this soil presents different failure mechanisms is already explained.

QN *interaction (with* M*=0)*

The significance of the vertical load for the ultimate value Q_{ult} of a solely horizontal lateral load (M=0) and for the examined soil profiles is portrayed in Fig 16, for four values of D/B: 0, 0·2, 0·5, 1. The normalization is in the form of $Q_{ult}=AS_u$ plotted against N/AS_u and in the normalized form $Q_{ult}=Q_{ult,N=0}$ plotted against $N/N_{ult,Q=0}$. It is noticeable that the normalised curves as functions of D/B have the similar face for all soil profiles! The only difference is the lower values of inhomogeneous soil envelopes.

Note, for the second type of normalization, that for low vertical loads compared to the vertical capacity, $N/N_{ult,Q=0}<0{\cdot}5$, or equivalently for safety factors FS_V against vertical bearing capacity mobilization exceeding 2 (a most frequent situation in practice), the horizontal capacity remains almost constant, regardless of the axial force magnitude. This is true for all examined embedment ratios. Nevertheless, an abrupt reduction in load carrying capacity is noticed at higher vertical loads, with $Q_{ult}=Q_{ult,N=0}$ dropping to about 0·5 for an (admittedly very small) $FS_V=1{\cdot}11$ (i.e. $N/N_{ult,Q=0}=0{\cdot}9$). The same behaviour is obvious for all soil profiles.

MN *interaction (with* Q*=0)*

The significance of the vertical load for the ultimate value M_{ult} of a purely moment loading (Q=0) for the examined soil profiles is portrayed in Fig. 17, for four values of D/B: 0, 0·2, 0·5, 1. The normalization is in the form of $M_{ult}=ABS_u$ plotted against $N=AS_u$ and in the normalised form $M_{ult}/M_{ult,N=0}$ plotted against $N/N_{ult,M=0}$. Observe that the differences between the normalised curves as functions of D/B are barely if at all distinguishable, and have the similar face for homogeneous and inhomogeneous soil profiles! The only difference is the lower values of inhomogeneous soil envelopes.

The vertical load plays a slightly greater role than for the horizontal capacity. At low values of $N/N_{ult,M=0}$ the effect of N on the M_{ult} is negligible, but the limit now is $N/N_{ult,M=0}<0{\cdot}3$ rather than 0·5. This is true also for all examined embedment ratios. However, an abrupt reduction in load-carrying capacity is noticed at higher vertical loads, with $M_{ult}/M_{ult,N=0}$ dropping to about 0·5 for the very small $FS_V=1{\cdot}25$ (i.e. $N/N_{ult,M=0}=0{\cdot}8$). The same behaviour is obvious for all soil profiles.

TENSIONLESS, POTENTIALLY SLIDING INTERFACE (TSI)

MQ *envelopes with* N*≈0*

A very essential reduction of the effects of embedment ensues when the five interfaces of the foundation with the soil are incapable of transmitting (net) tensional normal stresses and shear stresses that exceed the adhesive stress $f_S=\alpha S_u$. Therefore, separation as well as sliding of parts of the walls or the base from the surrounding and underlying soil is possible.

Figs 18, 19 show the *MQ* envelopes for the D/B=1 for a foundation with TSI in case of inhomogeneous soil with m=10 kPa/m and the homogeneous soil (Ntritsos *et al.*, 2015) respectively, along with the snapshots of the displacement vectors and the high plastic shear strain 'shadows'. Note that results for inhomogeneous soil profile refer to safety factors FS_V against vertical bearing capacity mobilization equal to 4, or equivalently N/N_{ult}=0.25. On the contrary, results for homogeneous soil profile refer to N/N_{ult}=0. However, this slight difference in the vertical load is not considered to change the failure mechanisms to a large extent. This figures should be compared

with Figs 10 and 11 for the same foundation but with FBC, to get an idea of the effects of separation and sliding. Notice the following points. (a) For all combinations of Q and M the limiting values of Figs 18 and 19 decrease due to TSI, and the skewedness of the envelopes seen in Figs 10 and 11 substantially diminishes, being barely distinguishable for the smallest embedment ratios, D/B=0·2, examined. (b) The failure mechanisms at the four limit points (A–D) seem to consist of only a part of the mechanisms of the FBC analysis of Figs 10 and 11 since, as a consequence of separation, failure is restricted locally in the close vicinity of the particular interface. For instance, at point C of Q_{max} all the back side of the wall loses contact with the soil, and thus no active wedge develops.

At point B of the D/B=1 foundation, corresponding to M_{max}, the TSI mechanism in front and back of the normal-to-loading-direction sidewalls, as well as the one below the base, are almost half (in a qualitative sense) of the FBC mechanisms. The separation of the back wall is due to the combined effects of the clockwise moment M=M_{max} and the positive Q required for keeping the base horizontal translation equal to 0. A slight difference between the two soils is that the rotation pole in the inhomogeneous soil with m=10 kPa/m is on the foundation base, while in the homogeneous soil is just above the base.

On the other hand, at the M_{max} point B of the D/B=0·2 foundation, the TSI mechanism is altogether different: instead of the *scoop* mechanism of the FBC foundations of Figs 13 and 14, a *Brinch Hansen*-type (1953) wedge is evident.

At the Q_{ult} point D, there is again a slight difference between the two soils: the rotation pole in the inhomogeneous soil with m=10 kPa/m is at the surface and in the middle of the upper foundation base, while in the homogeneous soil is a bit lower and to the right.

At the M_{ult} point A, in the inhomogeneous soil with m=10 kPa/m the failure mechanism is similar to the corresponding mechanism of M_{max}, with lower uplift and the rotation pole higher above the foundation base, because of the zero horizontal force. Homogeneous soil fails with a *scoop* mechanism.

Fig. 20, show the MQ envelope for the D/B=1 for a foundation with TSI in case of inhomogeneous soil with m=2 kPa/m, along with the snapshots of the displacement vectors and the high plastic shear strain ‘shadows’. Note that results for inhomogeneous soil profile refer to safety factors FS_V against vertical bearing capacity mobilization equal to 4, or equivalently N/N_{ult}=0.25. Point (a) apply here as well.

Analytically, at point C of Q_{max} the failure mechanism is similar to the FBC mechanism, as soil in the back side of the foundation has low strength and fails for very low displacement. Consequently, active wedge develops and the gap between foundation and soil is indistinguishable. This comes in contrast with the behaviour of other soil profiles in TSI.

At point B, corresponding to M_{max}, the TSI mechanism is similar to the corresponding failure mechanism of other soil profiles. The only difference is that the foundation uplift is lower because of the greater soil plastification above the foundation base. As a result, the spheroidal shear zone haw bigger diameter and the rotation pole drives to the left.

On the other hand, at the M_{max} point B of the D/B=0·2 foundation, the TSI mechanism is altogether different: instead of the *scoop-wedge* mechanism of the FBC foundations of Fig. 12, a Brinch Hansen-type (1953) wedge is evident.

At the Q_{ult} point D, the failure mechanism is similar to the corresponding failure mechanism of the other inhomogeneous soil profile. Difference derives from the

active wedge, which develops in the soil of the foundation's back side, for very low displacement.

At the M_{ult} point A, a *scoop* failure mechanism with very low uplift is presented. Homogeneous soil fails in the same way.

Fig. 21 compares the dimensionless MQ envelopes from the FBC and the TSI analyses, for the four *D/B* ratios (0, 0·2, 0·5, 1), for inhomogeneous soil with m=10 kPa/m. Note that FBC is for N/N_{ult}=0 and TSI for N/N_{ult}=0·25. This comparison shows that the TSI curve are not only much 'contracted' compared to the FBC curves, but their shapes are also quite different, with the skewness having almost disappeared. Comparing with Fig. 22, which depicts the behaviour of homogeneous soil, it is obvious that TSI conditions have similar impact on both soil profiles.

SEISMIC RESPONSE

In the previous chapters, the response of foundations under static loading is investigated. However, the seismic response is an issue of pure dynamic nature. Seismic stimulation causes mainly transverse loading in foundation. Its kinematic and cycling character does not necessarily mean failure though. On the one hand, the structure cannot bear a load greater than its capacity. On the other hand, even if it reaches its bearing capacity, it does not indispensably fails, as it is instantly imposed loading.

Earthquake include three components, two horizontal and one vertical. Here, the seismic response of the foundations is being considered in one horizontal direction. For this reason, is presented the seismic response of the one-degree-of-freedom (1-DOF) oscillator. The model consists of a foundation supporting a simple rigid structure of mass m located at a height *h* from the foundation top. The superstructure is designed as a circular column, so the seismic study response to one direction is sufficient. Additionally, it is designed with a very high modulus of elasticity, so it is considered to be practically rigid, on purpose the column bending not to affect the results.

Results are presented for homogeneous soil (S_u=150 kPa) and inhomogeneous with m=10 kPa/m, for foundations with embedment ratio: 0·2 and 1. With the aid of this parametric investigation, becomes possible the study of response differentiation because of the various soil and embedment characteristics. Two FS_V values are considered: 2 and 5, representing, respectively, lightly loaded and heavily loaded structures. To achieve the desired FS_V, the mass is adjusted appropriately. The slenderness ratio, *h/B*, is varied parametrically: 1·25 and 2·5.

Authors explore the response for the following seismic records (Fig. 23): *LXR* (Lixouri, Kefalonia, Greece, 2014) and *Shin-Kobe* (Kobe, Japan, 1995). These two excitations have different characteristics, which affect the response of the soil-foundation-superstructure system. *Shin-Kobe* [Fig. 23(a)] is a record with 0·43 g peak acceleration and the predominant eigenperiods range from 0·3 to 0·5 s and 1·0 to 1·3 s. *LXR* record [Fig. 23(b)] has 0·65 g peak acceleration and the eigenperiods range from 0·08 to 0·2 s and 1·2 to 1·5 s.

Concerning the boundary conditions, it must be noted the release of the model in the direction of the seismic record. Kinematic commitments are placed at the lateral borders, in order to simulate realistically the free field response and dampers at the base for the proper simulation of radiation damping. The damping factor of the dampers is defined as:

$$C=\rho V_s A_d \quad (11)$$

where, ρ is the soil density (=2 Mg/m^3), V_s the propagation velocity of the shear waves at the model base (m/s) and A_d (m) the active surface of the damper. Forty to sixty groups of dampers are placed depending on the discrimination of the finite-element grid, as is required from the different foundation embedment ratios.

Hysteretic damping of the soil is considered as ξ_s=1%, in order to achieve viscoelastic behaviour in the field of small deformations. The damping of the foundation-superstructure system is equal to ξ=5% (standard concrete damping). All the results in this section, refer only to the non-linear TSI soil-foundation interaction, as defined in previous chapter. P–Δ effects are now taken into account because of the mass in the top of the column.

System Response to *Shin-Kobe*

Slenderness ratio h/B=1·25 & FS$_V$=2. Fig. 24 depicts accelerograms for two soil profiles (homogeneous soil and Gibson soil with m=10 kPa/m) and two embedment ratios (0·2 and 1). The lines refer to three model points [top of the structure (top), top of foundation (cp) and a specific free field point (ff)]. As for the soil response, it is obvious that the inhomogeneous soil profiles present higher peak values (0·74 g) in contrast to homogeneous soil, which give a peak value of 0·39 g. This difference can be explained because of the loose soil, which does not have enough stiffness to react to the motion. Similar is the response of the (cp) point, which is higher for the Gibson soil and the lower embedment ratio (0·39 g). As for the mass acceleration, there is no big difference between the models, as the bigger acceleration (0·26 g) comes out from the homogeneous profile and the D/B=1. Note that the mass accelerogramms present high periods, because the low FS$_V$ (heavy mass) leads to high plastification of the soil and it increases the period of the system (as the displacement of the superstructure top increases) out of the record's predominant period range. In fact, system periods exceed 2 s and this leads to de-amplification of superstructure's acceleration.

Fig. 25 shows the normalised settlement (w/B) – rotation angle (θ) fluctuation of the foundation control point for all models. It is obvious that, high embedment ratios present smaller residual settlements. Additively, Gibson soil models present smaller residual settlements and higher rotation angles (0·015 rad instead of 0·0075 rad for the homogeneous soil models).

Fig. 26 depicts normalised moment (M/BAS_u) – rotation angle (θ) loops of the foundation control point for all models. Note that all moment normalisations are made for a value of S_u in depth B. So for homogeneous soil profiles S_u=150 kPa and for Gibson soil profiles S_u=mB. It is noticeable that, homogeneous soil profiles (and especially foundation with D/B=1) present bigger M–θ loops, which means the soil–foundation system dissipates larger amount of energy during seismic motion in comparison with the loose Gibson soil.

Slenderness ratio h/B=1·25 & FS$_V$=5. Fig. 27 depicts accelerograms for the two soil profiles, the two embedment ratios and the three selected points. The free field response presents similar behaviour with the corresponding behaviour for the lower FS$_V$. Indeed, the inhomogeneous soil profile present higher peak values (0·74 g) in contrast to homogeneous soil which gives a peak value of 0·43 g. As for the (cp) point, higher is the response of the homogeneous soil (0·75 g), while in the Gibson

soil appears a high 0·62 g. The embedment ratio does not play an important role to this result. In contrast to previous section, is presented amplification in the superstructure top in almost all models, with max acceleration in inhomogeneous soil profile for D/B=1 (1·31 g). This is logical, as light mass, pushes to lower horizontal displacements, lower soil plastification and lower system periods, which are in the range of the record's predominant period range (0·3 to 0·8 s). So the amplification comes as a logical impact, while the mass accelerograms present low predominant periods. Gibson soil profiles present higher values of acceleration. As for the homogeneous soil profile with the low embedment ratio, there is no amplification because even in this vertical safety factor, top mass is heavy and so the behaviour of previous section is presented.

Fig. 28 shows the normalised settlement (w/B) – rotation angle (θ) fluctuation of the foundation control point for all models. High FS_V leads foundations to smaller residual settlements. Especially, Gibson soil present higher residual settlements (w_{max}/B=0·00035 for D/B=0·2), because of the lower soil strength, which leads to higher soil plastification. On the other hand, homogeneous soil models present a particular behaviour, semi-sinking and semi-uplifting. Low embedment foundation gives normalised uplifting up to 0.006 and ends with a normalised settlement of 0.00025. Foundation with D/B=1 presents a more sinking behaviour as it has very low uplifts (up to 0.0002B) and ends with a very low settlement (0.00015B), even if in case of a seismic pulse foundation sinked 0.002B. Therefore, foundation with low embedment ratio has again higher settlement. It must be noted that low rotation angles exist, which can be explained because of the small top mass. Foundation with D/B=0·2 in homogeneous soil presents the maximum residual rotation angle (0·005 rad), which is almost the half of previous section.

Fig. 29 depicts normalised moment (M/BAS_u) – rotation angle (θ) loops of the foundation control point for all models. These M–θ loops are narrow (in contrast to previous section), because smaller top masses lead to less soil plastification, and less consumed energy. Contribution to the latter behaviour have the small rotation angles that are presented in this section.

Slenderness ratio h/B=2·5 & FS_V=2. Fig. 30 illustrates accelerograms for the two soil profiles, the two embedment ratios and the three selected points. The inhomogeneous soil profiles present higher peak values (0·74 g) in contrast to homogeneous soil, which give a peak value of 0·39 g. Similar is the response of the (cp) point, which is higher for the Gibson soil and the lower embedment ratio (0·48 g). As for the mass acceleration, there is no big difference between the models, as the bigger acceleration (0·15 g) comes out from the homogeneous soil model with a D/B=1 foundation, while Gibson soil profiles present a peak value of 0·14 g. In previous section, with the same FS_V and half slenderness ratio, maximum mass acceleration is about 1·7 times higher (0·26 g). This probably has the following explanation: higher superstructure leads to lower stiffness of structure and higher initial period of system. As top moves horizontally, soil plastification increases and the system period increases faster than in the case of lower slenderness ratio. As a result, system period comes out of the record's predominant period range with less mass horizontal displacement. In other words, same mass horizontal displacement leads to higher system periods in case of

higher superstructure. At last, it could be useful to notice that mass accelerogram generally presents phase angle 90^{o} in comparison with the other point accelerograms. This is a result of the high slenderness ratio and the high system period.

Fig. 31 shows the normalised settlement (w/B) – rotation angle (θ) response of the foundation control point for all models. Here, homogeneous soil models present higher residual rotation angles, as a result of the higher superstructure. Oppositively, Gibson soil models present decreased residual rotation angles possibly because of the record period content. It is noticed that during last record pulses the rotation angle is decreased and remains to half the angle (0·0075 rad) of the first section. As for the settlements, foundation embedment ratio does not follow a certain pattern, but it is obvious that all (cp) points sink less than in case of the taller superstructure. This behaviour may have the following explanation: for an imposed large angle of rotation, the total moment atop the foundation is almost equal in two cases (h/B=1·25 and 2·5); however, the contribution to this moment of the (vertical) weight W (P–Δ effect) is 2 times larger for the taller (h/B=2·5) structure, and the corresponding moment because of the horizontal force is 2 times smaller. Therefore, the horizontal shear force $Q=M/h$ developing atop the foundation of the taller system is slightly smaller than the one coming from the shorter one. Consequently, in the latter case, the increased Q leads to greater inelastic action in the soil, leading to greater residual settlement.

Fig. 32 illustrates normalised moment (M/BAS_u) – rotation angle (θ) loops of the foundation control point for all models. In this section, M–θ loops have similar shape as in the first section but in all cases, they present slight moment increases (because of the higher slenderness ratio), although the top mass acceleration values are lower.

System Response to *LXR*

Slenderness ratio h/B=1·25 & FS_V=2. Fig. 33 presents accelerograms for the two soil profiles (homogeneous soil and Gibson soil with m=10 kPa/m) and the two embedment ratios (0·2 and 1). It is obvious that inhomogeneous soil profiles give higher peak values (0·76 g) in contrast to homogeneous soil which gives a peak value of 0·54 g. This is a pattern that appeared also in the previous record. As for the (cp) point, maximum acceleration value gives the homogeneous soil model with the foundation of low embedment ratio (0·47 g). It must be noticed that models have 0·3 to 0·47 g peak values and their peak values are close enough, so a conclusion cannot drawn. As for the mass acceleration, there is no big difference between the models, as the bigger acceleration (0·26 g) comes out from the homogeneous profile and the D/B=1 (same foundation in Gibson soil gives a maximum value of 0·24 g). On the other hand, the other models present 0·20 g, so all peak values are close. The de-amplification is due to the reasons that explained in previous sections.

Fig. 34 shows the normalised settlement (w/B) – rotation angle (θ) response of the foundation control point for all models. As for the rotation angle, all models present low residual angles. Nevertheless, Gibson soil models present larger angles and maximum residual angle has the model of Gibson soil with the foundation of D/B=0·2 (0·005 rad). Regarding to the results, settlements increase in homogeneous soil and maximum residual settlement has the foundation with D/B=1 (0·013B).

Fig. 35 depicts normalised moment (M/BAS_u) – rotation angle (θ) loops of the foundation control point for all models. All moment normalisations are made for a value of S_u in depth B. So for homogeneous soil profiles S_u=150 kPa and for Gibson soil profiles $S_u=mB$. It is obvious that, homogeneous soil profiles (and especially foundation with D/B=1) present bigger M–θ loops, which means the soil–foundation

system dissipates larger amount of energy during seismic motion in comparison with the loose Gibson soil.

Slenderness ratio h/B=1·25 & FS_V=5. Fig. 36 depicts accelerograms for two soil profiles and two embedment ratios. Inhomogeneous soil profile presents higher peak values (0·76 g) in contrast to homogeneous soil which gives a value of 0·54 g. The (cp) point of foundation with *D/B*=0·2 embedded in homogeneous soil gives the maximum acceleration (0·81 g). Amplification is presented in the superstructure top in almost all models, with max acceleration in inhomogeneous soil profile for *D/B*=1 (0·99 g). This is logical, as light mass, pushes to lower horizontal displacements, lower soil plastification and lower system periods, which are in the range of the record's predominant period range. So the amplification comes as a logical impact, while the mass accelerograms present low predominant periods. Gibson soil profiles present again higher values of acceleration. As for the homogeneous soil profile with the low embedment ratio, there is no amplification because even in this vertical safety factor, top mass is heavy and so the behaviour of previous section is presented.

Fig. 37 shows the normalised settlement (*w/B*) – rotation angle (θ) fluctuation of the foundation control point for all models. High FS_V leads foundations to smaller residual settlements. Especially, Gibson soil present higher residual settlements (w_{max}/B=0·0004 for *D/B*=0·2), because of the lower soil strength, which leads to higher soil plastification. On the other hand, homogeneous soil models present a particular behaviour, semi-sinking and semi-uplifting. Low embedment foundation gives normalised uplifting up to 0·007 and ends with a normalised settlement of 0·001. Foundation with *D/B*=1 presents a more sinking behaviour as it has very low uplifts and ends with a very low residual settlement (0·0001*B*), even if in case of a seismic pulse foundation sinked 0·00016*B*. Therefore, foundation with low embedment ratio has again higher settlement. Note that low residual rotation angles exist, which can be explained because of the small top mass. Foundation with *D/B*=0·2 in homogeneous soil presents the maximum residual rotation angle (0·0015 rad), which is almost the 1/3 of previous section.

Fig. 38 depicts normalised moment (M/BAS_u) – rotation angle (θ) loops of the foundation control point for all models. These $M–\theta$ loops are narrow in contrast to previous section, because smaller top masses lead to less soil plastification, and less consumed energy. Furthermore, the small rotation angles that are presented in this section, contribute to the loop shrinkage.

Slenderness ratio h/B=2·5 & FS_V=2. Fig. 39 illustrates accelerograms for two soil profiles and two embedment ratios. As for the soil response, it is obvious that in inhomogeneous soil profile presents higher peak values (0·76 g) in contrast to homogeneous soil which gives a value of 0·54 g. This difference can be explained because of the loose soil, which does not have enough stiffness to react to the motion. Similar is the response of the (cp) point, which is reasonably higher for the Gibson soil and the lower embedment ratio (0·45 g). As for the mass acceleration, there is no big difference between the models, as the bigger acceleration (0·16 g) comes out from the homogeneous profile and the *D/B*=1. In previous section, with the same FS_V and half slenderness ratio, maximum mass acceleration is about 1·6 times higher (0·26 g).

This ratio is almost equal to the ratio exacted for the *Shin-Kobe* stimulation. Phase angle 90^o dominates again.

Fig. 40 shows the normalised settlement (w/B) – rotation angle (θ) response of the foundation control point for all models. Here, models with the same embedment ratio present almost equal residual rotation angles. As for the settlements, foundation embedment ratio does not follow a certain pattern, but it is obvious that all (cp) points sink less than in case of the taller superstructure. This behaviour has been explained in previous sections.

Fig. 41 illustrates normalised moment (M/BAS_u) – rotation angle (θ) loops of the foundation control point for all models. In this section, $M–\theta$ loops have similar shape as in the first section but in all cases, they present slight moment increases (because of the higher slenderness ratio), although the top mass acceleration values are lower.

SUMMARY & CONCLUSIONS

This article is an attempt to investigate the static and seismic response of square foundations embedded in Gibson soil. For this reason, 3D FEA models were developed. As for the static response, emphasis was given to the bearing horizontal and rotational capacity, while studying the role of the vertical load. Furthermore, horizontal and rotational elastic stiffness were investigated. The fluctuation of these results with the soil heterogeneity was the keypoint of this study. Parametrical equations related to the bearing capacity and the elastic stiffness (normalised with the soil heterogeneity or the shear modulus) as functions of embedment ratio were introduced, proving their independence from the soil inhomogeneity or the shear modulus.

Failure envelopes for various *NQM* loadings are presented, while soil–foundation interface properties play important role and they are studied analytically. All these results are presented in comparison with the corresponding analyses for homogeneous soil of Ntritsos *et al.* (2015), in order to obtain global perspective on the issue.

Subsequently, seismic response of homogeneous and Gibson soil–foundation–superstructure system is studied. Two seismic records are selected for this reason. Accelerograms for different point models, settlement–rotation angle and M–θ loops of the foundation are depicted. Parametric analyses are presented as function of the vertical static factor of safety (FS_V), the superstructure slenderness ratio and the foundation embedment ratio. It seems that different values of these parameters affect the system in many ways.

Specifically, low FS_V leads to low accelerations at top of the superstructure, while high FS_V leads to amplification. High slenderness ratio of superstructure decreases the atop acceleration and increases the response period. Embedment ratio and soil heterogeneity do not seem to play an important role on this matter. Nevertheless, inhomogeneous soil with low bearing capacity leads to high free field accelerations.

As for the foundation–superstructure settlements, low FS_V leads to increased settlements, while high FS_V reduces them and makes possible the foundation uplift. Increased embedment and slenderness ratio generally reduces settlements. Soil heterogeneity does not introduce a certain behaviour pattern.

Rotation angles are affected significantly from low FS_V, because P–Δ effects are increased. Furthermore, soil heterogeneity in most cases leads to larger foundation rotations.

FS_V affects significantly the shape of M–θ loops. Low static factor leads to increased soil plastification and moment M. High embedment ratio results to the same behaviour. Slenderness ratio increases the size of loops while soil heterogeneity reduces it.

FIGURES

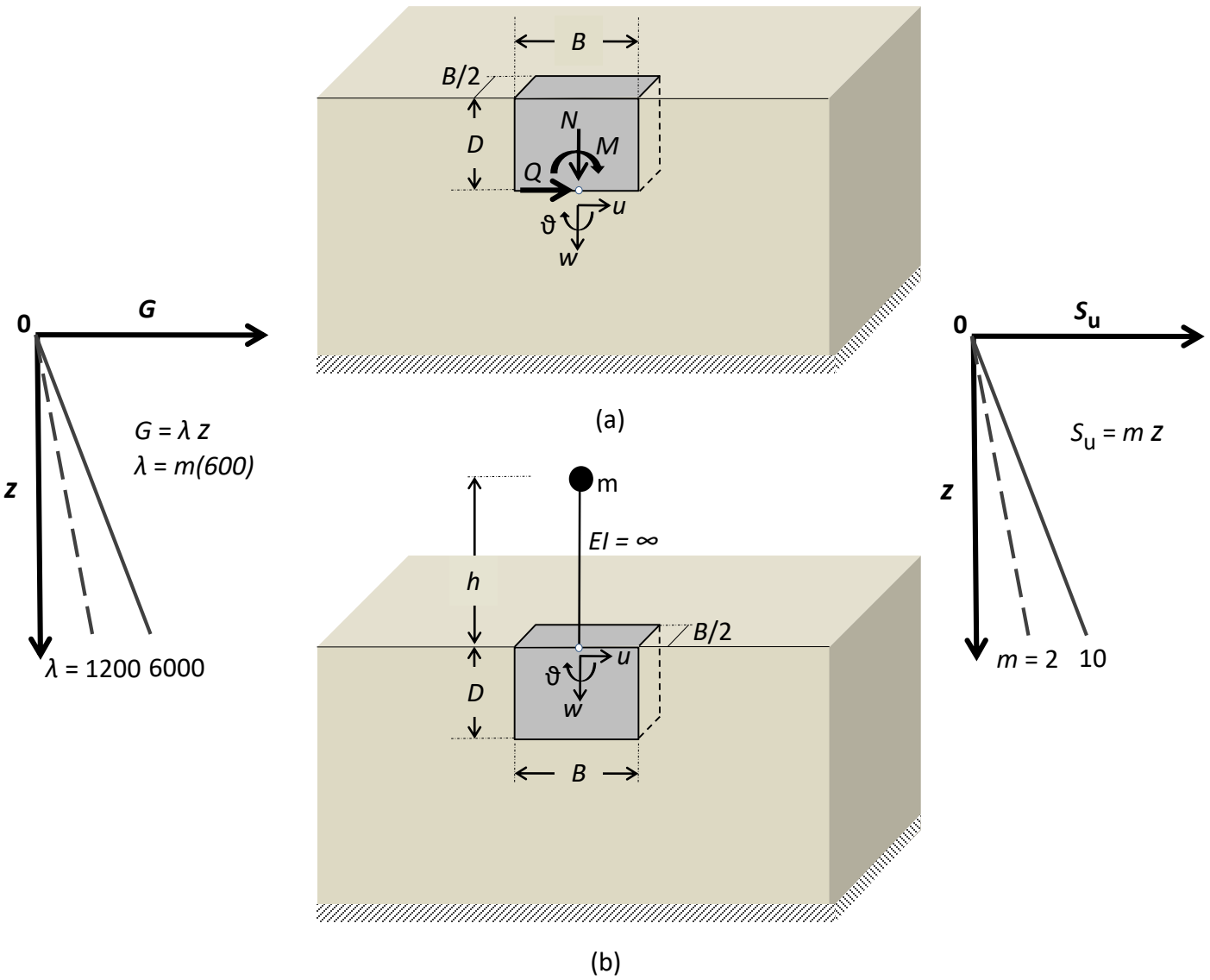

Fig. 1. Problem definition and symbols: (a) soil–foundation system (load and displacement reference point at the base of the foundation); (b) soil–foundation–structure system [load and displacement reference point at base of the structure (top of foundation)]

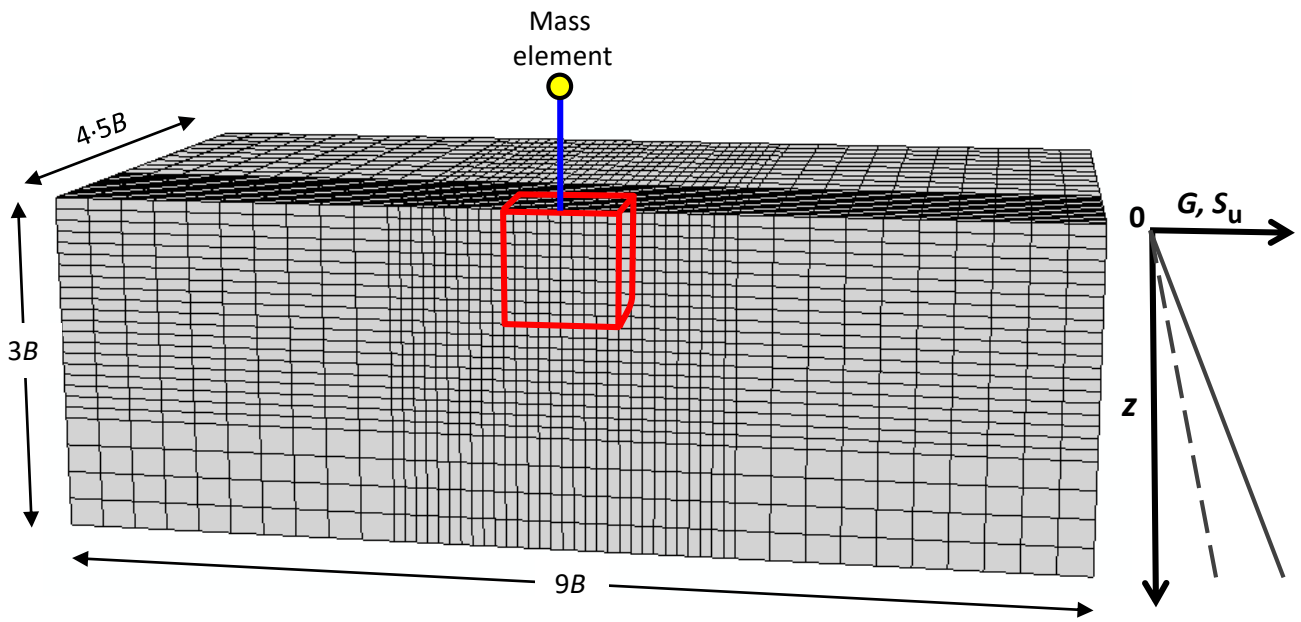

Fig. 2. Outline and dimensions of three-dimensional FE model

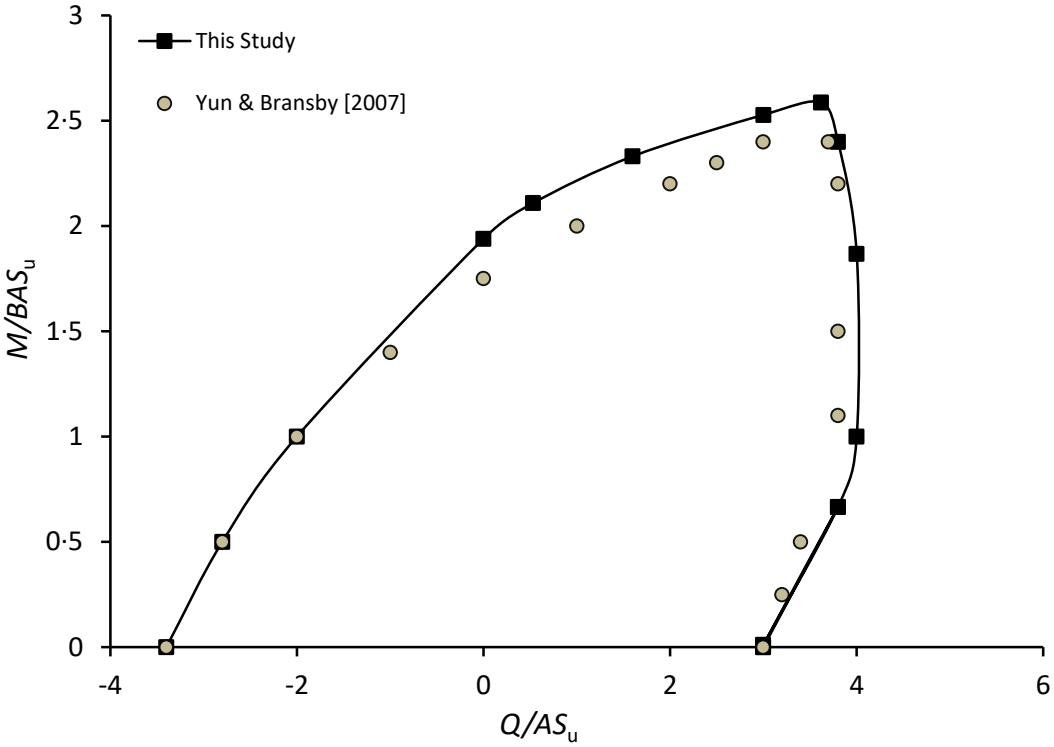

Fig. 3. Model validation for the 2D plane-strain problem with D/B=1 and N/N_{ult}= 0: comparison of MQ failure envelope of Yun & Bransby (2007) (points) with the terminal points of swipe and probe lines (continuous line) of our analysis

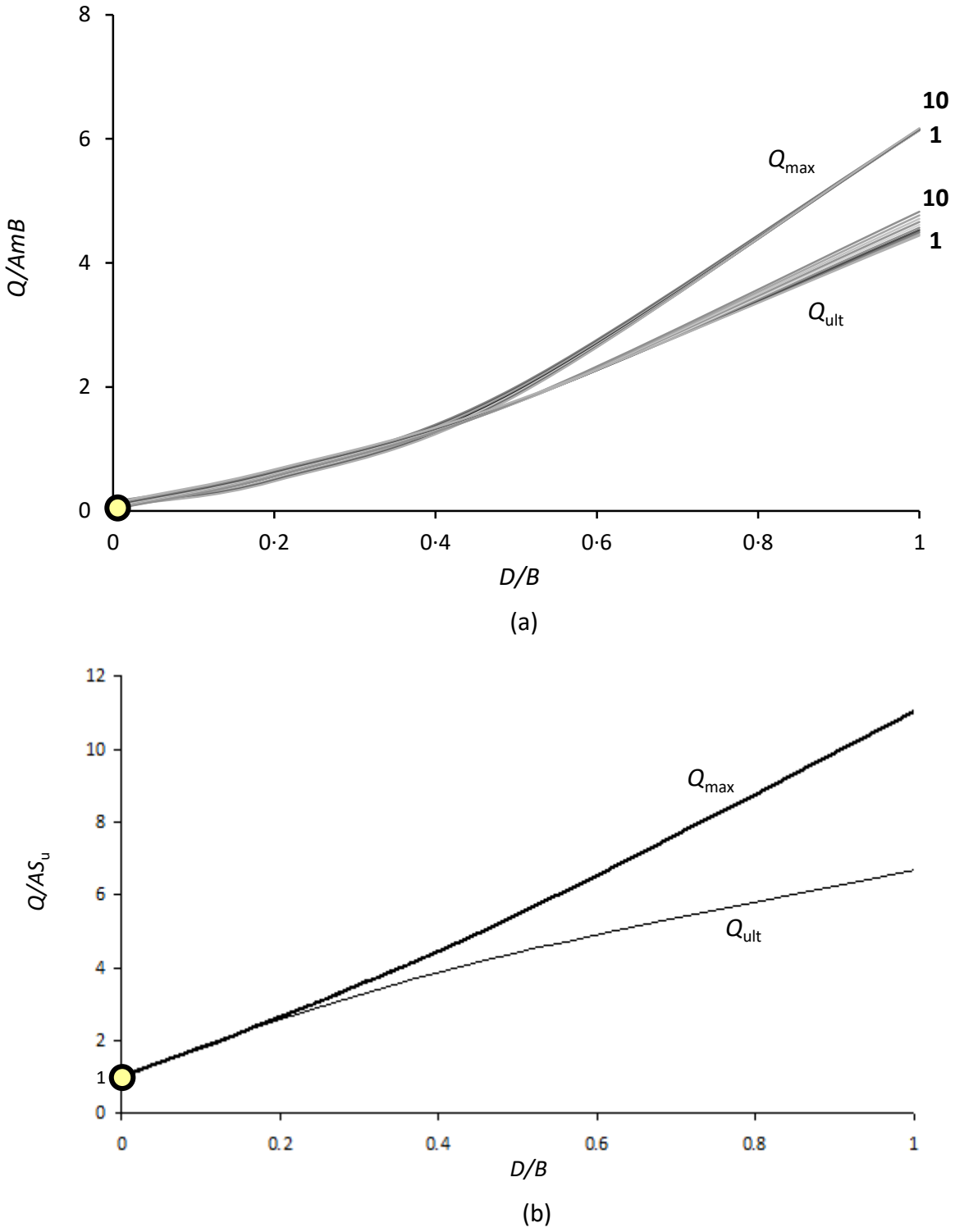

Fig. 4. The horizontal capacity Q_{max} (zero rotation): (a) Gibson soil for various degrees of inhomogeneity (10 values of *m*, from 1 to 10 kPa/m), and (b) homogeneous soil (Ntritsos *et al.*, 2015). Both results are presented as functions of the embedment ratio *D/B*. (FBC, *N*=0).

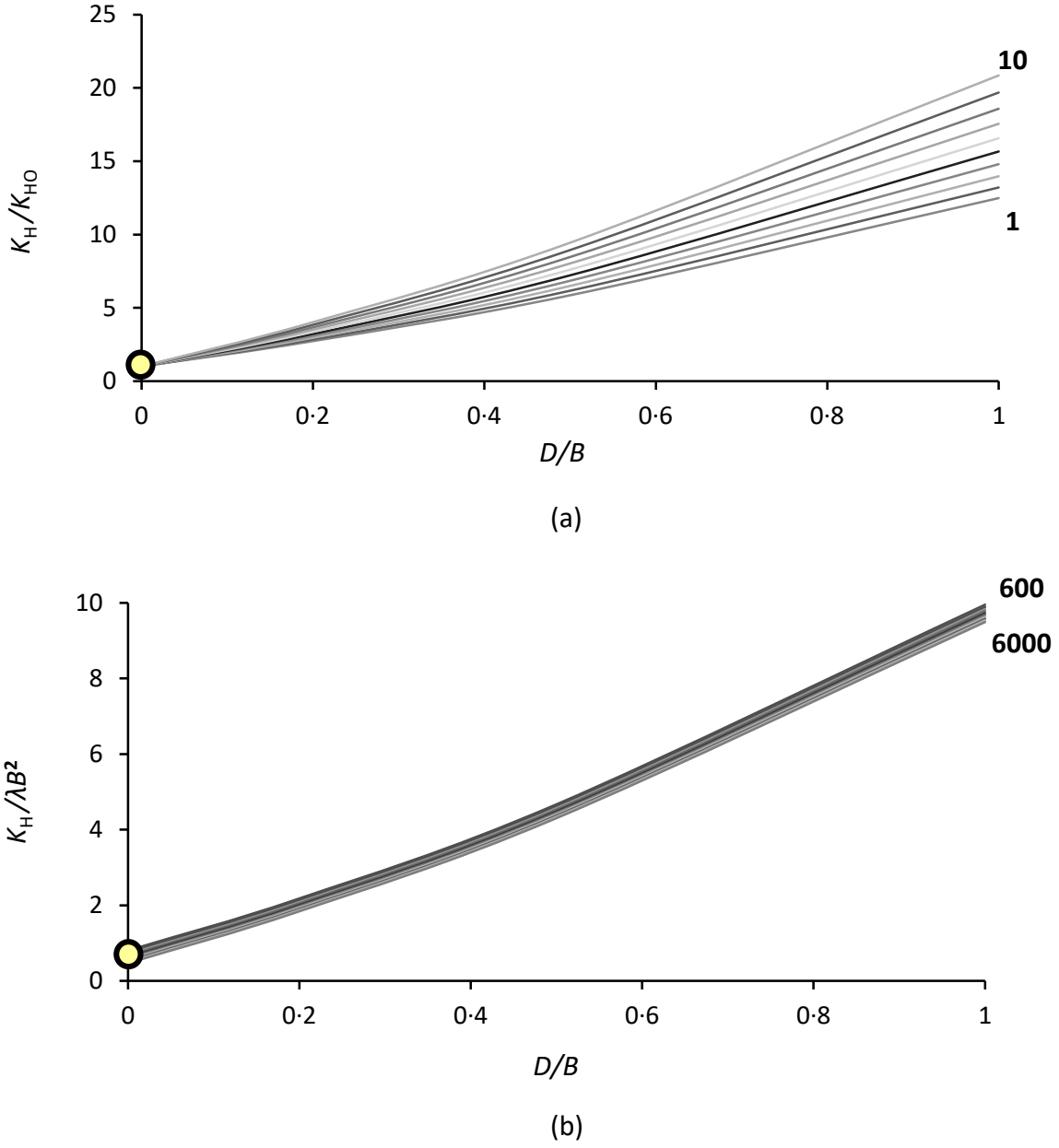

Fig. 5. The horizontal stiffness K_H of embedded foundation: (a) over horizontal stiffness K_{HO} of surface foundation (10 values of m, from 1 to 10 kPa/m); (b) over λB^2 (10 values of λ, from 600 to 6000 kPa/m). Both results are presented as functions of the embedment ratio D/B. (FBC, N=0).

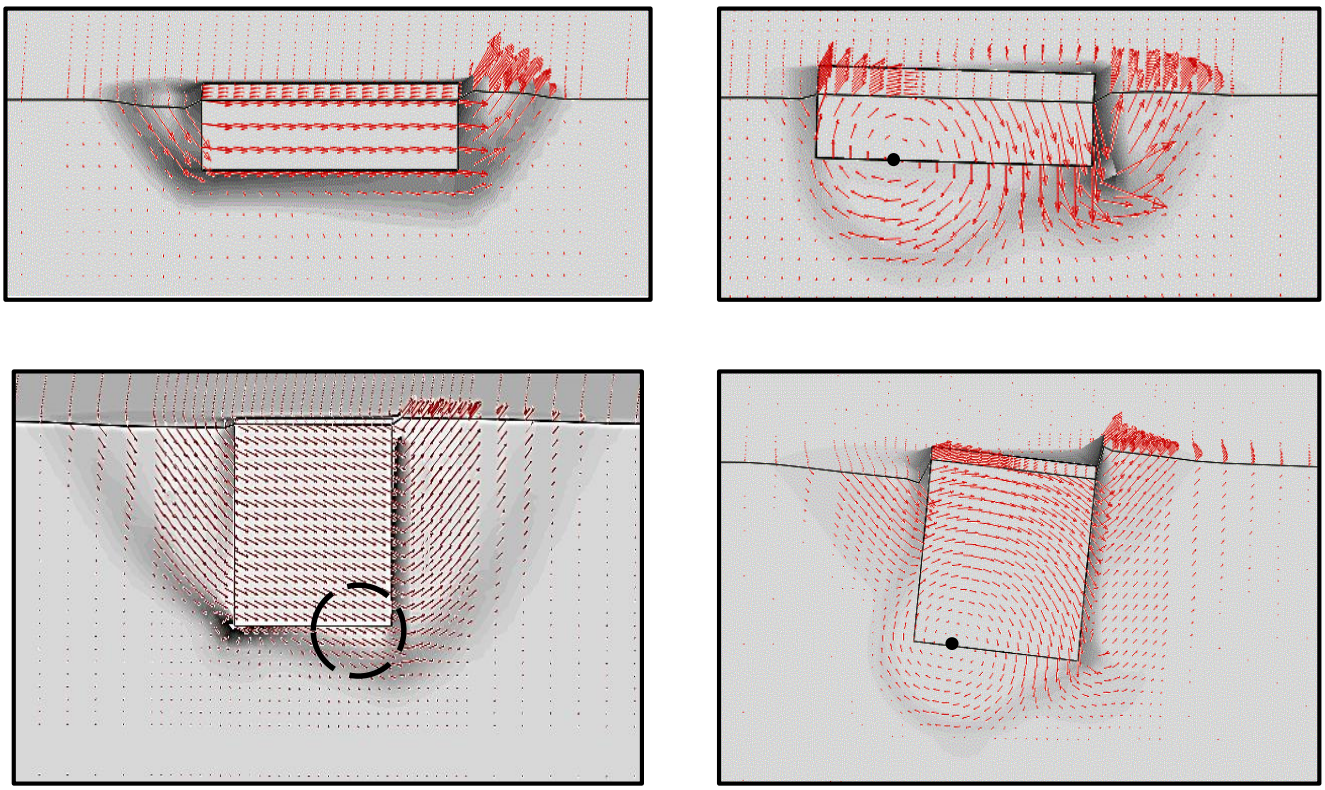

Fig. 6. Displacement vectors at two failure loads in inhomogeneous soil with m=2 kPa/m: (a) at Q_{max} (with zero rotation); (b) at M_{max} (with zero horizontal displacement). Top row: D/B=0·2; bottom row D/B=1. Grey shades indicate the location of high concentration of shear strains, revealing the failure mechanisms. The interceding black circle presents the drifting small mass of non-plastificated soil. FBC

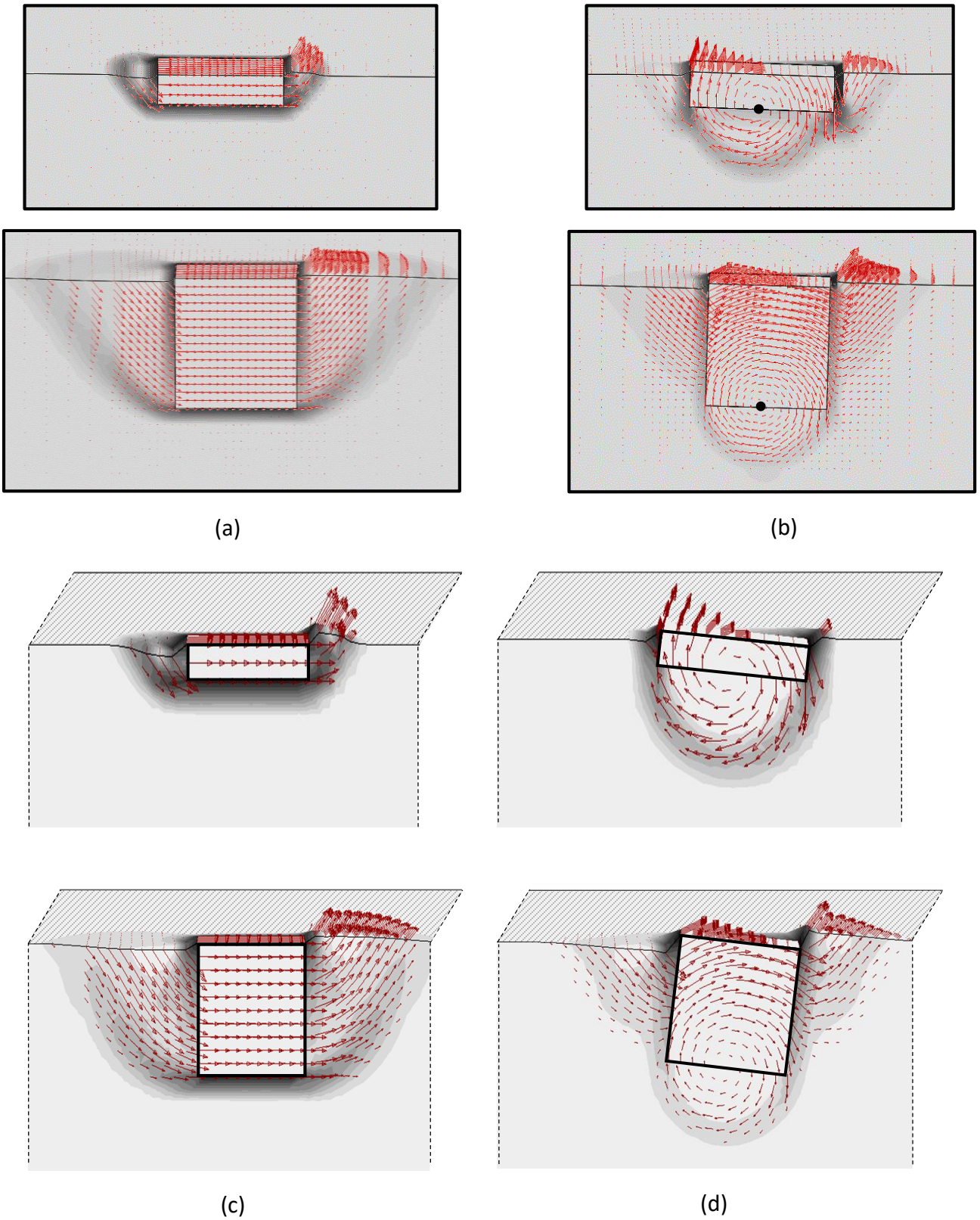

Fig. 7. Displacement vectors at two failure loads in Gibson soil with *m*=10 kPa/m (a, b) and homogeneous soil (c, d from Ntritsos *et al.*, 2015): (a, c) at Q_{max} (with zero rotation); (b,d) at M_{max} (with zero horizontal displacement). Top row: *D/B*=0·2; bottom row *D/B*=1. Grey shades indicate the location of high concentration of shear strains, revealing the failure mechanisms. FBC

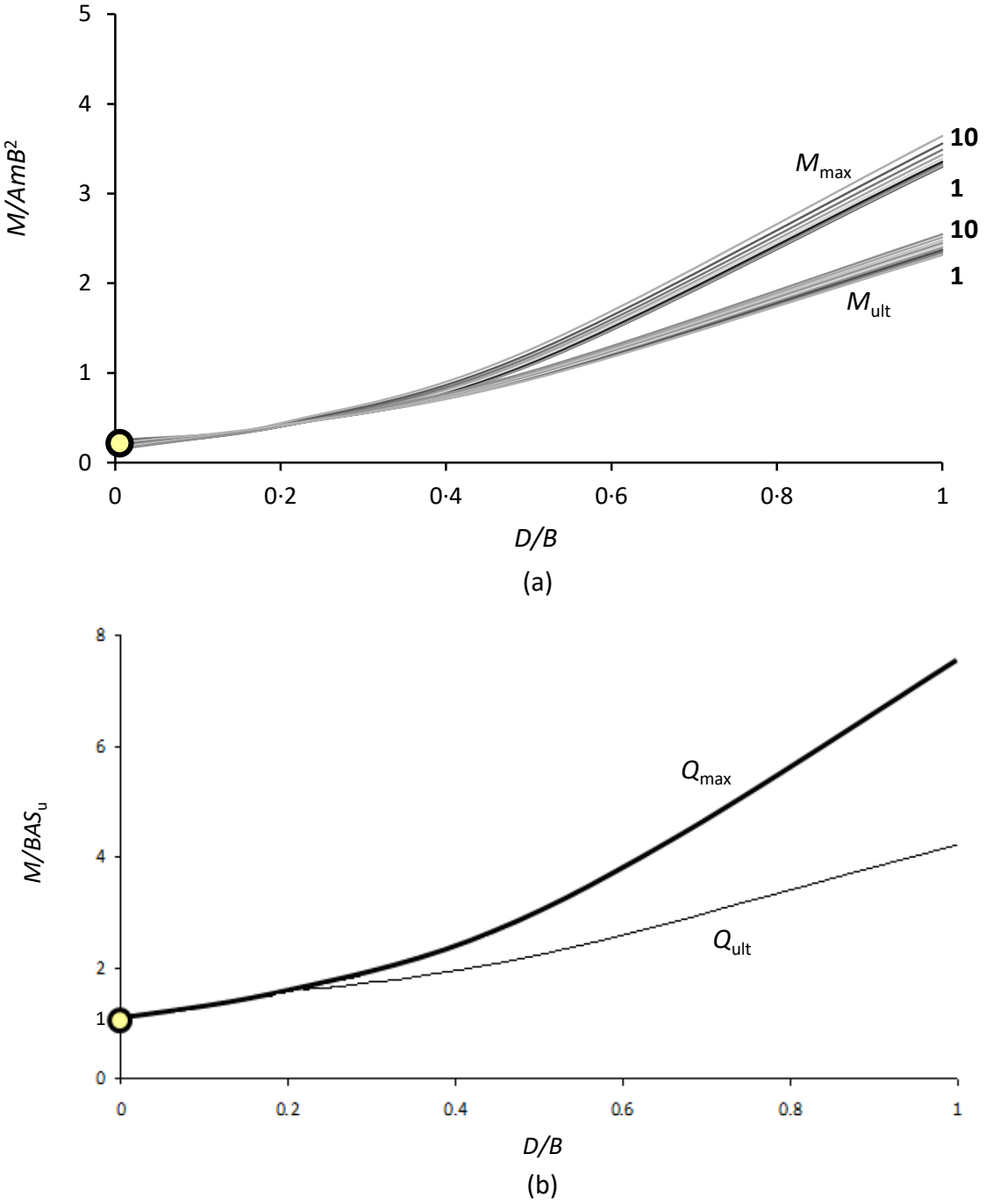

Fig. 8. The rotational capacity M_{max} (zero horizontal displacement): (a) Gibson soil for various degrees of inhomogeneity (10 values of *m*, from 1 to 10 kPa/m), and (b) homogeneous soil (Ntritsos *et al.*, 2015). Both results are presented as functions of the embedment ratio *D/B*. FBC, *N*=0

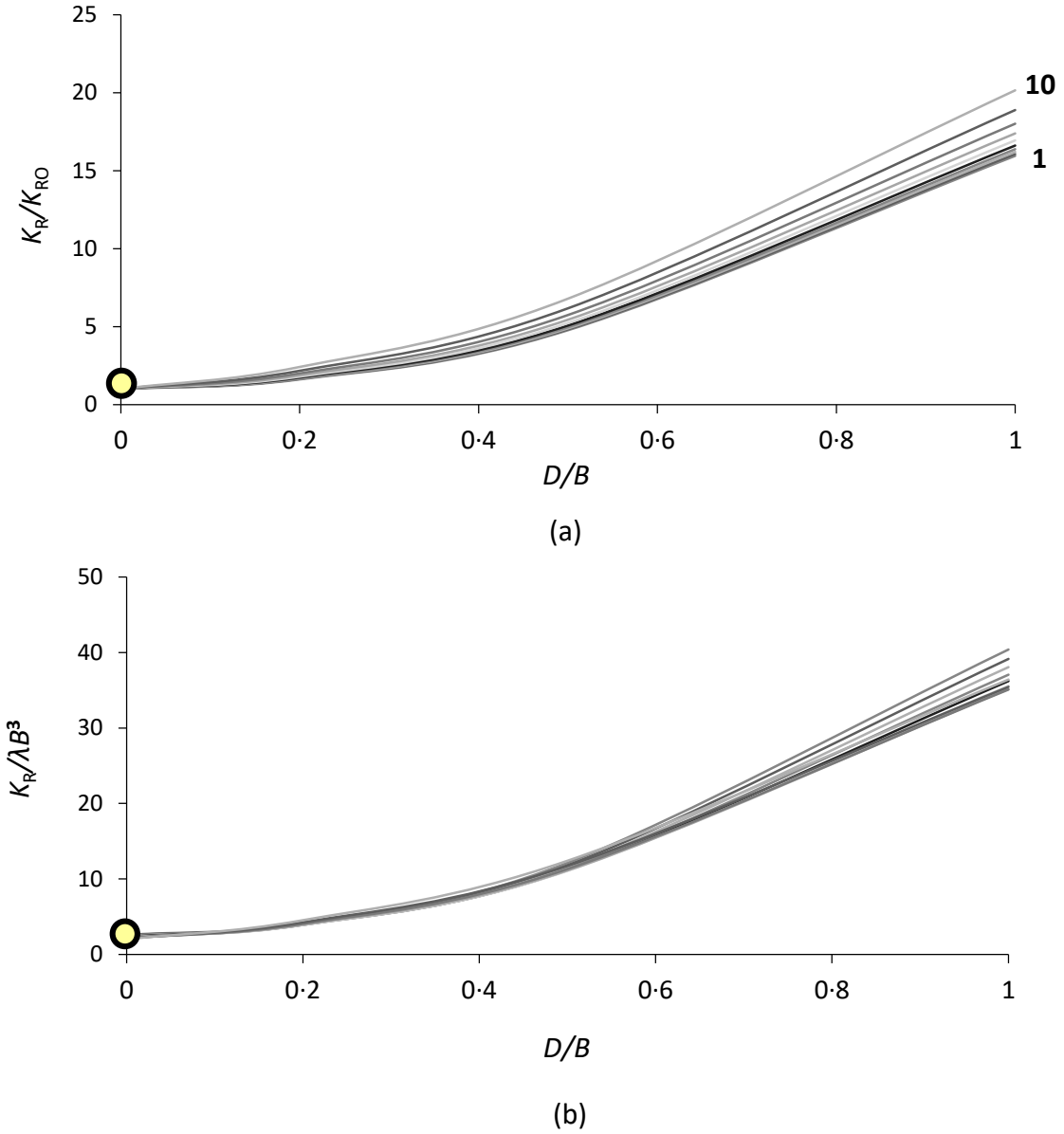

Fig. 9. The rotational stiffness K_R of embedded foundation: (a) over rotational stiffness K_{RO} of surface foundation (10 values of m, from 1 to 10 kPa/m); (b) over λB^3 (10 values of λ, from 600 to 6000 kPa/m). Both results are presented as functions of the embedment ratio D/B. (FBC, N=0).

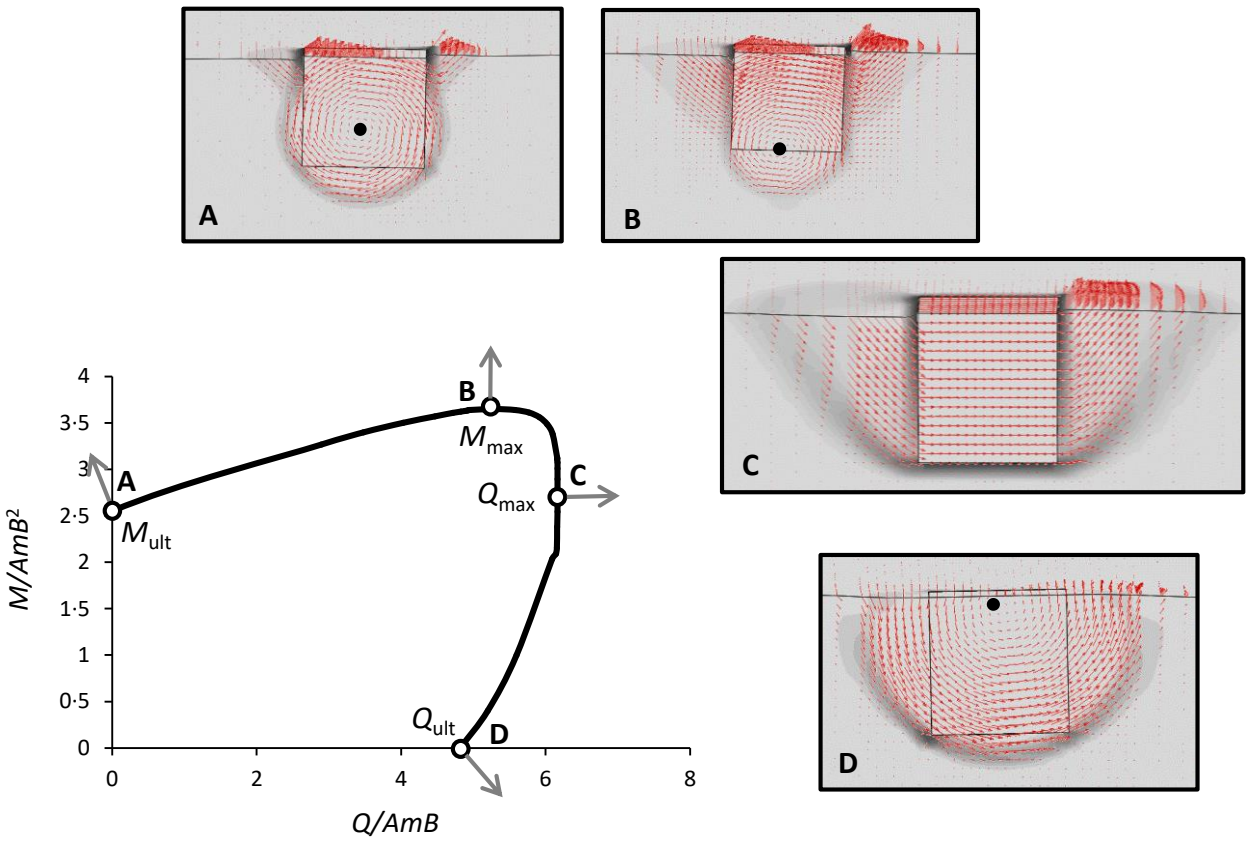

(a)

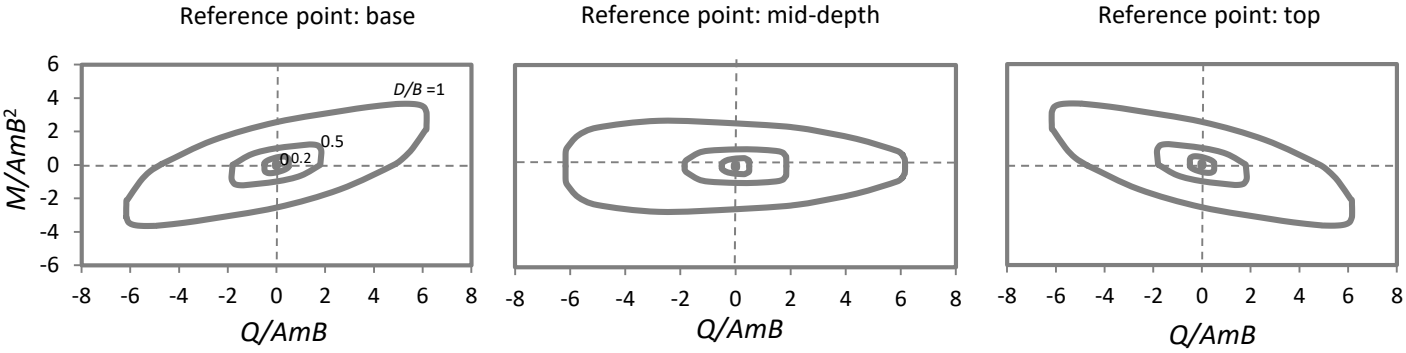

(b)

Fig. 10. (a) *MQ* interaction (failure envelope) (inhomogeneous soil with *m*=10 kPa/m) with the direction of plastic deformations at four key points, along with displacement vectors and concentration of shear strains revealing the failure mechanisms at the above four points. FBC, *D*/*B*=1. The solid dots in the pictures represent the instantaneous rotation pole of the foundation. (The pole is at infinity for the horizontal translation case, C.) (b) change of the form of the interaction *MQ* diagrams by changing the reference point (left: foundation base (see Fig. 1) as with the previous figures; middle: centre of gravity (mid-depth) of the foundation; right: foundation top surface).

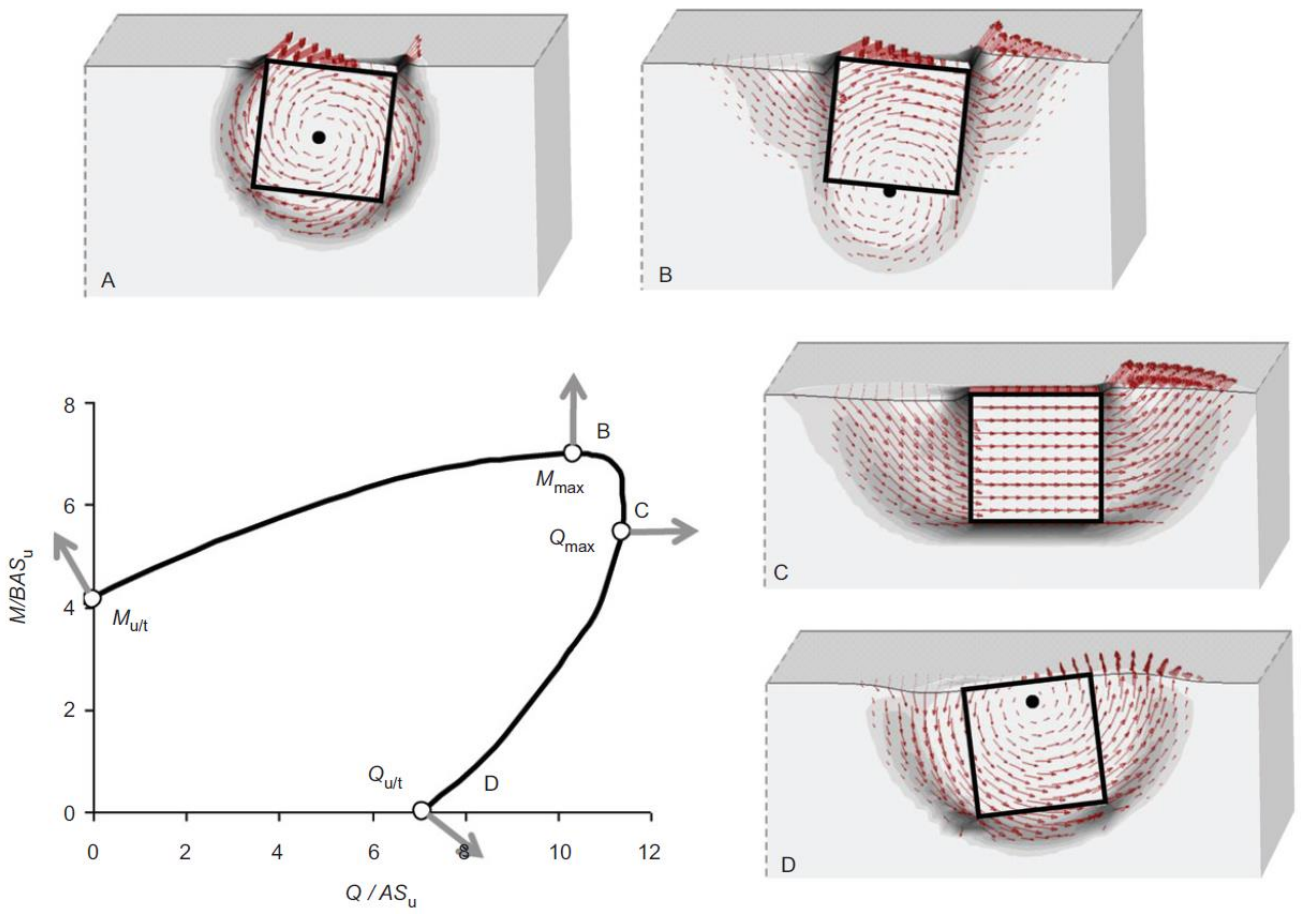

(a)

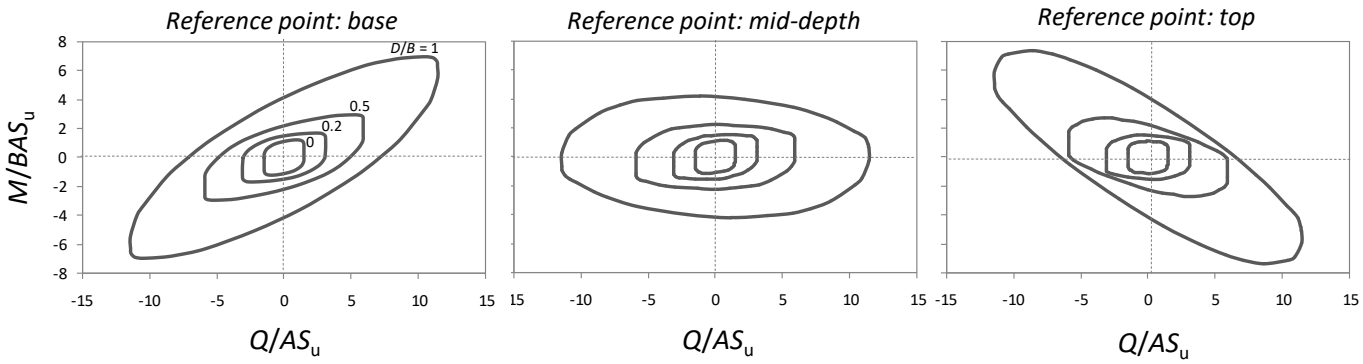

(b)

Fig. 11. (a) *MQ* interaction envelope of homogeneous soil (Ntritsos *et al.*, 2015) with the direction of plastic deformations at four key points, along with displacement vectors and concentration of shear strains revealing the failure mechanisms at the above four points. FBC, *D*/*B*=1. The solid dots in the pictures represent the instantaneous rotation pole of the foundation. (The pole is at infinity for the horizontal translation case, C.)(b) change of the form of the interaction *MQ* diagrams by changing the reference point (left: foundation base (see Fig. 1) as with the previous figures; middle: centre of gravity (mid-depth) of the foundation; right: foundation top surface).

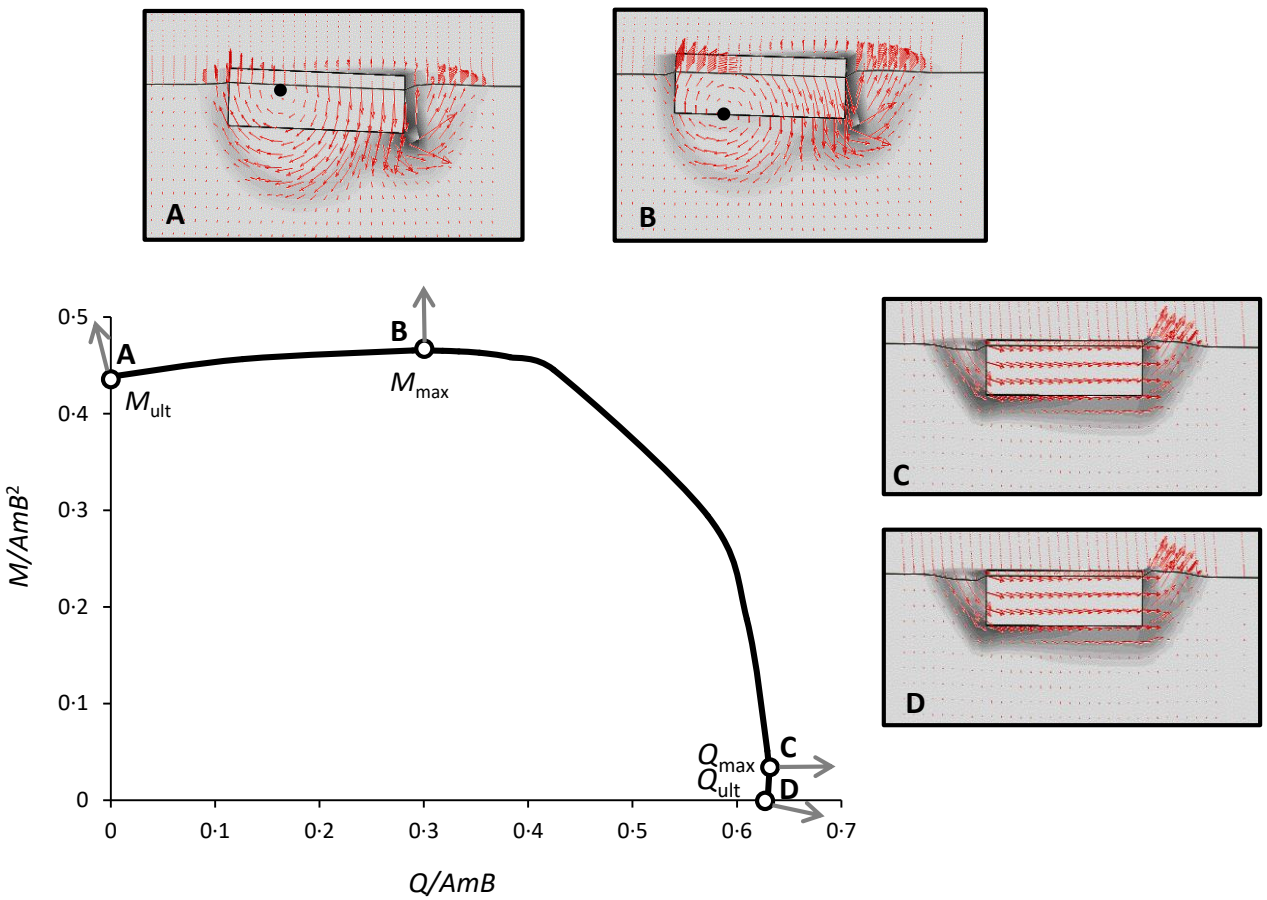

Fig. 12. Graphical representation of *MQ* interaction envelope (inhomogeneous soil with *m*=2 kPa/m) with the direction of plastic deformations at four key points. Four offset diagrams show displacement vectors and concentration of shear strains revealing the failure mechanisms at these points. FBC, *D*/*B*=0·2. The solid dots in the pictures represent the instantaneous rotation pole of the foundation. (The pole is at infinity for the horizontal translation case, point C, and "almost" infinity at point D.)

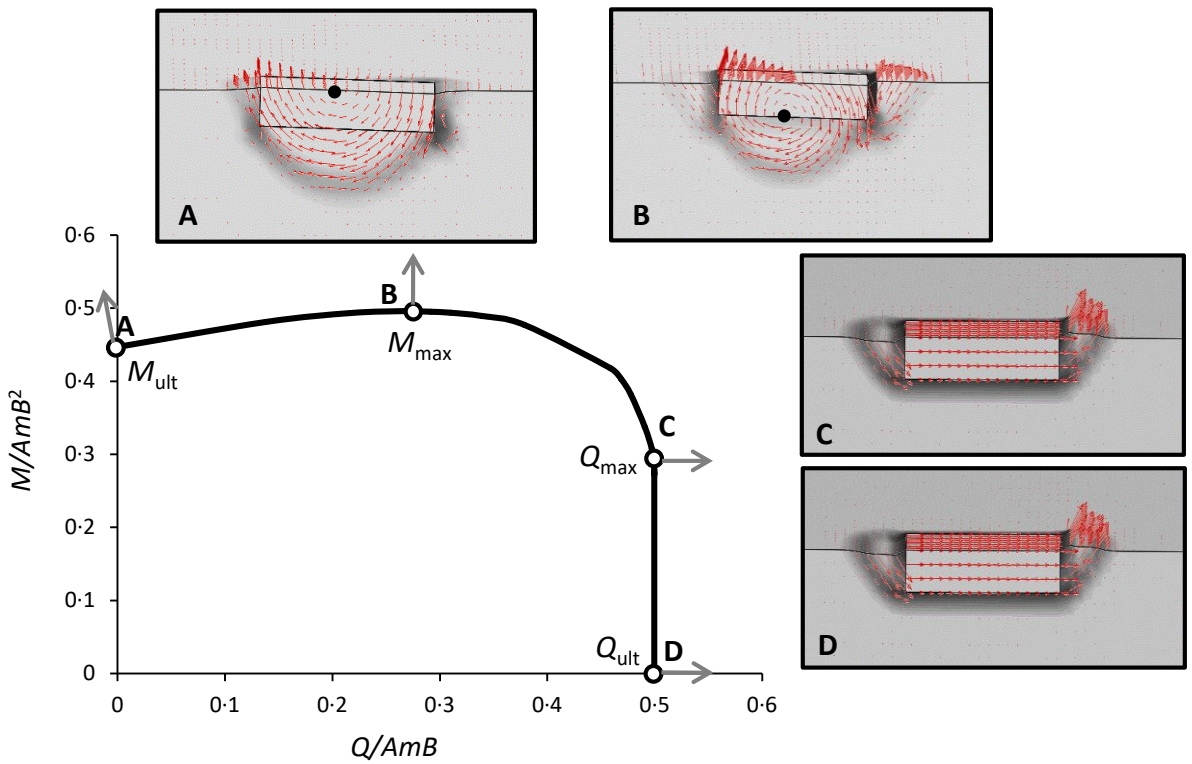

Fig. 13. Graphical representation of *MQ* interaction envelope (inhomogeneous soil with *m*=10 kPa/m) with the direction of plastic deformations at four key points. Four offset diagrams show displacement vectors and concentration of shear strains revealing the failure mechanisms at these points. FBC, *D*/*B*=0·2. The solid dots in the pictures represent the instantaneous rotation pole of the foundation. (The pole is at infinity for the horizontal translation case, point C, and "almost" infinity at point D.)

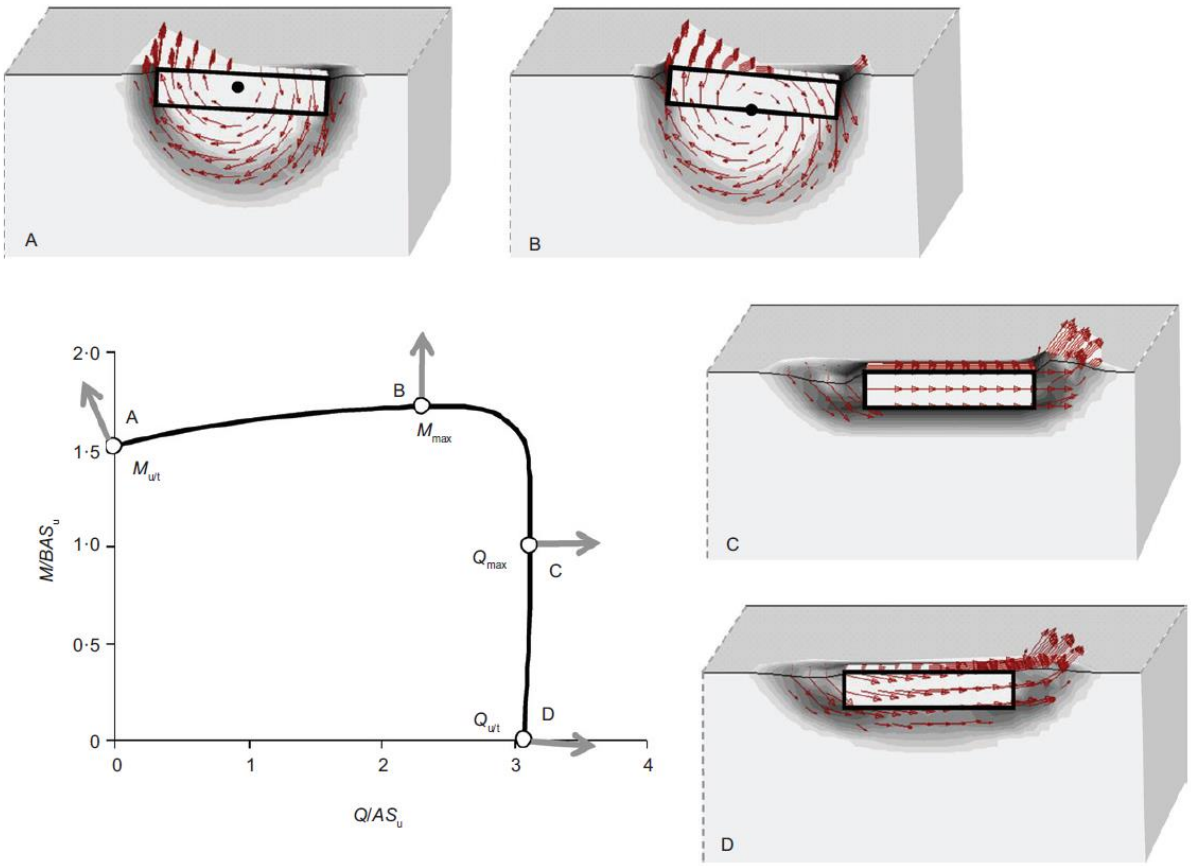

Fig. 14. Graphical representation of *MQ* interaction envelope (homogeneous soil, Ntritsos *et al.*, 2015) with the direction of plastic deformations at four key points. Four offset diagrams show displacement vectors and concentration of shear strains revealing the failure mechanisms at these points. FBC, *D*/*B*=0·2. The solid dots in the pictures represent the instantaneous rotation pole of the foundation. (The pole is at infinity for the horizontal translation case, point C, and "almost" infinity at point D.)

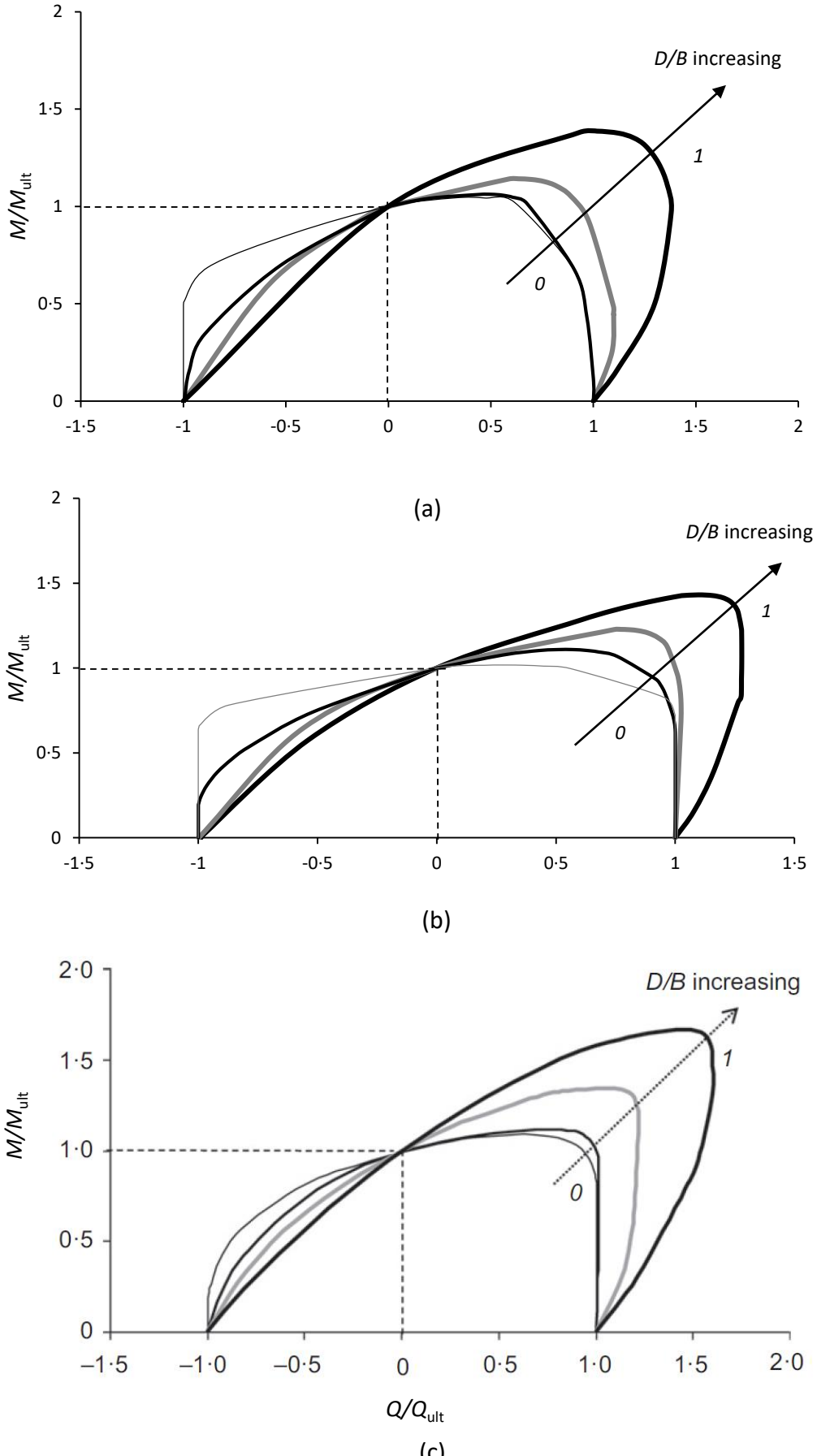

Fig. 15. Normalised *MQ* interaction envelopes for four embedment ratios *D*/*B*=0, 0·2, 0·5, 1. FBC, *N*=0: (a) inhomogeneous soil with *m*=2 kPa/m, (b) inhomogeneous soil with *m*=10 kPa/m, and (c) homogeneous soil (Ntritsos *et al.*, 2015).

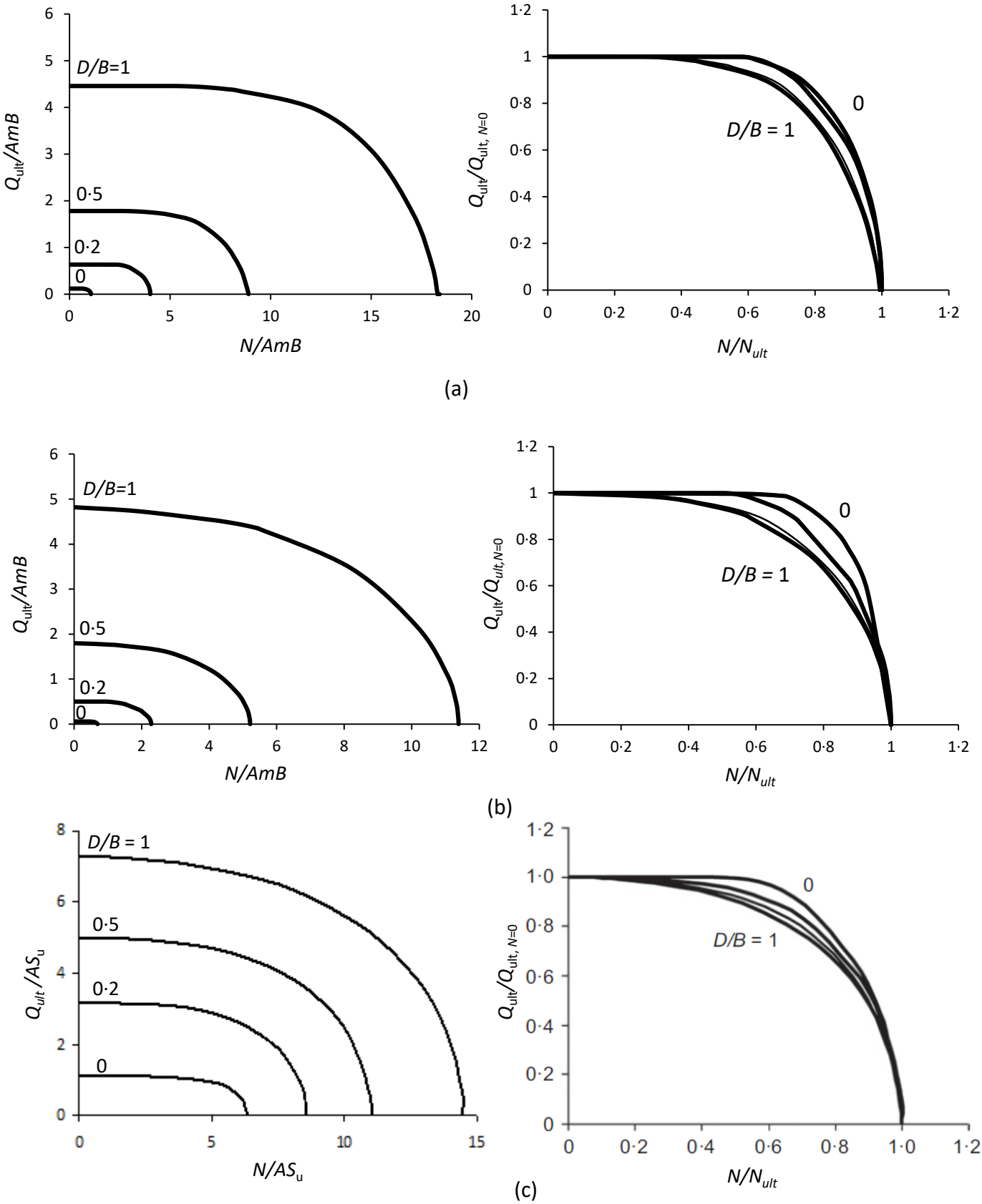

Fig. 16. Three-dimensional embedded-square foundation with FBC normalized with AS_u (S_u for depth equal to B) and with the ultimate values of N and Q: (a) inhomogeneous soil with m=2 kPa/m, (b) inhomogeneous soil with m=10 kPa/m, and (c) homogeneous soil (Ntritsos *et al.*, 2015).

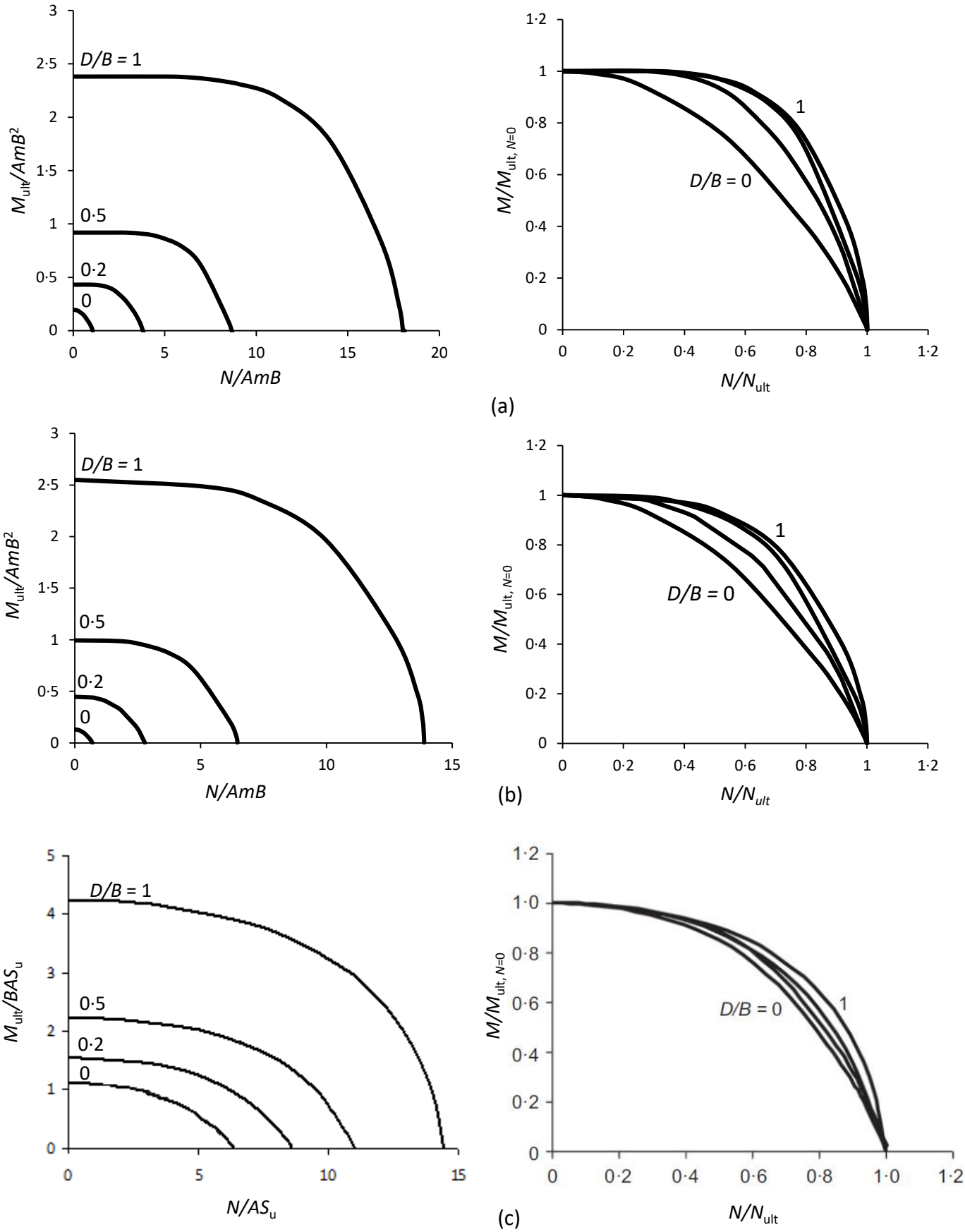

Fig. 17. Three-dimensional embedded-square foundation with FBC *MN* envelopes normalised with ABS_u (S_u for depth equal to *B*) and with the ultimate values of *N* and *M*: (a) inhomogeneous soil with *m*=2 kPa/m, (b) inhomogeneous soil with *m*=10 kPa/m, and (c) homogeneous soil (Ntritsos *et al.*, 2015).

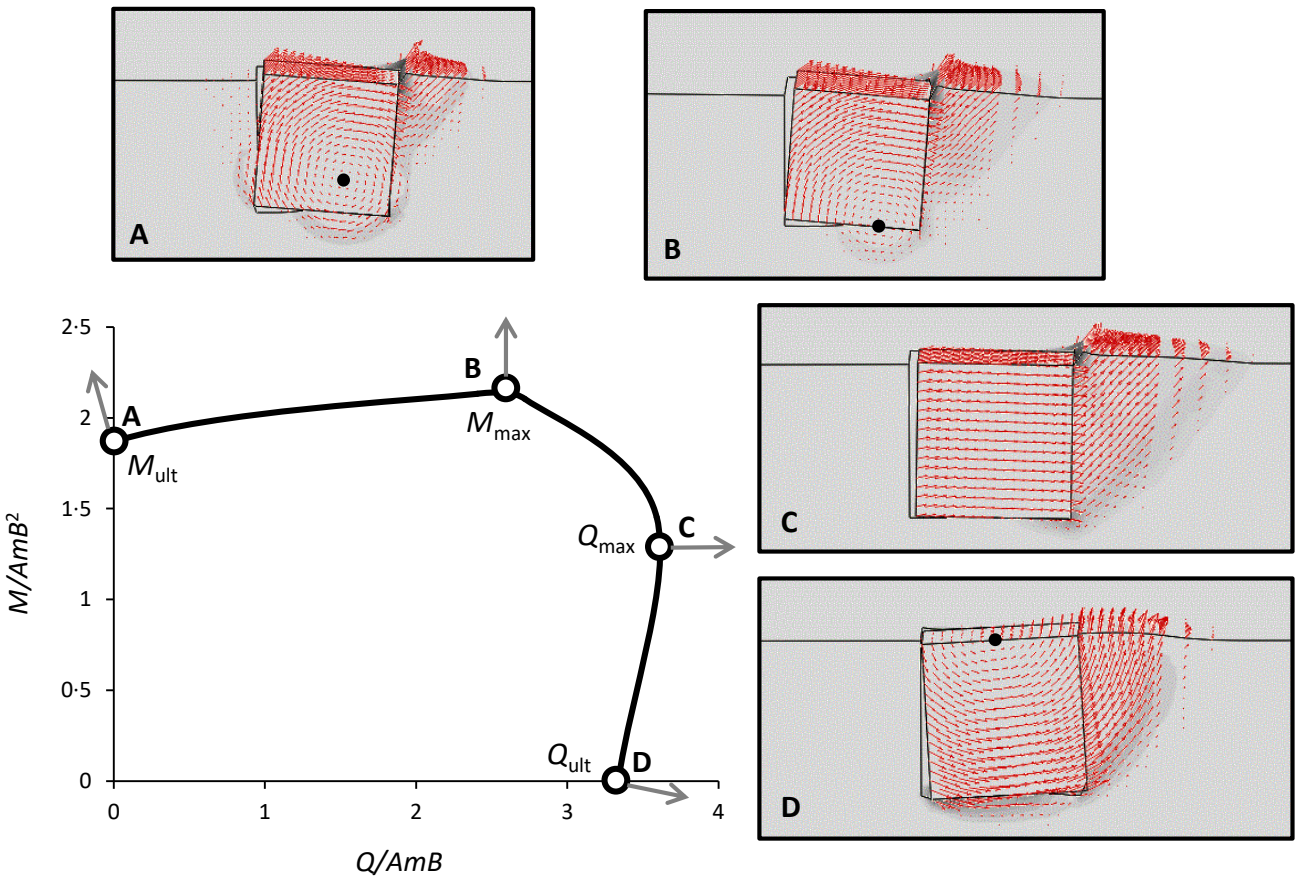

Fig. 18. *MQ* interaction (for N/N_{ult}=0·25) in inhomogeneous soil with *m*=10 kPa/m: failure mechanisms at key points of the failure envelope of a *D*/*B*=1 foundation having a tensionless sliding interface (TSI) with the soil. The solid dots represent approximately the instantaneous rotation pole, which for purely horizontal translation (point C) is at infinity

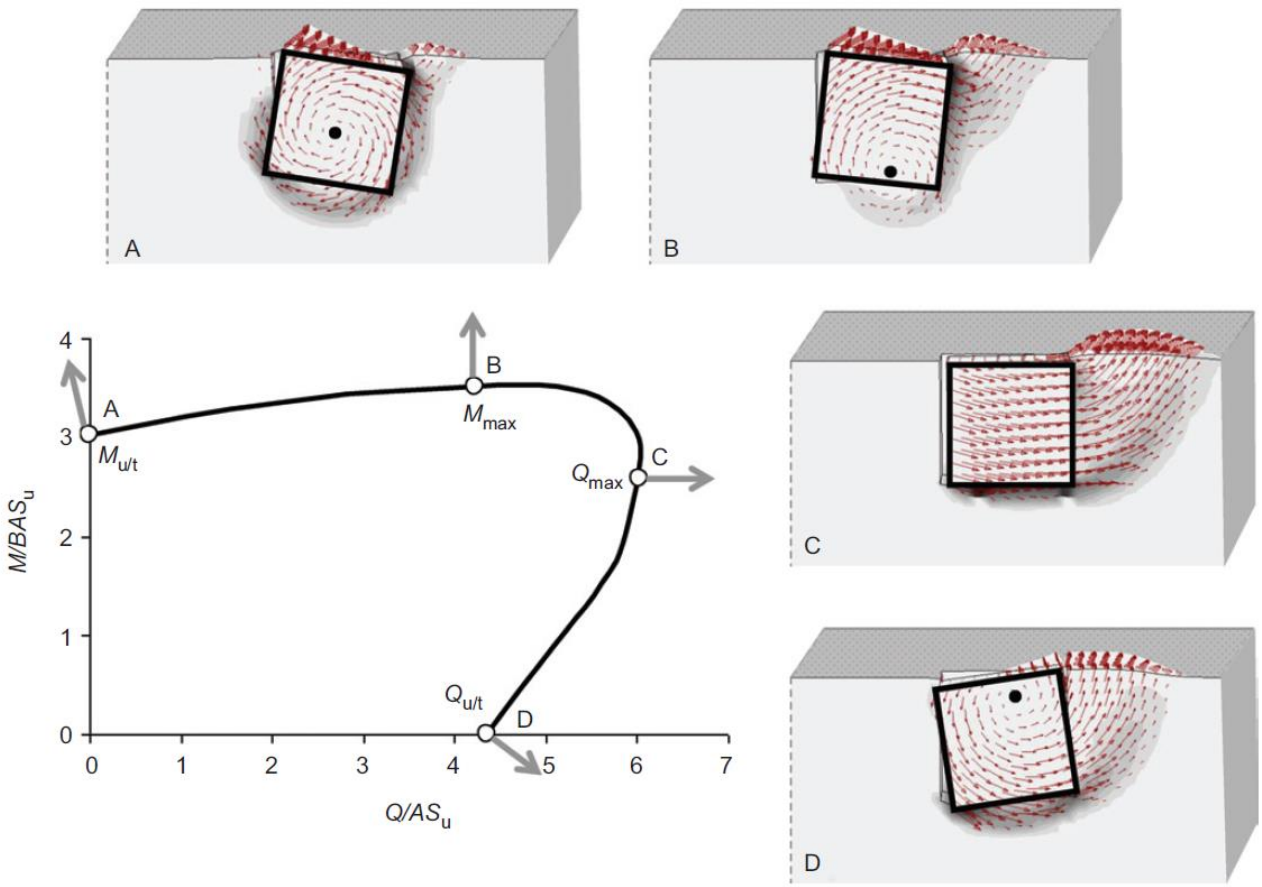

Fig. 19. *MQ* interaction (for N/N_{ult}=0): failure mechanisms at key points of the failure envelope of a D/B=1 foundation having a tensionless sliding interface (TSI) with the soil. The solid dots represent approximately the instantaneous rotation pole, which for purely horizontal translation (point C) is at infinity

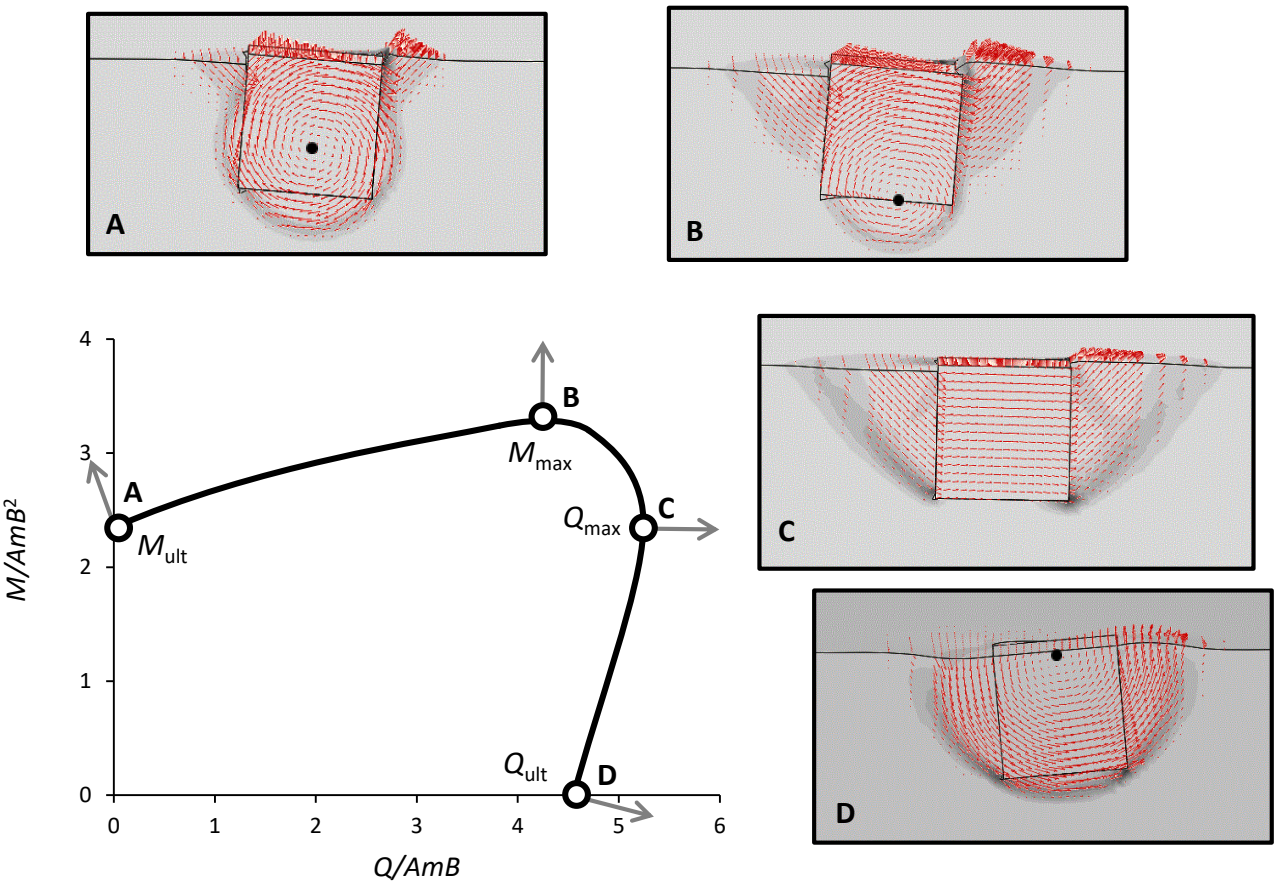

Fig. 20. *MQ* interaction (for N/N_{ult}=0·25) in inhomogeneous soil with *m*=2 kPa/m: failure mechanisms at key points of the failure envelope of a *D*/*B*=1 foundation having a tensionless sliding interface (TSI) with the soil. The solid dots represent approximately the instantaneous rotation pole, which for purely horizontal translation (point C) is at infinity

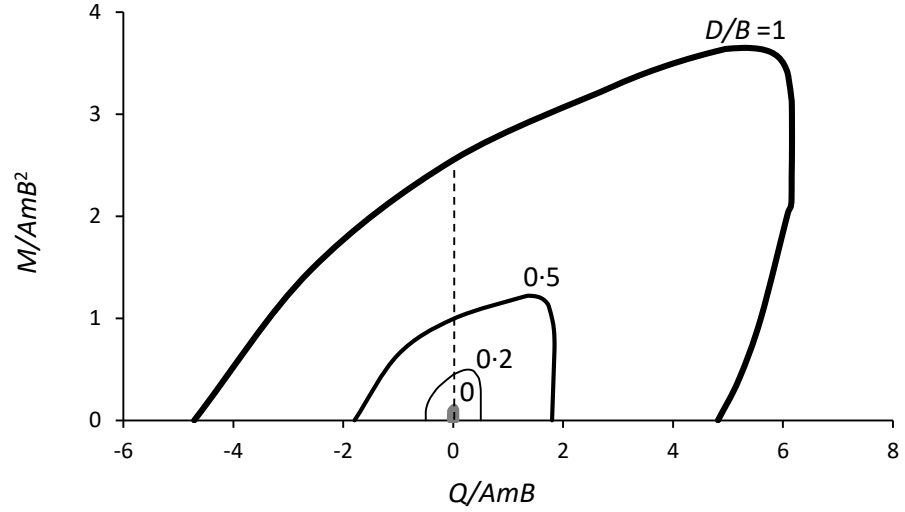

(a)

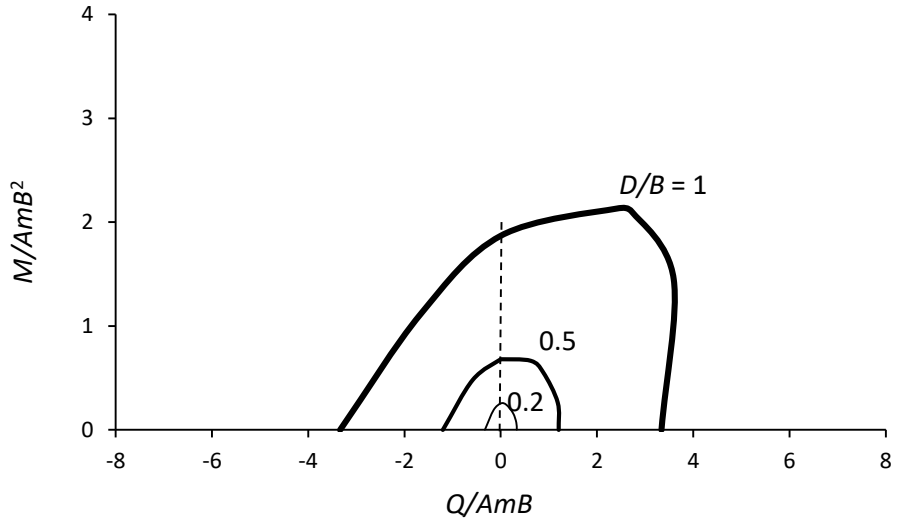

(b)

Fig. 21. Effect of interface conditions in inhomogeneous soil with *m*=10 kPa/m: failure envelopes in *MQ* load plane: (a) FBC for N/N_{ult}=0, compared to (b) TSI for N/N_{ult}=0·25

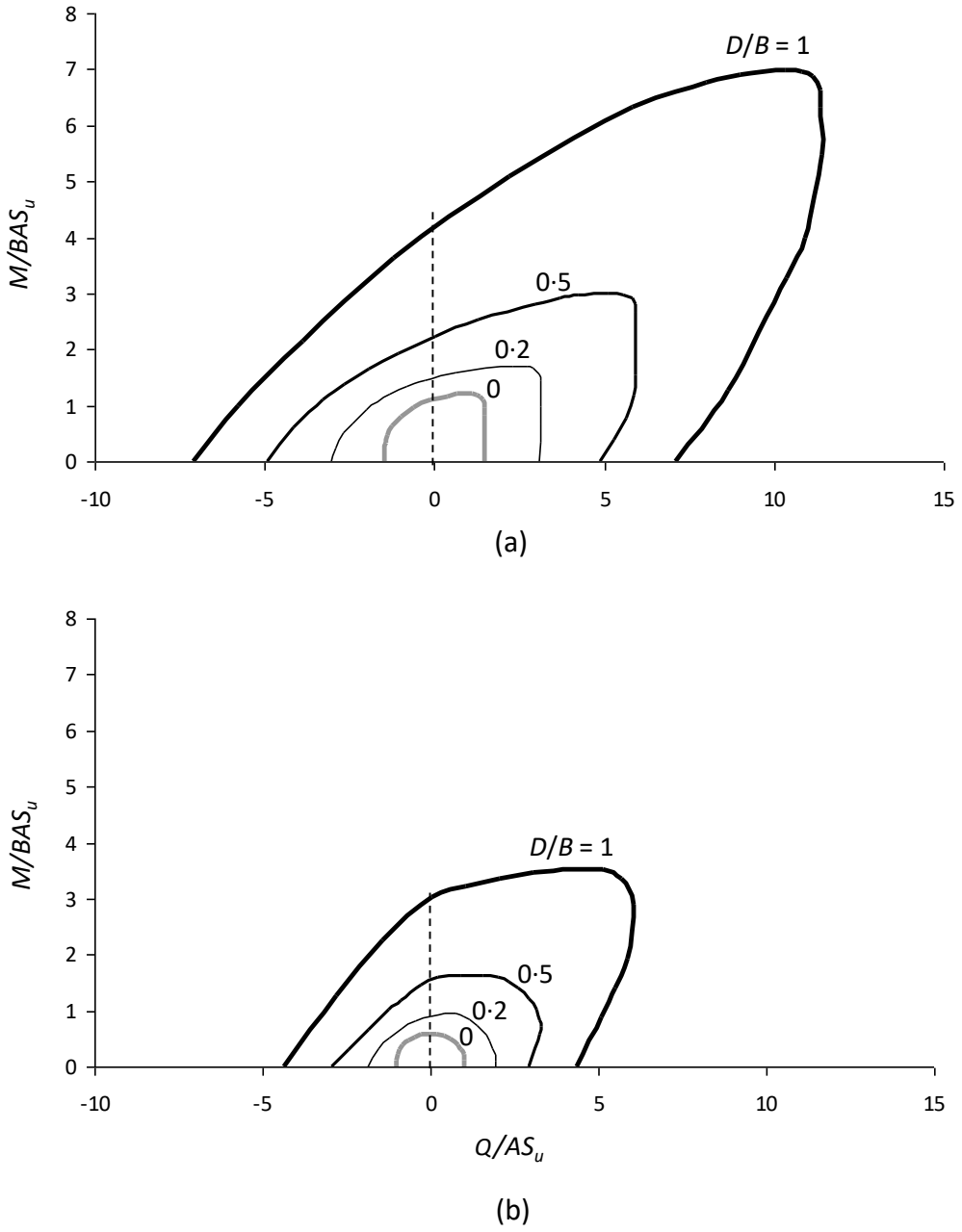

Fig. 22. Effect of interface conditions in homogeneous soil (Ntritsos *et al.*, 2015): failure envelopes in *MQ* load plane for N/N_{ult}=0·25: (a) FBC, compared to (b) tensionless sliding interface (TSI)

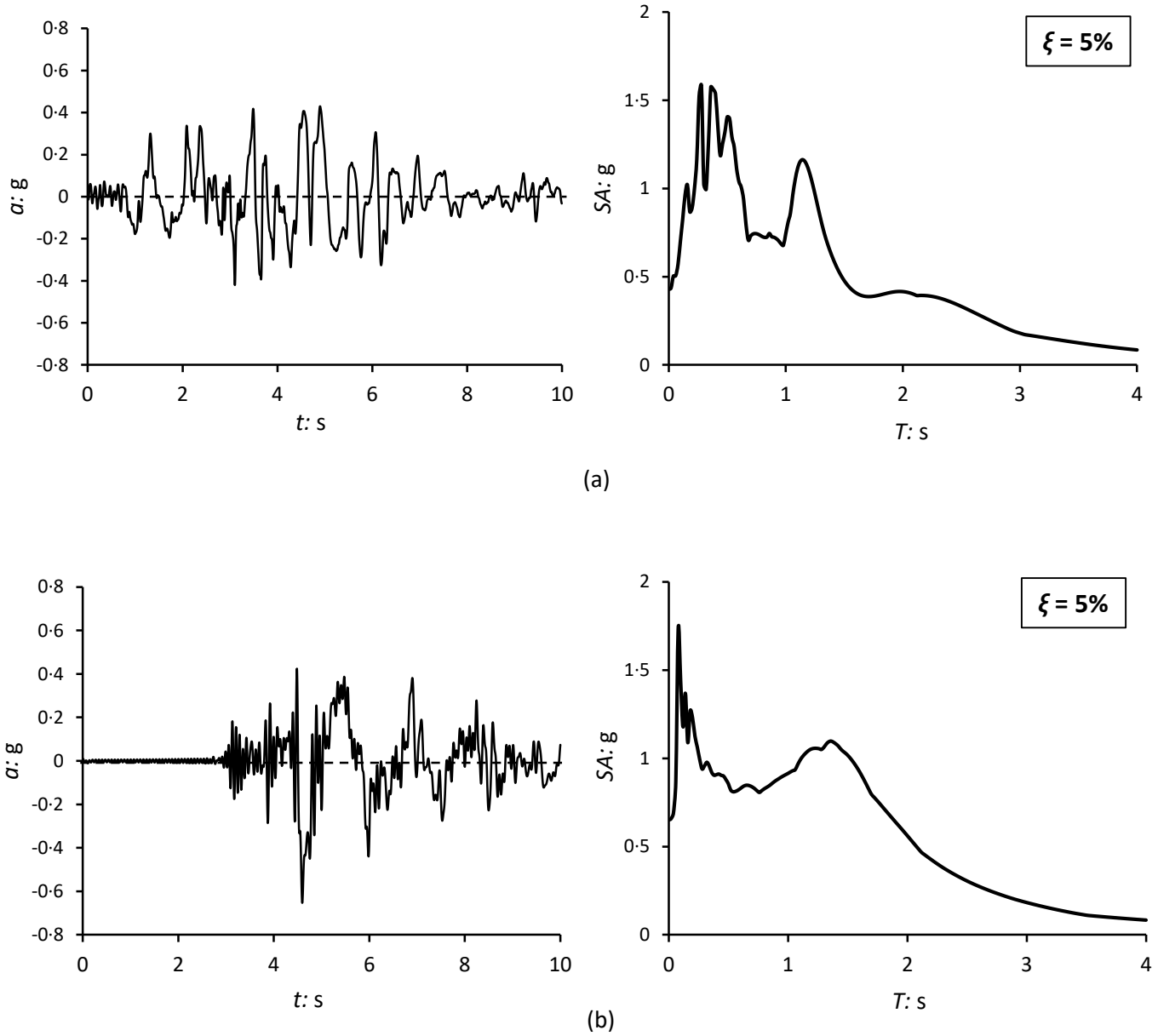

Fig. 23. Accelerograms and spectrums of seismic records: (a) *Shin-Kobe* (Kobe, Japan, 1995), (b) *LXR* (Lixouri, Kefalonia, Greece, 2014).

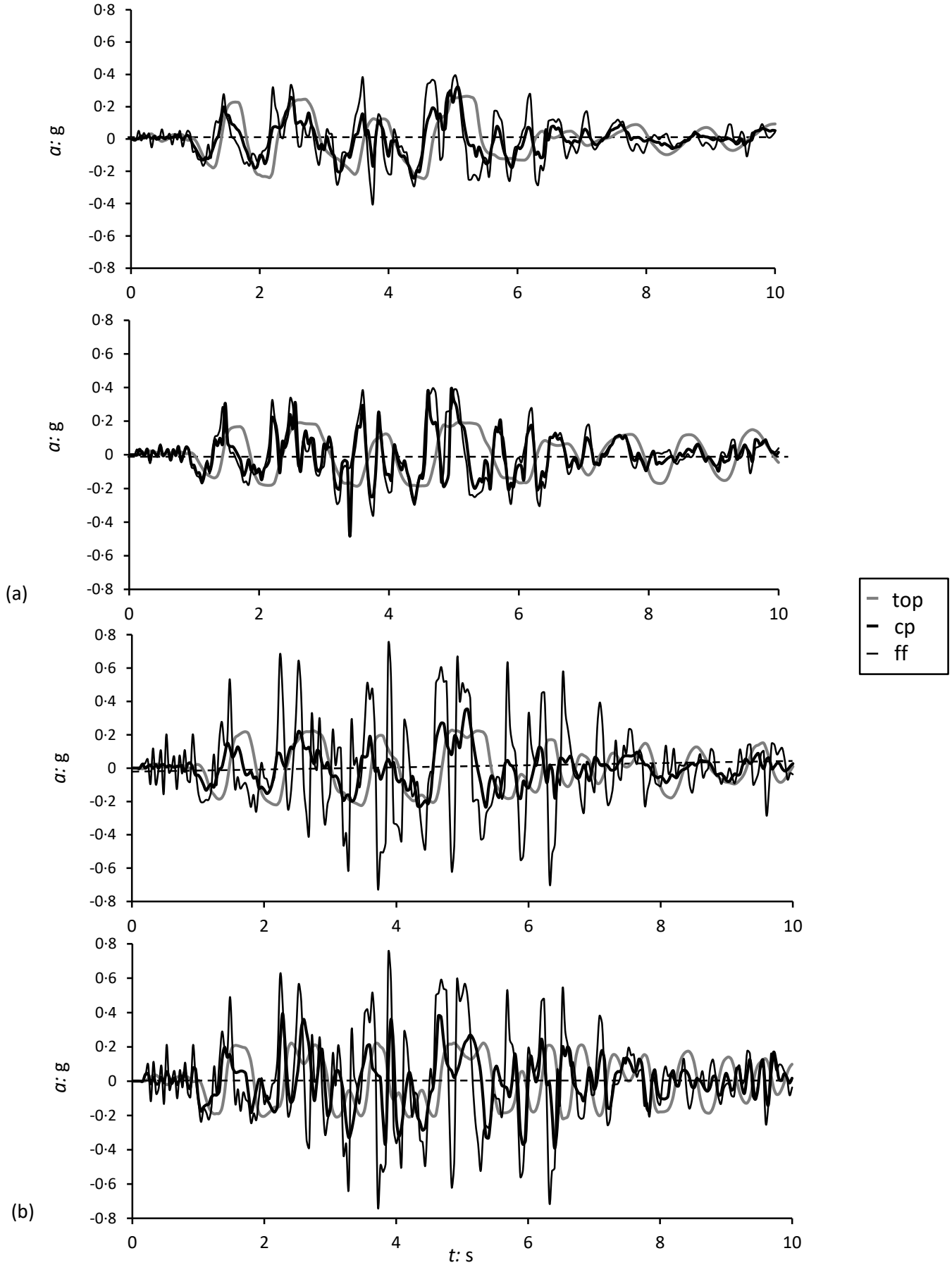

Fig. 24. Accelerograms for seismic record *Shin-Kobe* (Kobe, Japan, 1995) and for two soil profiles: (a) homogeneous soil profile and, (b) inhomogeneous soil with *m*=10 kPa/m. Up: *D/B*=1; down *D/B*=0·2. The results refer to three points: top of superstructure (top), top of foundation or control point (cp) and a specific free field point (ff). FS_V=2 and *h*=10 m.

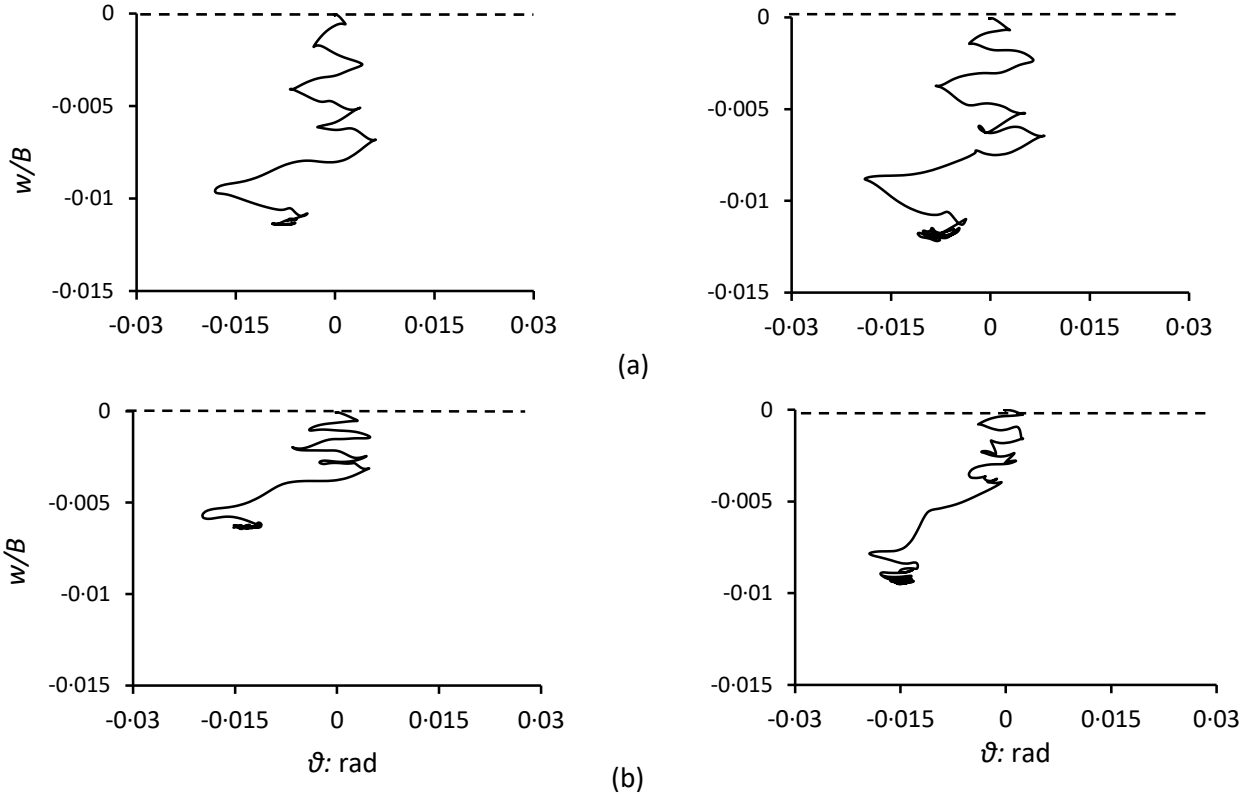

Fig. 25. Foundation settlement-rotation response for seismic record *Shin-Kobe* (Kobe, Japan, 1995) and for two soil profiles: (a) homogeneous soil profile and, (b) inhomogeneous soil with *m*=10 kPa/m. Left: *D/B*=1; right *D/B*=0·2. The results refer to the top of foundation or control point (cp). FS_V=2 and *h*=10 m.

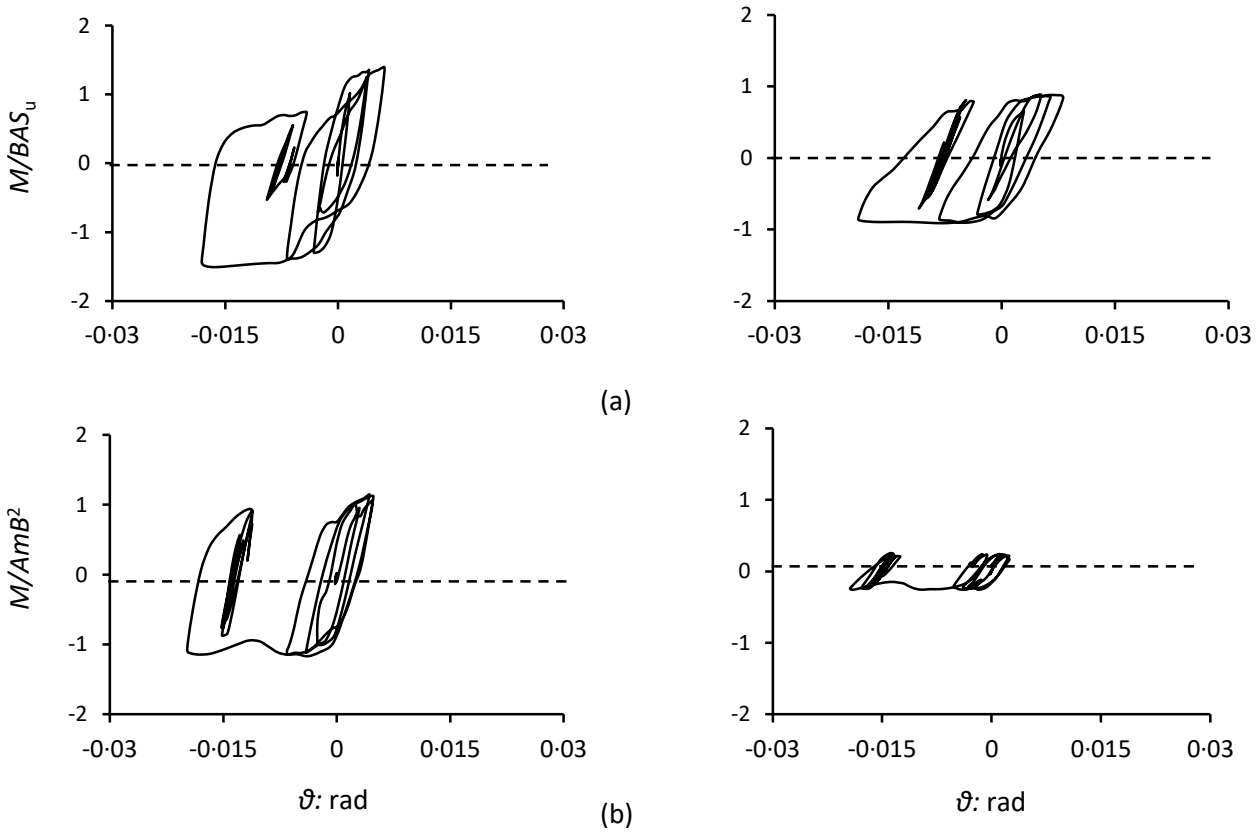

Fig. 26. Foundation dimensionless moment-rotation response for seismic record *Shin-Kobe* (Kobe, Japan, 1995) and for two soil profiles: (a) homogeneous soil profile and, (b) inhomogeneous soil with *m*=10 kPa/m. Left: *D/B*=1; right *D/B*=0·2. FS_V=2 and *h*=10 m.

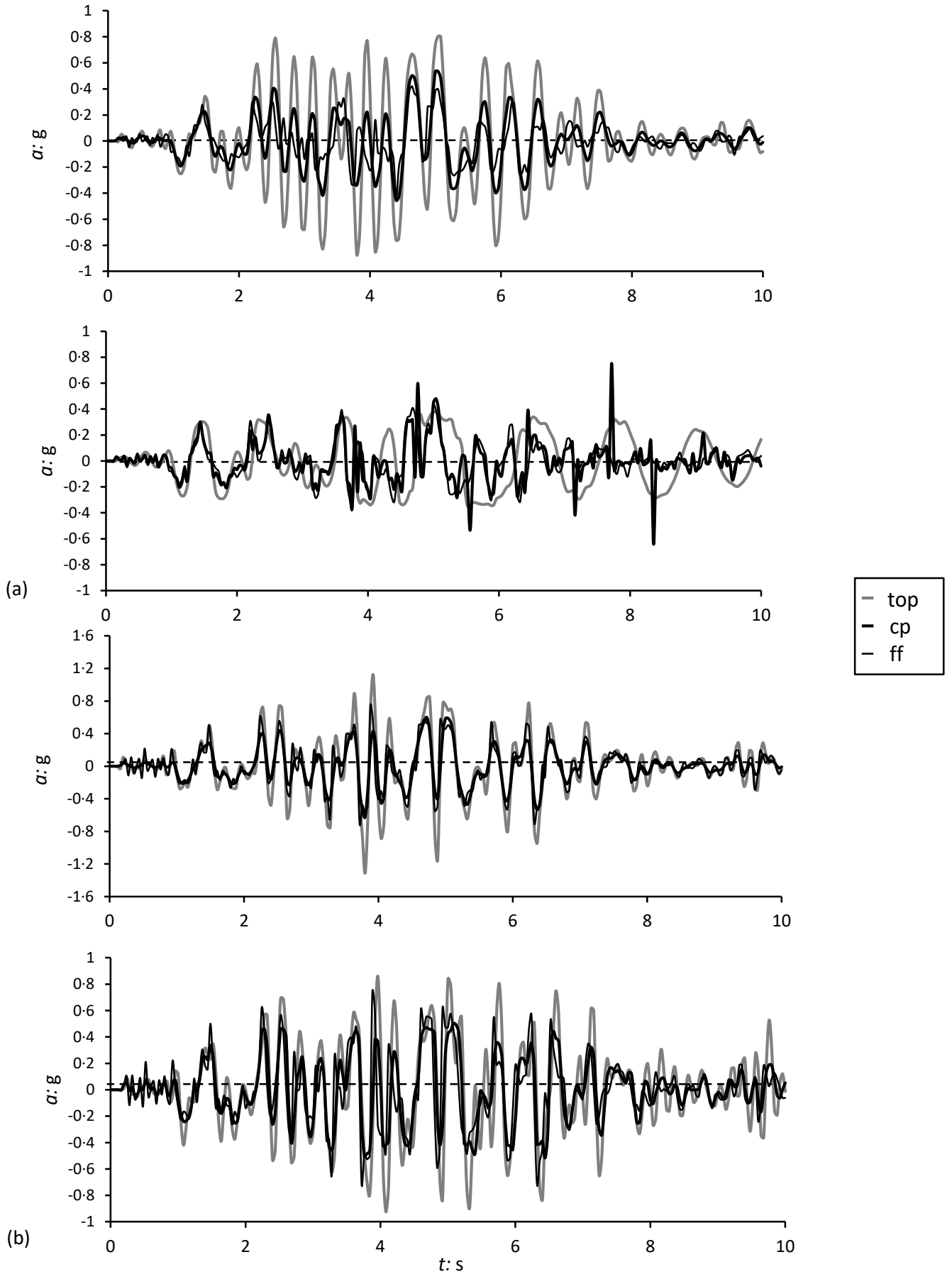

Fig. 27. Accelerograms for seismic record *Shin-Kobe* (Kobe, Japan, 1995) and for two soil profiles: (a) homogeneous soil profile and, (b) inhomogeneous soil with *m*=10 kPa/m. Up: *D/B*=1; down *D/B*=0·2. The results refer to three points: top of superstructure (top), top of foundation or control point (cp) and a specific free field point (ff). FS_V=5 and *h*=10 m.

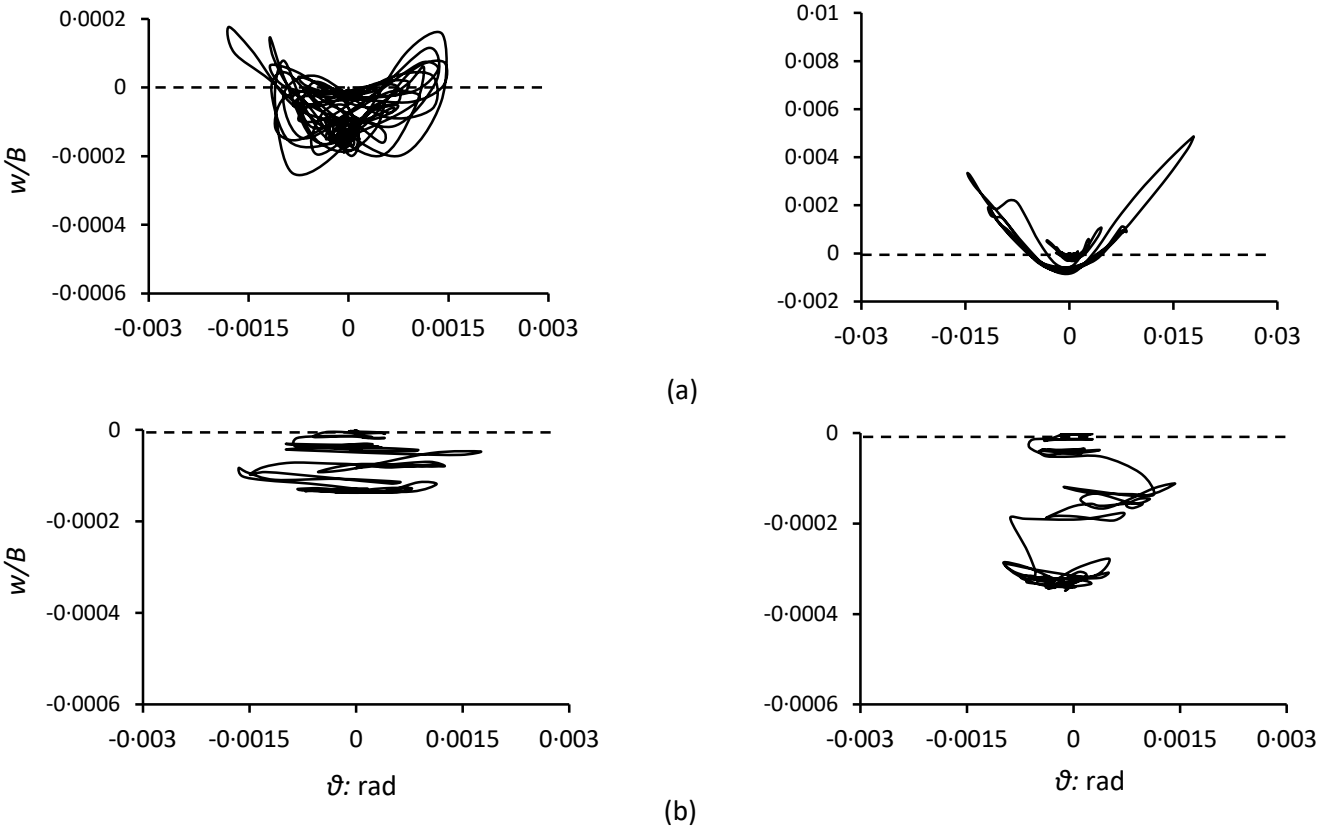

Fig. 28. Foundation settlement-rotation response for seismic record *Shin-Kobe* (Kobe, Japan, 1995) and for two soil profiles: (a) homogeneous soil profile and, (b) inhomogeneous soil with m=10 kPa/m. Left: D/B=1; right D/B=0·2. The results refer to the top of foundation or control point (cp). FS_V=5 and h=10 m.

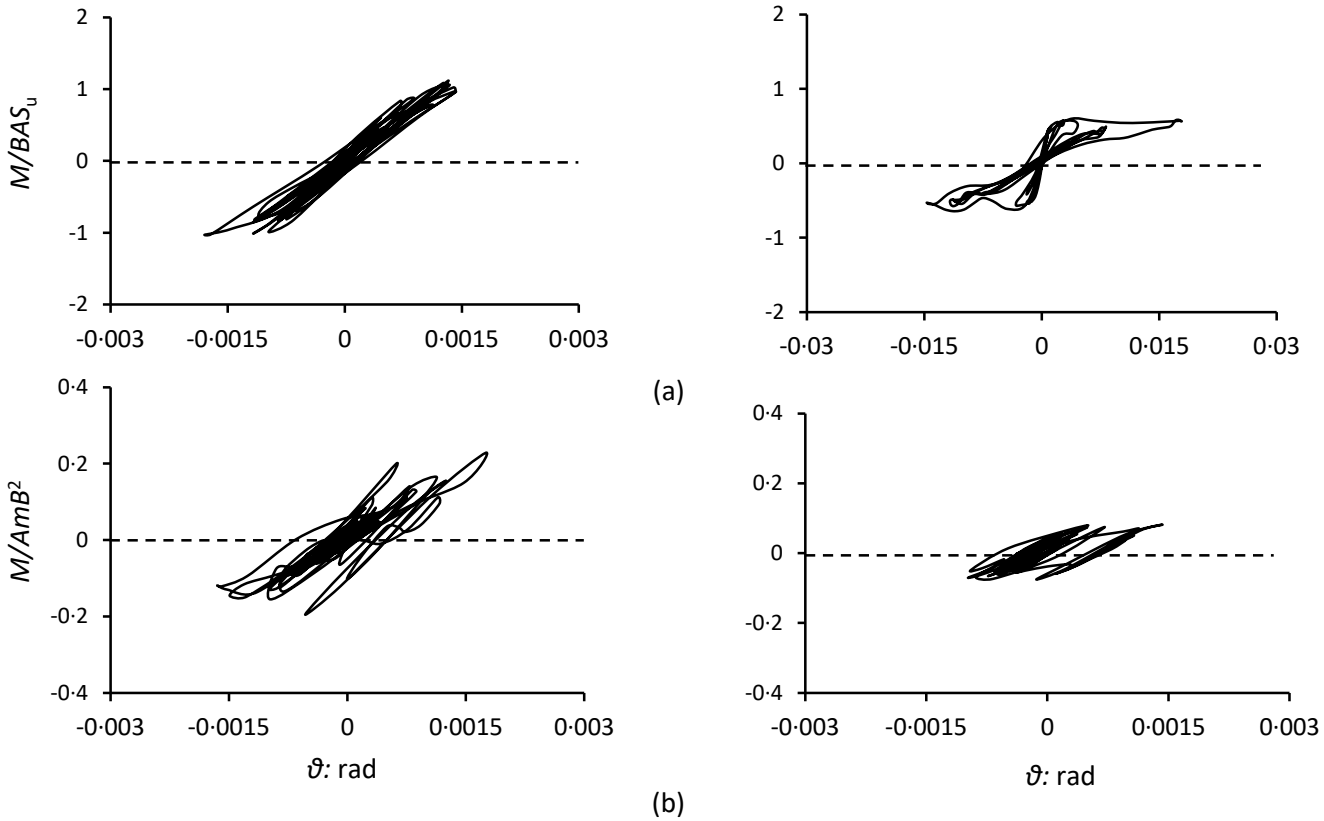

Fig. 29. Foundation dimensionless moment-rotation response for seismic record *Shin-Kobe* (Kobe, Japan, 1995) and for two soil profiles: (a) homogeneous soil profile and, (b) inhomogeneous soil with m=10 kPa/m. Left: D/B=1; right D/B=0·2. FS_V=5 and h=10 m.

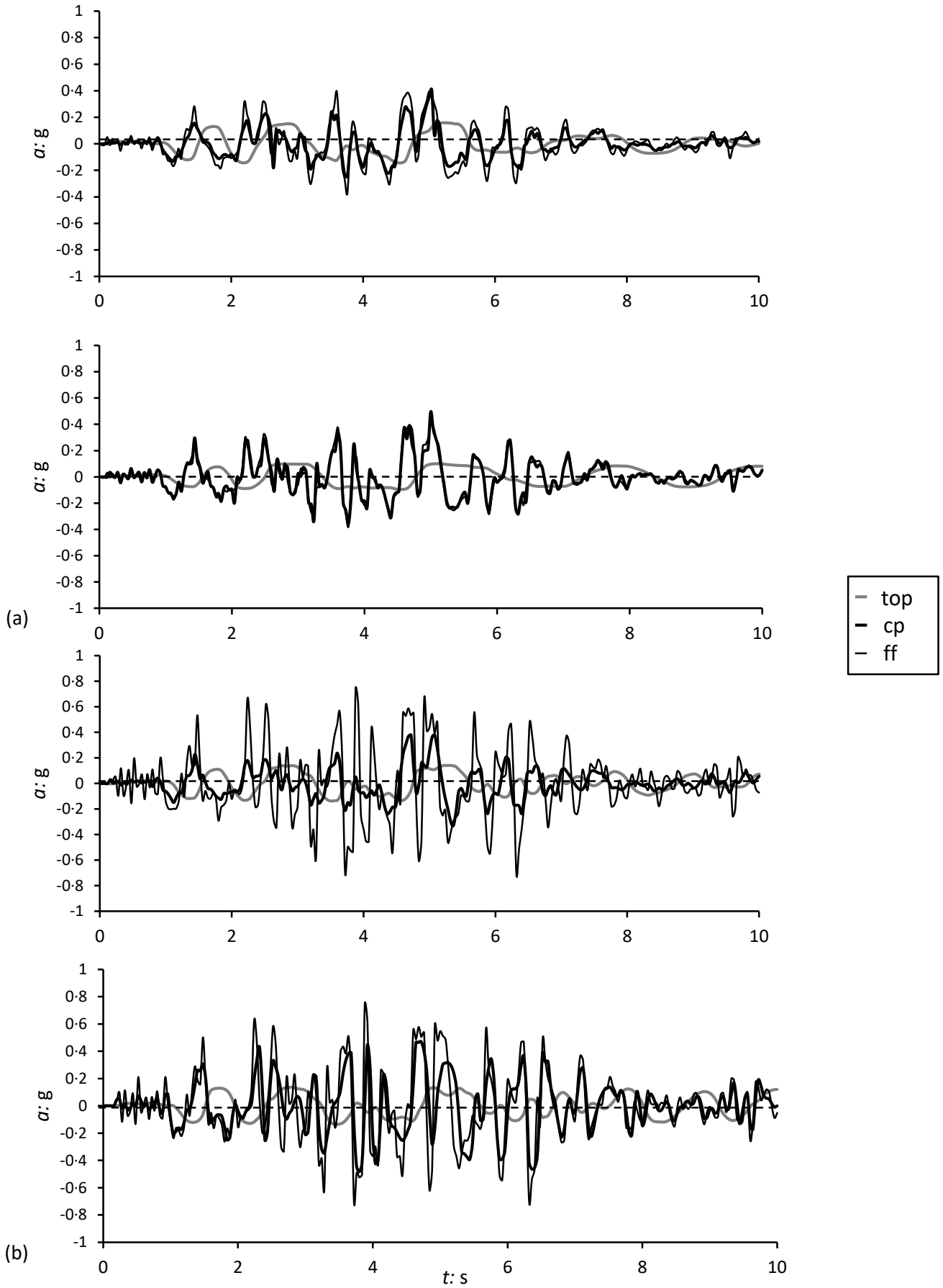

Fig. 30. Accelerograms for seismic record *Shin-Kobe* (Kobe, Japan, 1995) and for two soil profiles: (a) homogeneous soil profile and, (b) inhomogeneous soil with *m*=10 kPa/m. Up: *D/B*=1; down *D/B*=0·2. The results refer to three points: top of superstructure (top), top of foundation or control point (cp) and a specific free field point (ff). FS_V=2 and *h*=20 m.

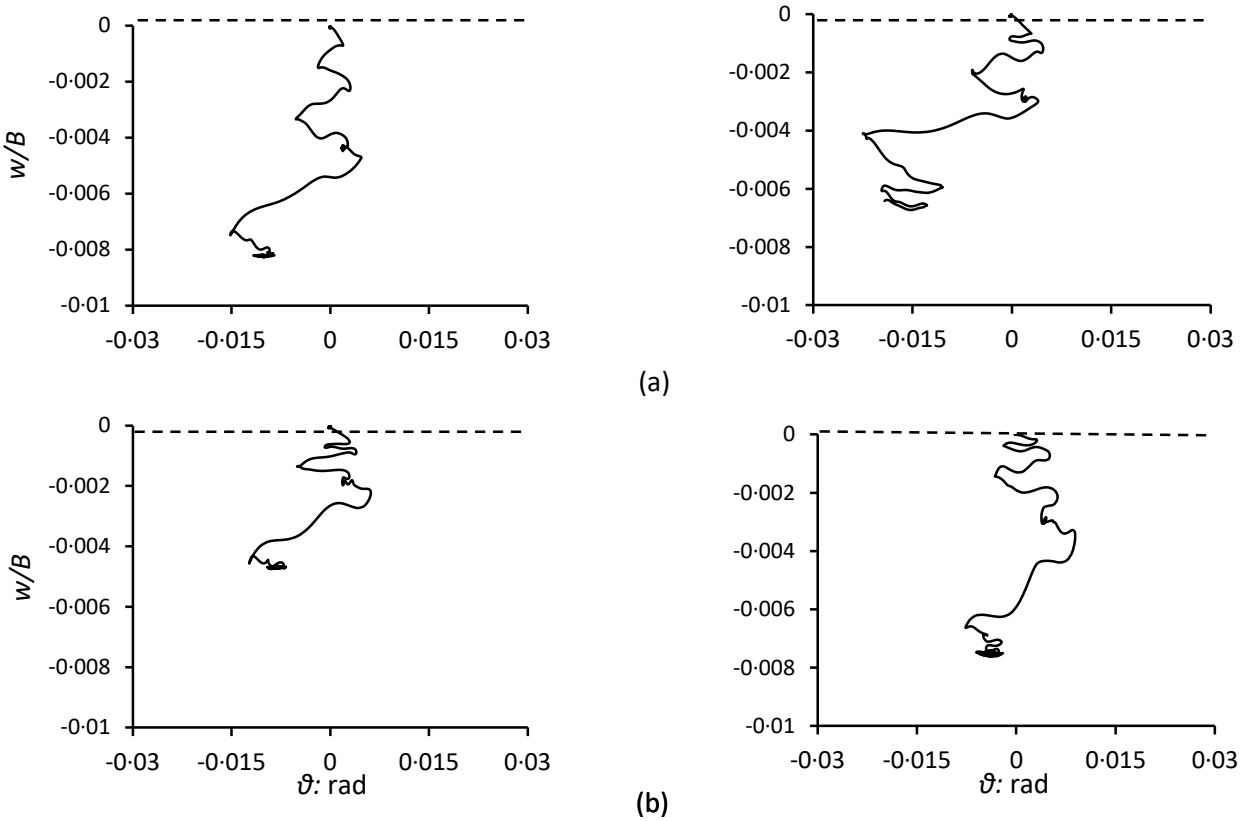

Fig. 31. Foundation settlement-rotation response for seismic record *Shin-Kobe* (Kobe, Japan, 1995) and for two soil profiles: (a) homogeneous soil profile and, (b) inhomogeneous soil with *m*=10 kPa/m. Left: *D/B*=1; right *D/B*=0·2. The results refer to the top of foundation or control point (cp). FS_V=2 and *h*=20 m.

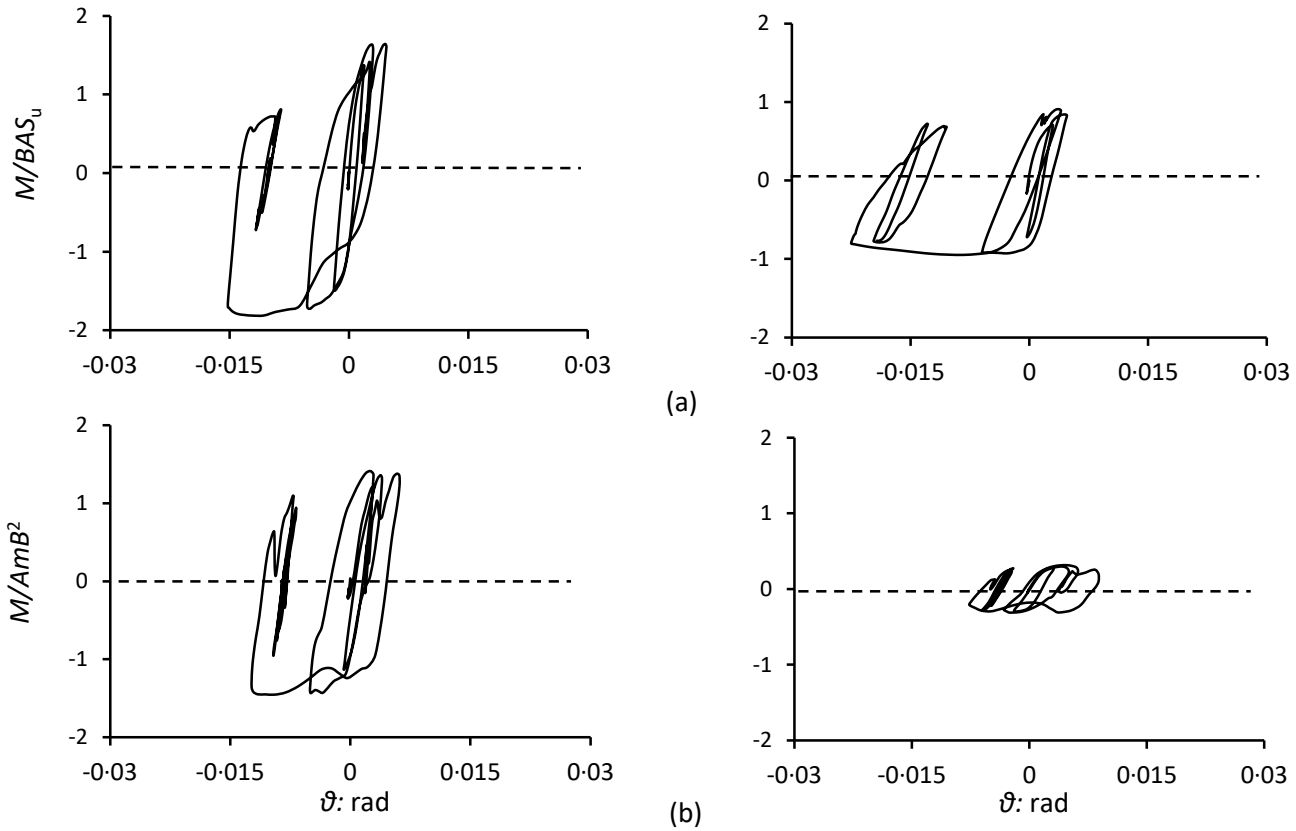

Fig. 32. Foundation dimensionless moment-rotation response for seismic record *Shin-Kobe* (Kobe, Japan, 1995) and for two soil profiles: (a) homogeneous soil profile and, (b) inhomogeneous soil with *m*=10 kPa/m. Left: *D/B*=1; right *D/B*=0·2. FS_V=2 and *h*=20 m.

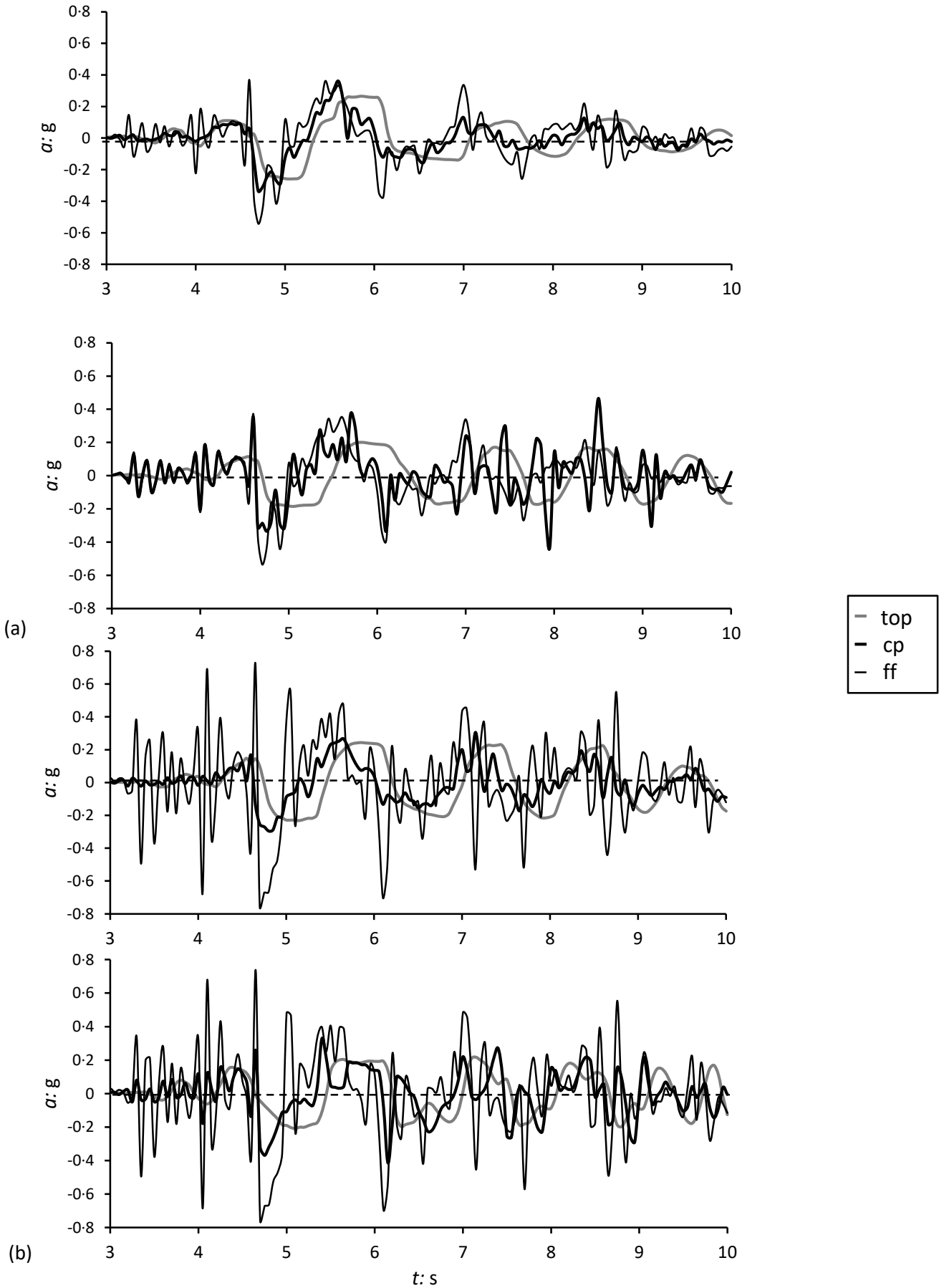

Fig. 33. Accelerograms for seismic record *LXR* (Lixouri, Kefalonia, Greece, 2014) and for two soil profiles: (a) homogeneous soil profile and, (b) inhomogeneous soil with *m*=10 kPa/m. Up: *D/B*=1; down *D/B*=0·2. The results refer to three points: top of superstructure (top), top of foundation or control point (cp) and a specific free field point (ff). FS_V=2 and *h*=10 m.

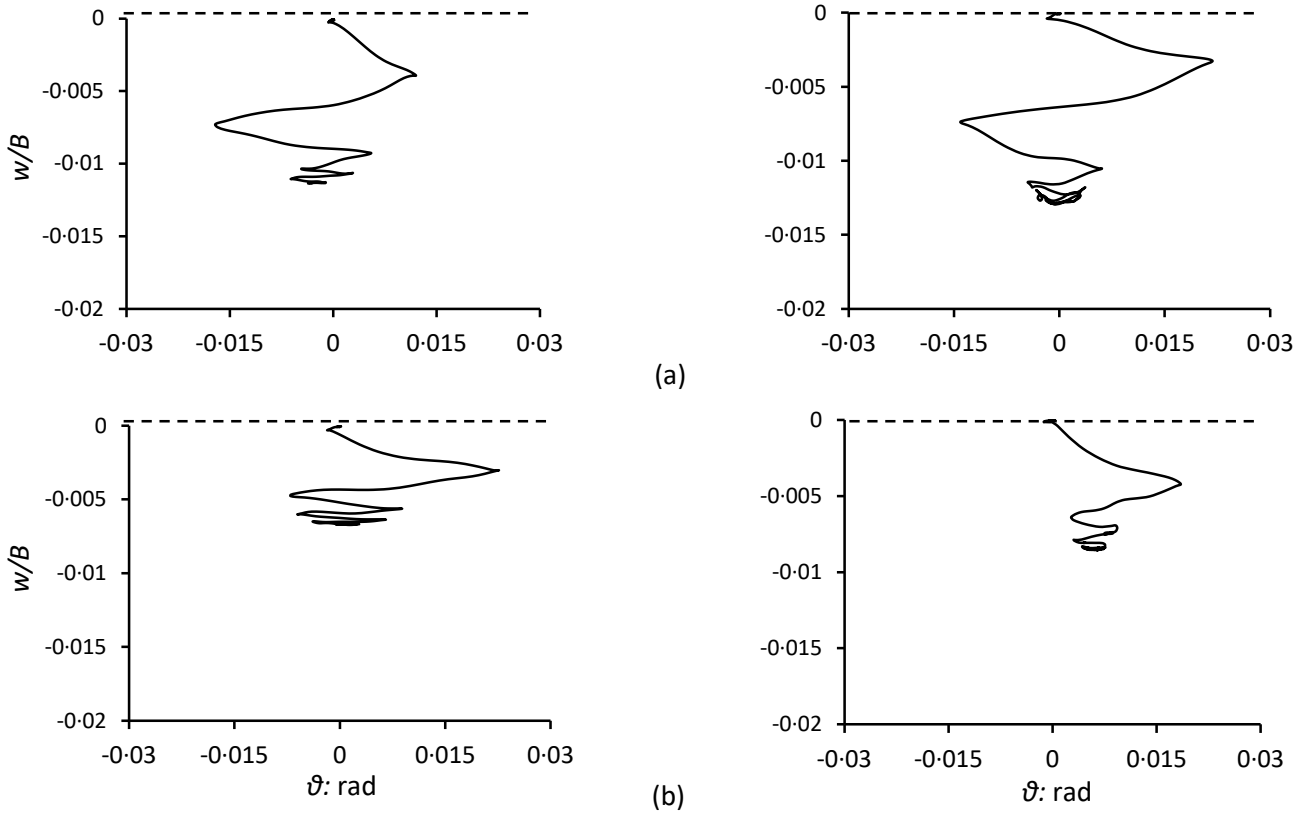

Fig. 34. Foundation settlement-rotation response for seismic record *LXR* (Lixouri, Kefalonia, Greece, 2014) and for two soil profiles: (a) homogeneous soil profile and, (b) inhomogeneous soil with *m*=10 kPa/m. Left: *D/B*=1; right *D/B*=0·2. The results refer to the top of foundation or control point (cp). FS_V=2 and *h*=10 m.

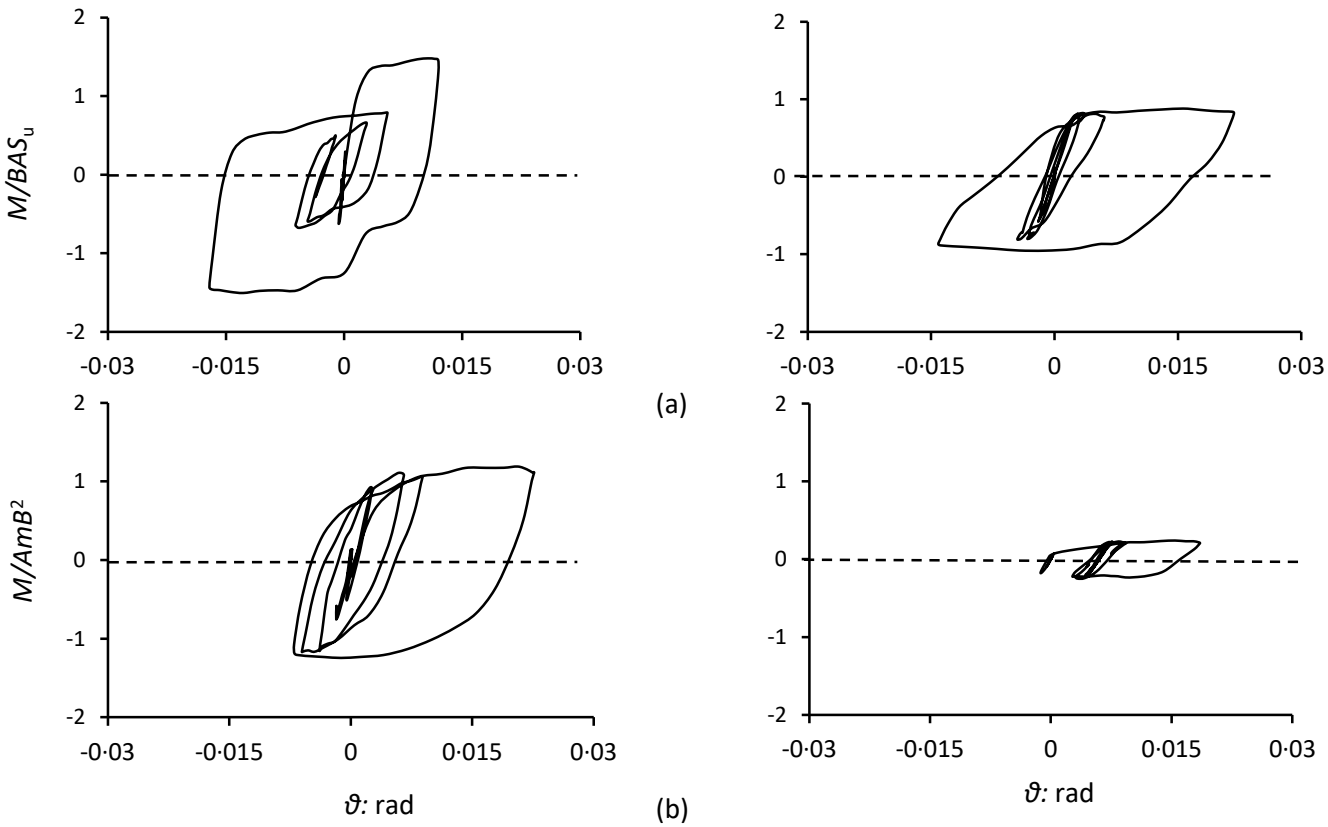

Fig. 35. Foundation dimensionless moment-rotation response for seismic record *LXR* (Lixouri, Kefalonia, Greece, 2014) and for two soil profiles: (a) homogeneous soil profile and, (b) inhomogeneous soil with *m*=10 kPa/m. Left: *D/B*=1; right *D/B*=0·2. FS_V=2 and *h*=10 m.

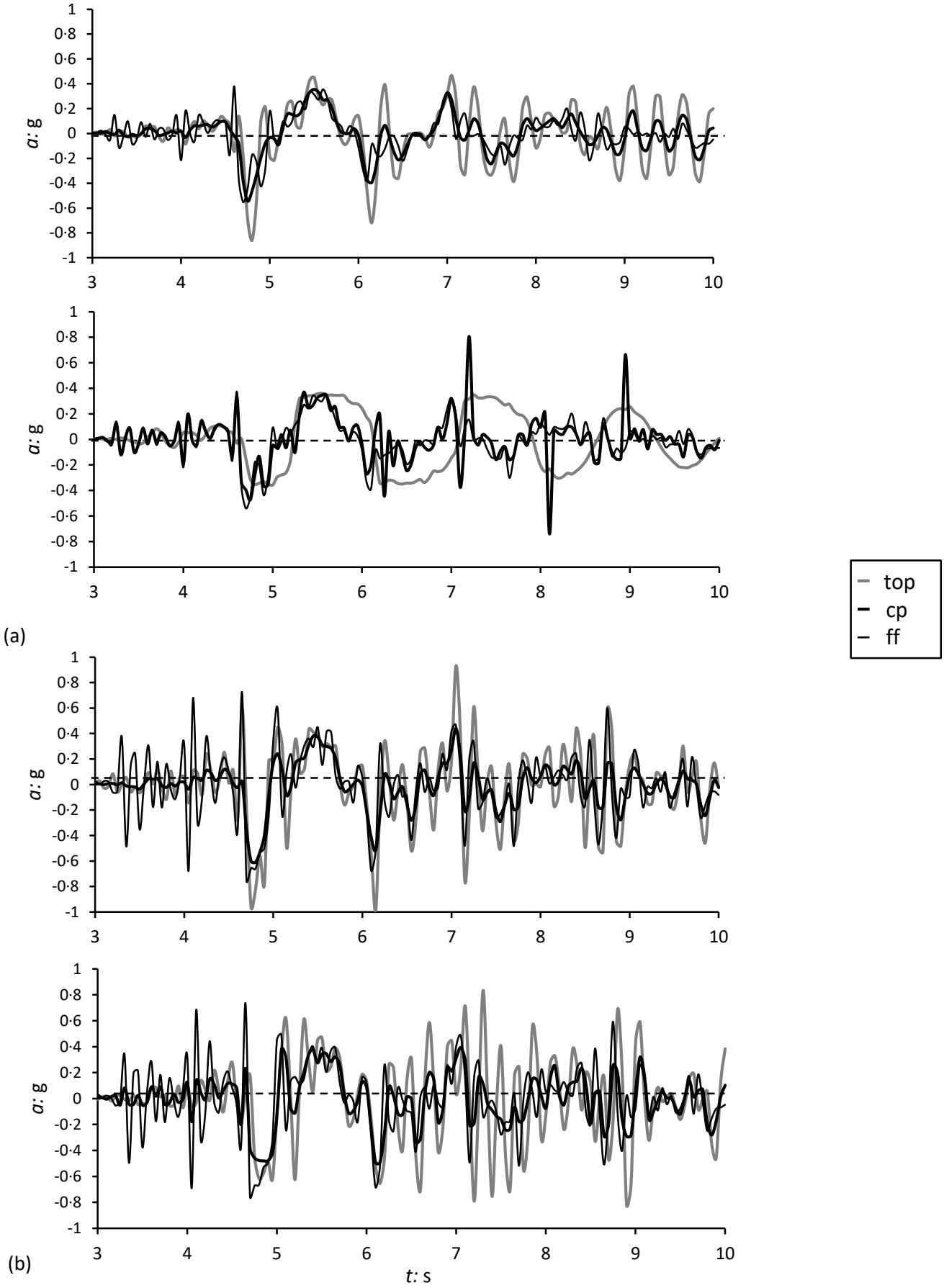

Fig. 36. Accelerograms for seismic record *LXR* (Lixouri, Kefalonia, Greece, 2014) and for two soil profiles: (a) homogeneous soil profile and, (b) inhomogeneous soil with *m*=10 kPa/m. Up: *D/B*=1; down *D/B*=0·2. The results refer to three points: top of superstructure (top), top of foundation or control point (cp) and a specific free field point (ff). FS_V=5 and *h*=10 m.

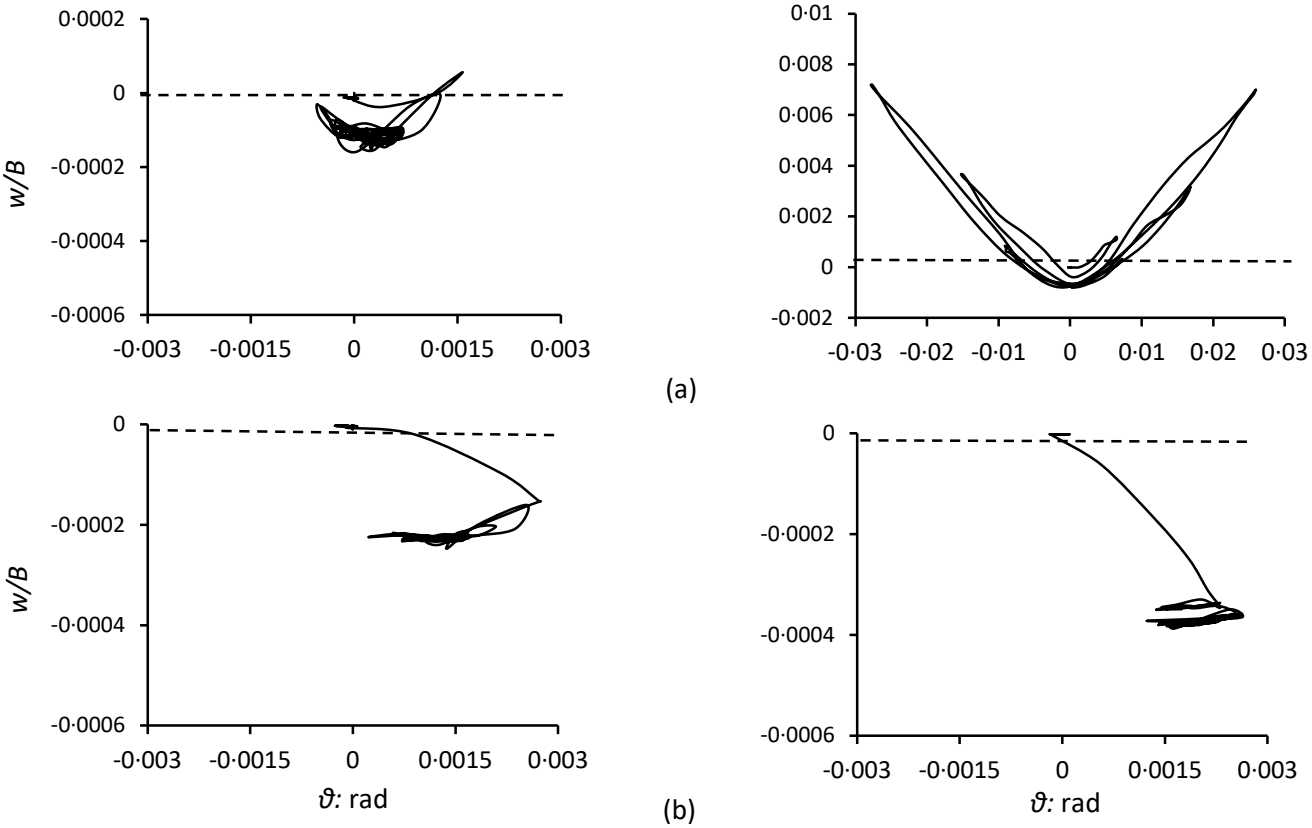

Fig. 37. Foundation settlement-rotation response for seismic record *LXR* (Lixouri, Kefalonia, Greece, 2014) and for two soil profiles: (a) homogeneous soil profile and, (b) inhomogeneous soil with *m*=10 kPa/m. Left: *D/B*=1; right *D/B*=0·2. The results refer to the top of foundation or control point (cp). FS_V=5 and *h*=10 m.

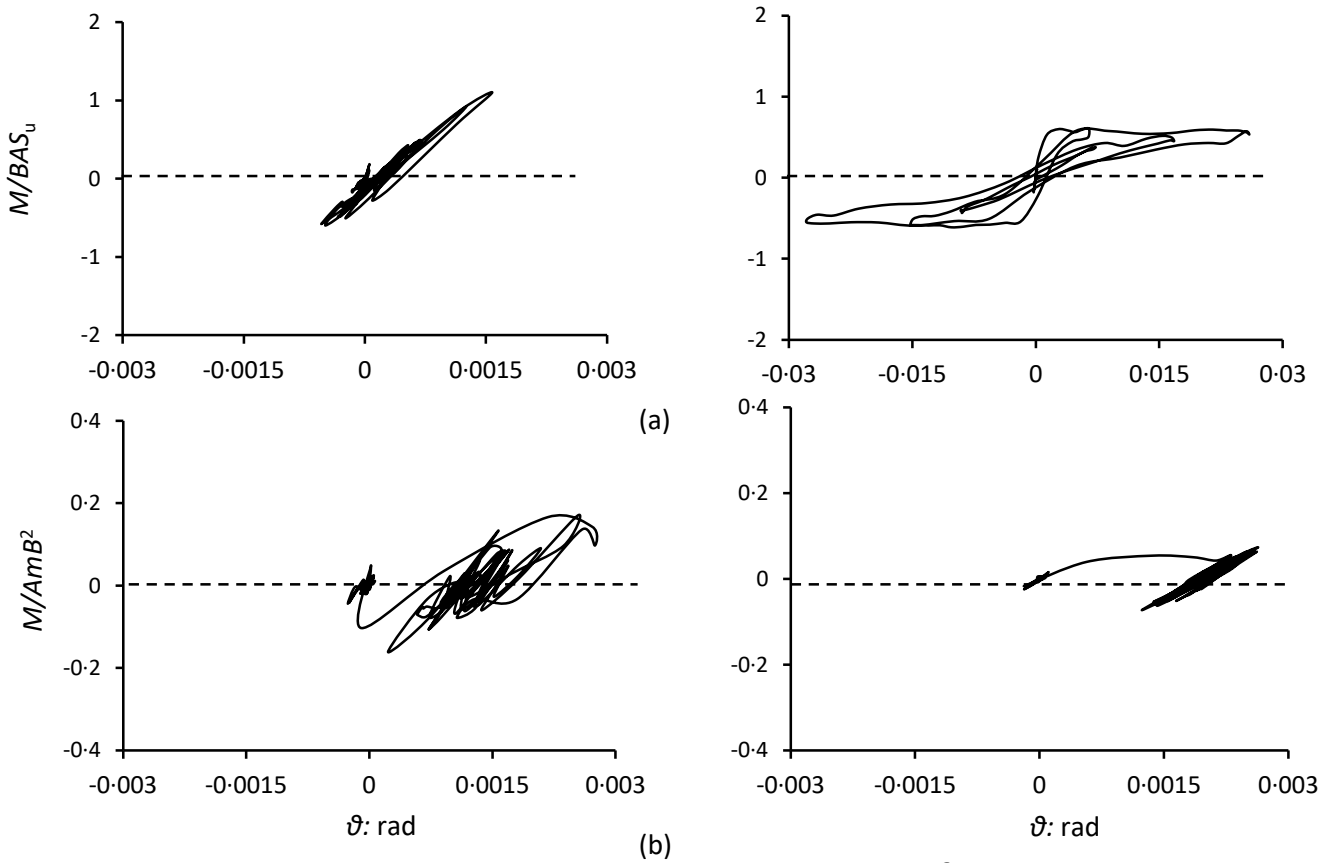

Fig. 38. Foundation dimensionless moment-rotation response for seismic record *LXR* (Lixouri, Kefalonia, Greece, 2014) and for two soil profiles: (a) homogeneous soil profile and, (b) inhomogeneous soil with *m*=10 kPa/m. Left: *D/B*=1; right *D/B*=0·2. FS_V=5 and *h*=10 m.

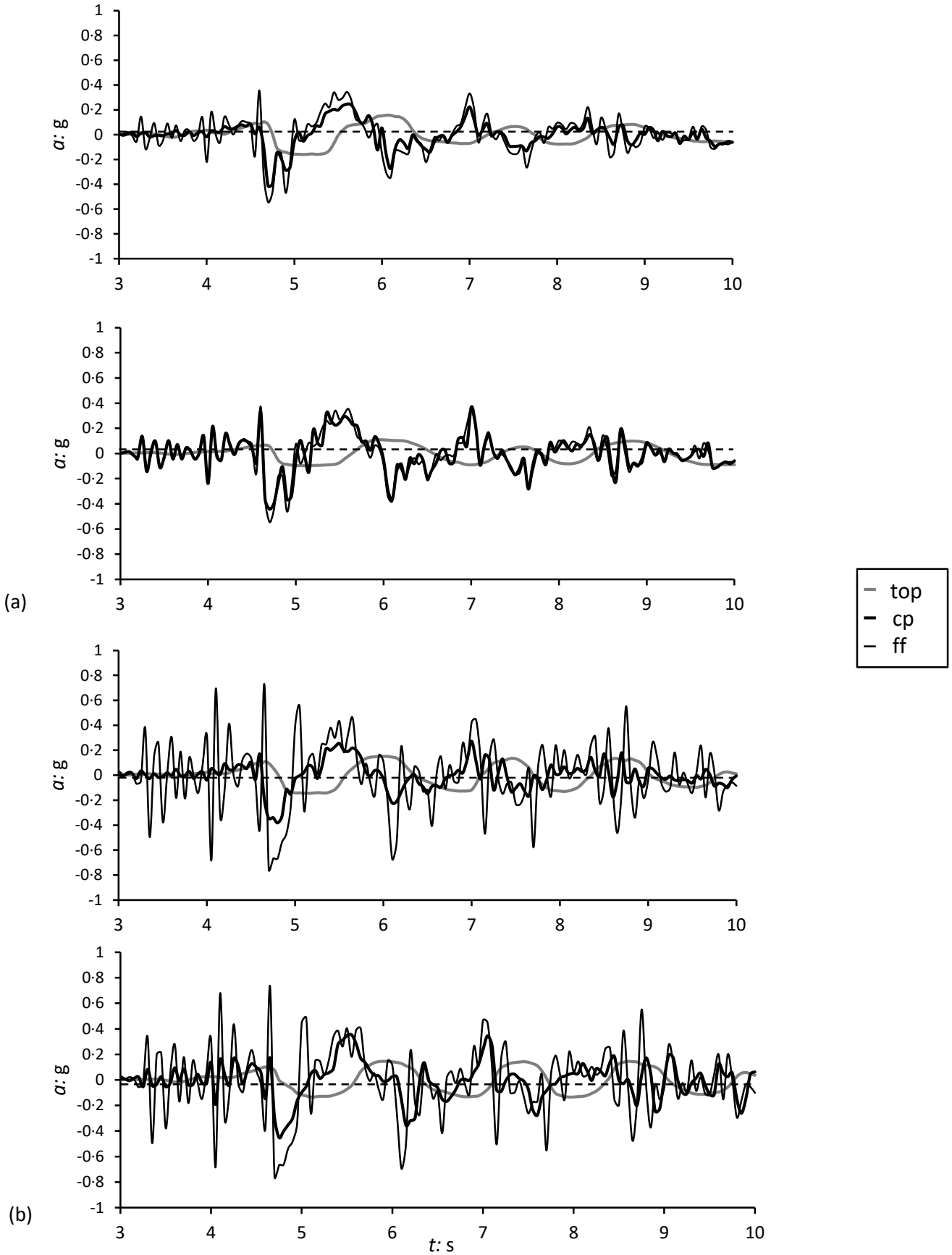

Fig. 39. Accelerograms for seismic record *LXR* (Lixouri, Kefalonia, Greece, 2014) and for two soil profiles: (a) homogeneous soil profile and, (b) inhomogeneous soil with *m*=10 kPa/m. Up: *D/B*=1; down *D/B*=0·2. The results refer to three points: top of superstructure (top), top of foundation or control point (cp) and a specific free field point (ff). FS_V=2 and *h*=20 m.

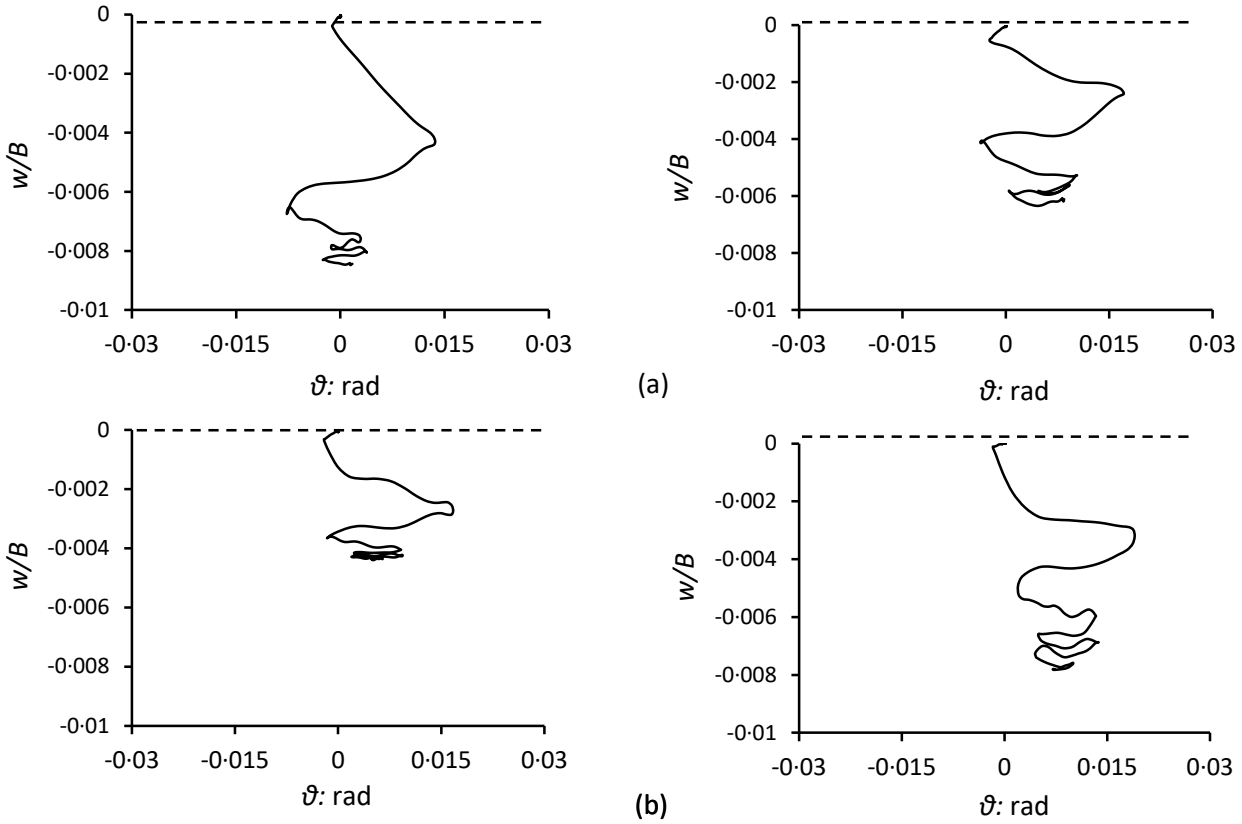

Fig. 40. Foundation settlement-rotation response for seismic record *LXR* (Lixouri, Kefalonia, Greece, 2014) and for two soil profiles: (a) homogeneous soil profile and, (b) inhomogeneous soil with *m*=10 kPa/m. Left: *D/B*=1; right *D/B*=0·2. The results refer to the top of foundation or control point (cp). FS_V=2 and *h*=20 m.

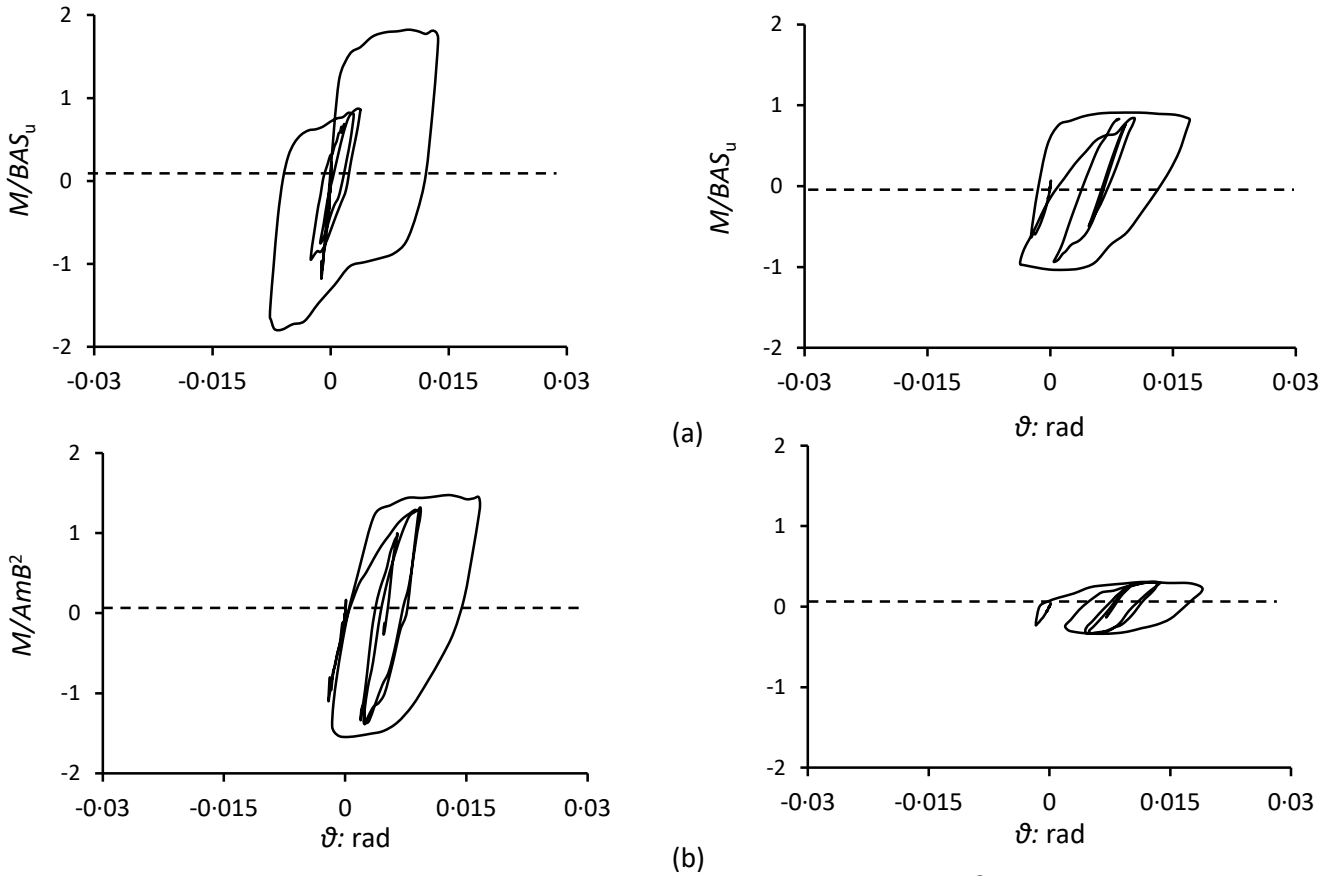

Fig. 41. Foundation dimensionless moment-rotation response for seismic record *LXR* (Lixouri, Kefalonia, Greece, 2014) and for two soil profiles: (a) homogeneous soil profile and, (b) inhomogeneous soil with *m*=10 kPa/m. Left: *D/B*=1; right *D/B*=0·2. FS_V=2 and *h*=20 m.

NOTATION

A_{base} area of foundation base ($=B^2$)
B width of footing
c_a cohesion at soil–foundation interface ($=\alpha S_u$)
D embedment depth (=0, 0·2, 0·5, 1 m)
E Young's modulus
E_u undrained Young's modulus of soil ($=1800S_u$)
FS_V factor of safety against exceeding the purely vertical bearing capacity
f_S limiting shear resistance
h height of structural mass from foundation top (=10 m, 20 m)
K_H elastic horizontal stiffness of an embedded square-in-plan foundation
K_{HO} elastic horizontal stiffness of a surface square-in-plan foundation
K_R elastic rotational stiffness of an embedded square-in-plan foundation
K_{RO} elastic rotational stiffness of a surface square-in-plan foundation
M overturning moment
M_{max} maximum moment capacity of an embedded square-in-plan foundation
M_{ult} purely moment capacity
M_{uo} maximum moment capacity of a surface square-in-plan foundation
m mass of superstructure
m gradient of undrained shear strength with depth
N vertical force
N_u ultimate vertical load of embedded square-in-plan foundation
N_{ult} purely vertical capacity
N_{uo} ultimate vertical load of a surface square-in-plan foundation
Q horizontal force
Q_{max} maximum horizontal load of an embedded square-in-plan foundation
Q_{ult} purely horizontal capacity
Q_{uo} maximum horizontal load of a surface square-in-plan foundation
S_u undrained shear strength
S_{uo} undrained shear strength at the soil surface
u horizontal translation
W weight of superstructure
w vertical translation (settlement)
z depth from soil surface
α adhesion coefficient
γ specific unit weight of soil
δ sidewall displacement
θ rotation
λ gradient of shear modulus with depth
ν Poisson's ratio

REFERENCES

Abaqus (2013). Theory and analysis user's manual, version 6.8-3. Providence, RI, USA: Dassault Systèmes Simulia Corp.

Adamidis, O., Gazetas, G., Anastasopoulos, I. & Argyrou, C.(2014). Equivalent–linear stiffness and damping in rocking of circular and strip foundations. Bull. Earthquake Engng 12, No. 3, 1177–1200.

Allotey, N. & Naggar,M. H. E. (2003). Analytical moment–rotation curves for rigid foundations based on a Winkler Model. Soil Dyn. Earthquake Engng 23, No. 5, 367–381.

Anastasopoulos, I., Gazetas, G., Loli, M., Apostolou, M. & Gerolymos, N. (2010a). Soil failure can be used for seismic protection of structures. Bull. Earthquake Engng 8, No. 2, 309–325.

Anastasopoulos, I., Gelagoti, F., Kourkoulis, R. & Gazetas, G. (2011). Simplified constitutive model for simulation of cyclic response of shallow foundations: validation against laboratory tests. J. Geotech. Geoenviron. Engng, 137, No. 12, 1154–1168.

Apostolou, M., Gazetas, G. & Garini, E. (2007). Seismic response of slender rigid structures with foundation uplifting. Soil Dynam. Earthquake Engng 27, No. 7, 642–654.

Bransby, M. F. & Randolph, M. F. (1999). The effect of embedment depth on the undrained response of skirted foundations to combined loading. Soils Found. 39, No. 4, 19–33.

Brinch Hansen, J. (1970). A revised and extended formula for bearing capacity, Bulletin No. 28, pp 5–11. Copenhagen, Denmark: Danish Geotechnical Institute.

Butterfield, R. & Gottardi,G. (1994). A complete three-dimensional failure envelope for shallow footings on sand. Géotechnique 44, No. 1, 181–184.

Butterfield, R. & Ticoff, J. (1979). Design parameters for granular soils. Proceedings of the 7th European conference on soil mechanics and foundation engineering, Brighton, UK, vol. 4, pp. 259–261.

Chatzigogos, C. T., Pecker, A. & Salencon, J. (2009). Macroelement modelling of shallow foundations. Soil Dyn. Earthquake Engng 29, No. 5, 765–781.

Deng, L. &Kutter, B. L. (2012). Characterization of rocking shallow foundations using centrifuge model tests. Earthquake Engng Structl Dynam. 41, No. 5, 1043–1060.

Dobry, R. (2014). Simplified methods in soil dynamics. Soil Dyn. Earthquake Engng 61–62, 246–268. (Also found as: Nabor Carrillo Lecture, Sociedad Mexicana de Ingenieria Geotecnica, 2012.)

Dobry, R. & Gazetas, G. (1986). Dynamic response of arbitrarily shaped foundations. J. Geotech. Engng, 113, No. 2, 109–135.

Faccioli, E., Paolucci, R. & Vivero, G. (2001). Investigation of seismic soil–footing interaction by large scale cyclic tests and analytical models. Proceedings of the 4th International Conference on Recent Advances in Geotechnical Earthquake Engineering and Soil Dynamics, San Diego (ed. S. Prakash), paper no. SPL-5 (CD-ROM).

Gajan, S. & Kutter, B. L. (2008). Capacity, settlement, and energy dissipation of shallow footings subjected to rocking. J. Geotech. Geoenviron. Engng, ASCE 134, No. 8, 1129–1141.

Gazetas, G. (1983). Analysis of machine foundation vibrations: state of the art. Soil Dyn. Earthquake Engng 2, No. 1, 2–43.

Gazetas, G. (1991). Formulas and charts for impedances of surface and embedded foundations. J. Geotech. Engng, ASCE 117, No. 9, 1363–1381.

Gazetas, G. (2015). 4th Ishihara Lecture: Soil–foundation–structure systems beyond conventional seismic failure thresholds. Soil Dynam. Earthquake Engng 68, 23–39.

Georgiadis, M. & Butterfield, R. (1988). Displacements of footing on sands under eccentric and inclined loading. Can. Geotech. J. 25, No. 2, 199–212.

Gerolymos, N. & Gazetas, G. (2006a). Winkler model for lateral response of rigid caisson foundations in linear soil. Soil Dyn. Earthquake Engng 26, No. 5, 347–361.

Gerolymos, N. & Gazetas, G. (2006b). Development of Winkler model for static and dynamic response of caisson foundations with soil and interface nonlinearities. Soil Dyn. Earthquake Engng 26, No. 5, 363–376.

Gerolymos, N. & Gazetas, G. (2006c). Static and dynamic response of massive caisson foundations with soil and interface nonlinearities – validation and results. Soil Dyn. Earthquake Engng, 26, No. 5, 377–394.
Gottardi, G., Houlsby, G. T. & Butterfield, R. (1999). The plastic response of circular footings under general planar loading. Géotechnique 49, No. 4, 453–470.
Gourvenec, S. (2007). Shape effects on the capacity of rectangular footings under general loading. Géotechnique 57, No. 8, 637–646.
Gourvenec, S. (2008). Effect of embedment on the undrained capacity of shallow foundations under general loading. Géotechnique, 58, No. 3, 177–185.
Houlsby, G. T. (2003). Modelling of shallow foundations for offshore structures. In BGA international conference on foundations – innovations, observations, design and practice (ed. T. A. Newson), pp 11–26. London, UK: Thomas Telford.
Houlsby, G. T. & Puzrin, A. M. (1999). The bearing capacity of strip footings on clay under combined loading. Proc. R. Soc. A: Math. Phys. Enging Sci. 455, No. 1983, 893–916.
Kausel, E. (2010). Early history of soil–structure interaction. Soil Dyn. Earthquake Engng 30, No. 9, 822–832.
Kausel, E. & Roesset, J. M. (1975). Dynamic stiffness of circular foundations. J. Engng Mech. Div., ASCE 101, No. 6, 771–785.
Karapiperis, K. & Gerolymos, N. (2014). Combined loading of caisson foundation in cohesive soil: finite element versus Winkler modeling. Comput. Geotech. 56, 100–120.
Lekkakis, P. (2012). Analysis of skirted foundations for offshore wind turbines. Diploma thesis, Laboratory of Soil Mechanics, National Technical University of Athens, Athens, Greece.
Makris, N. & Roussos, Y. (2000). Rocking response of rigid blocks under near source ground motions. Géotechnique 50, No. 3, 243–262.
Martin, C. M. (1994). Physical and numerical modelling of offshore foundations under combined loads. DPhil thesis, University of Oxford, Oxford, UK.
Martin, G. R. & Lam, P. (2000). Earthquake resistant design of foundations: retrofit of existing foundations. Proceedings Geo-Engineering 2000 Conference, Melbourne, Australia.
Meyerhof, G. G. (1953). The bearing capacity of foundations under eccentric and inclined loads. Proceedings of the 3rd International Conference on Soil Mechanics Foundation Engineering, Zurich, Switzerland, vol. 1, pp. 440–445.
Nova, R. & Montrassio, L. (1991). Settlements of shallow foundations on sand. Géotechnique 41, No. 2, 243–256.
Ntritsos, N., Anastasopoulos, I. & Gazetas, G. (2015). Static and cyclic response of square embedded foundations. Géotechnique 65, No. 10, 805–823.
Pais, A. & Kausel, E. (1988). Approximate formulas for dynamic stiffnesses of rigid foundations. Soil Dyn. Earthquake Engng7, No. 4, 213–227.
Panagiotidou, A. I., Gazetas, G. & Gerolymos, N. (2012). Pushover and seismic response of foundations on stiff clay: analysis with P–Δ effects. Earthquake Spectra 28, No. 4,1589–1618.
Paolucci, R., Shirato, M. & Yilmaz, M. T. (2008). Seismic behavior of shallow foundations: Shaking table experiments vs numerical modeling. Earthquake Engng Structl Dyn. 37, No. 4, 577–595.
Pecker, A. (1998). Capacity design principles for shallow foundations in seismic areas. Proceedings of the 11th European conference on earthquake engineering, Paris, France, Invited Lectures volume, pp. 303–316.
Poulos, H. G. & Davis, E. H. (1974). Elastic solutions for soil and rock mechanics. New York, NY, USA: John Wiley & Sons.
Poulos, H. G., Carter, J. P. & Small, J. C. (2001). Foundations and retaining structures – research and practice. Proceedings of the 15th international conference on soil mechanics and geotechnical engineering, Istanbul, Turkey, vol. 4, pp. 2527–2607.
Randolph, M. & Gourvenec, S. (2011). Offshore geotechnical engineering. Abingdon, Oxford, UK: Spon Press.

Randolph, M. & Puzrin, A. M. (2003). Upper bound limit analysis of circular foundations on clay under general loading. Géotechnique 53, No. 9, 785–796.
Roesset, J. M. (1980). Stiffness and damping coefficients of foundations. Dynamic response of foundations: analytical aspects (eds M.W. O'Neil and R. Dobry), pp. 1–30, American Society of Civil Engineers.
Salencon, J. & Pecker, A. (1995). Ultimate bearing capacity of shallow foundations under inclined and eccentric loads. Part II: Purely cohesive soil without tensile strength. Eur. J. Mech. A – Solids 14, No. 3, 377–96.
Tassoulas, J. L. & Kausel, E. (1983). On the effect of the rigid sidewall on the dynamic stiffness of embedded circular footings. Earthquake Engng Structl Dyn. 11, No. 3, 403–14.
Taiebat, H. A. & Carter, J. P. (2000). Numerical studies of the bearing capacity of shallow foundations on cohesive soil subjected to combined loading. Géotechnique 50, No. 4, 409–418.
Terzaghi, K. (1943). Theoretical soil mechanics. New York, NY, USA: John Wiley.
Vucetic, M. & Dobry, R. (1991). Effect of soil plasticity on cyclic response. J. Geotech. Engng, 117, No. 1, 89–107.
Vulpe, C., Gourvenec, S. & Power, M. (2014). A generalized failure envelope for undrained capacity of circular shallow foundations under general loading. Géotechnique Lett. 4, No. 3, 187–196.
Wolf, J. P. (1985). Dynamic soil–structure interaction. Englewood Cliffs, NJ, USA: Prentice-Hall.
Wolf, J. P. (1988). Soil–structure interaction analysis in time-domain. Englewood Cliffs, NJ, USA: Prentice-Hall.
Yun, G. & Bransby, M. F. (2007). The horizontal-moment capacity of embedded foundations in undrained soil. Can. Geotech. J. 44, No. 4, 409–424.